Philipp Dechent

Simulation and Real-Life assessment of cell-to-cell variation of ageing lithium-ion batteries

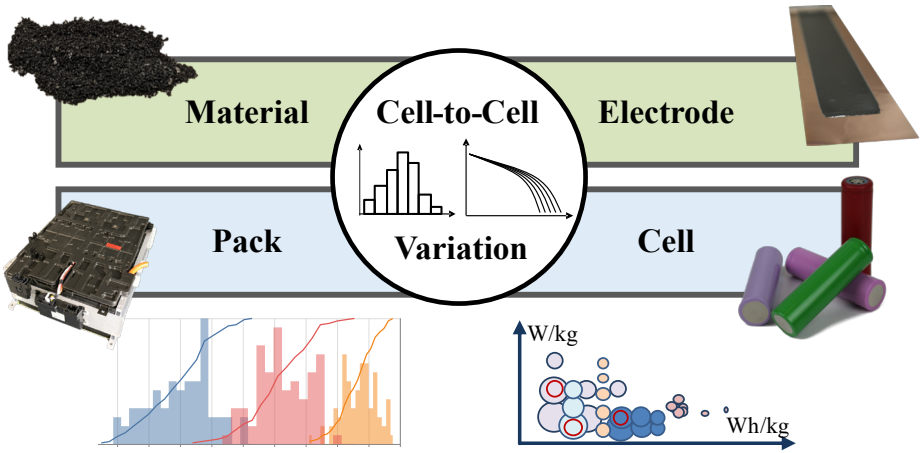

Aachener Beiträge des ISEA Band 163

Simulation and Real-Life Assessment of Cell-to-Cell Variation of Ageing Lithium-Ion Batteries

Von der Fakultät für Elektrotechnik und Informationstechnik
der Rheinisch-Westfälischen Technischen Hochschule Aachen
zur Erlangung des akademischen Grades eines Doktors der
Ingenieurwissenschaften genehmigte Dissertation

vorgelegt von

Philipp Dechent, M. Sc.
aus Wiesbaden

Berichter:
Universitätsprofessor Dr. rer. nat. Dirk Uwe Sauer
Professor David Howey, University of Oxford, UK

Tag der mündlichen Prüfung: 19 November 2021

AACHENER BEITRÄGE DES ISEA
Vol. 163

Editor:
Univ.-Prof. Dr. ir. Dr. h. c. Rik W. De Doncker
Director of the Institute for Power Electronics and Electrical Drives (ISEA)
RWTH Aachen University

ISSN 1437-675X

Institute for Power Electronics and Electrical Drives (ISEA), RWTH Aachen University
Jaegerstr. 17/19 • 52066 Aachen • Germany
Tel: +49 (0)241 80-96920
Fax: +49 (0)241 80-92203
post@isea.rwth-aachen.de

Vorwort

Die vorliegende Dissertation entstand im Rahmen meiner Tätigkeit als wissenschaftlicher Mitarbeiter am Institut für Stromrichtertechnik und Elektrische Antriebe (ISEA) der RWTH Aachen University. Hierfür möchte ich Prof. Dirk Uwe Sauer für die Möglichkeit der Promotion, Betreuung und sein mir entgegengebrachtes Vertrauen danken. Prof. David Howey danke ich für die Zusammenarbeit und die Übernahme des Koreferats.

Früh im Studium wurde ich durch Madeleine Ecker ans Institut geholt und habe dort als Hiwi & Bachelorarbeit in der Abteilung MAL zusammen mit Alexander Warnecke und Friedrich Hust gearbeitet. Dabei habe ich auch Stefan Käbitz, Johannes Schmalstieg und Heiko Witzenhausen kennen und schätzen gelernt.

Mit einem Abteilungswechsel habe ich dann meine Masterarbeit bei Susanne Lehner geschrieben, mit Unterstützung durch Thorsten Baumhöfer, Jan Becker und Florian Ringbeck, um dann als auch die Promotion bei BST zu beginnen.

Vielen Dank auch an die weiteren Kollegen und insbesondere für die Zusammenarbeit mit Dominik Jöst, Stephan Bihn, und Lisa Willenberg. Auch möchte ich Katharina Quade und Alexander Blömeke für ihre Korrekturen meiner Schriftfassung danken.

Zudem möchte ich allen Studenten danken, die mit mir zusammengearbeitet haben, insbesondere Marcel Eckert, Julian Tenhagen, Alexander Epp und Elias Barbers, die mich über längere Zeit durch Abschlussarbeiten und Hiwi-Tätigkeiten begleitet haben. Genauso gilt mein Dank auch Sarah Leibeling und Miriam Wittbusch, die mich bei den Arbeiten an CARL unterstützt haben.

Zuletzt möchte ich Sabine und meiner Familie für den starken Rückhalt und Hilfe aller Art danken.

Aachen, August 2022
Philipp Dechent

Kurzfassung

Eine der wichtigsten Komponenten eines Elektrofahrzeugs ist sein Energiespeicher. Leider hat es sich auch als die teuerste Komponente erwiesen, die die Leistung des Fahrzeugs, z. B. die Reichweite oder die Leistungsfähigkeit, bei einem bestimmten Kostenziel einschränkt. Eine Verbesserung der Zellqualität und einer Reduktion der Streuung der Zellparameter innerhalb des Systems führen zu einer Kostensenkung, indem die Anzahl der in der Produktion aussortierten Zellen verringert wird. Darüber hinaus ist es insbesondere bei großen Speichersystemen, wie z. B. in Elektrofahrzeugen oder bei stationären Speicheranwendungen, wichtig, eine lange Nutzbarkeit der Systeme zu gewährleisten. Insbesondere bei stationären Anwendungen muss die Lebensdauer im Bereich von 10 bis 15 Jahren liegen. Daher müssen die Hersteller für langlebige Batteriemodule als kleinste austauschbare Einheiten sorgen. Bisherige Analysen zu den Auswirkungen von Variationen in kommerziellen Lithium-Ionen-Batteriesystemen auf die Alterung haben gezeigt, dass die Streuung der Zellparameter der Batterien eine entscheidende Rolle für die Langlebigkeit spielt. Diese Arbeit zielt darauf ab, Systemtopologien für individuelle Anwendungen zu optimieren, eine Überdimensionierung von Batteriesystemen zu vermeiden und Vorhersagen über die Lebensdauer und quantifizierbare Ausfallraten von Batterien bei gleichzeitiger Kostenreduzierung zu geben. Es wurde eine Simulations-Toolchain entwickelt, um Variabilitäts- und Alterungsraten-Streuungen in den Systementwurfsprozess einzubeziehen. Im Rahmen des Simulationswerkzeugs können Batterietopologien mit unterschiedlichen Nutzungsprofilen, Zellparameterspreizungen und verschiedenen Alterungsraten simuliert werden.

Insgesamt vertieft die vorliegende Arbeit das Verständnis und die Quantifizierung von Zell-zu-Zell-Variationen und erzielt so Fortschritte in mehreren Aspekten. Entscheidend ist das zielgerichtete Testen von Batterien unter Einbeziehung von Variationen, um die statistische Sicherheit zu erhöhen, was zu einer Verringerung der Kosten und des Aufwands für das Testen durch eine vorgegebene Stichprobengröße führt. Darüber hinaus ermöglichen Prognosemodelle mit zusätzlichem Konfidenzintervall repräsentative Vorhersagen von Lebensdauer und Ausfallszenarien in der Anwendung.

Abstract

One of the essential components of an electric vehicle is its energy storage system. Unfortunately, it has also proven to be the most expensive component, limiting the vehicle's performance, for example, range or power, for a given cost target. If higher spreads and more inferior cell quality can be coped within the system, costs can be lowered by decreasing the number of cells rejected in production. In addition, it is essential, particularly for large storage systems such as automotive or stationary storage applications, to ensure the extended usability of the systems. Especially in stationary applications, design lifetimes have to be in the range of 10 to 15 years. Therefore, the manufacturers need to ensure long-lasting battery modules as the smallest exchangeable units. Previous analysis on the impact of variations in commercial lithium-ion battery systems on ageing showed the vital role of spreads in cell parameters of the batteries.

The research in this thesis aims to optimise system topologies for individual applications to find suitable cells, avoid oversizing battery systems and give forecasts of a lifetime and quantifiably failure rates for battery packs while decreasing cost. A simulation toolchain was developed to incorporate variability and spread of ageing rates in the system design process. In the scope of the simulation tool, battery topologies can be simulated with varying usage profiles, cell parameter spreads and varying ageing rates.

Overall, with the deeper understanding and quantification of cell-to-cell variation that has been developed within this work, advances in several aspects have been achieved. Most relevant is target-oriented testing of batteries incorporating variation for enhanced statistical certainty, resulting in decreased cost and testing efforts through a predetermined sample size. In addition, lifetime prognosis models with additional confidence intervals allow representative predictions of lifetime and failure scenarios in the application.

Contents

1 Introduction

1.1 Motivation

Lithium-ion batteries have become ubiquitous in many portable applications ranging from wearables and medical devices to e-bikes, electric vehicles, grid storage, trains, and ships. First commercialised by Sony in 1991, lithium-ion batteries were developed starting in the late 1970s [1] by several teams with exceptional contributors Goodenough, Whittingham and Yoshino receiving the Nobel Prize in 2019.

To further increase market penetration, prices need to remain falling. This enables new applications, previously non-economical, especially for high power and energy demands, as well as frequent charge and discharge cycles [2]. Figure 1.1 depicts the development of the whole range of lithium-ion batteries, not only for automotive applications, over the last 25 years, with an increase in energy density of 3 % per year, from 90 Wh/kg to 300 Wh/kg for C-rates up to 3C [3]. At the same time, prices decreased by a factor of 80 [4].

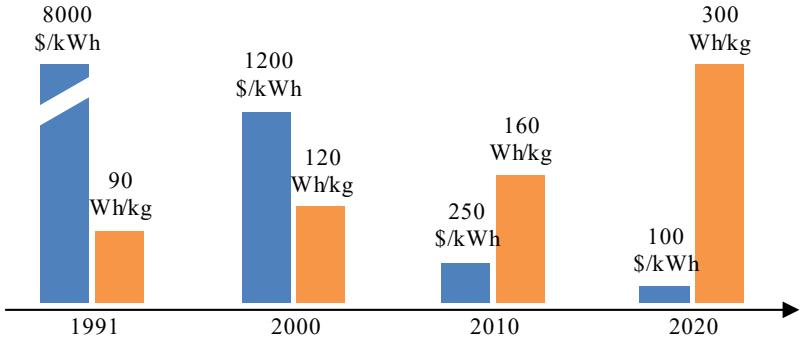

Figure 1.1: Development of price and energy density over time.

By replacing expensive components or cutting down their share in the product, or increasing the production volume cells become cheaper. For example, the electrolyte was reduced to a level where new cells appear dry when opened, compared to several millilitres of excess electrolyte a few years ago [5].

To get a perspective on the decline in prices, an analogy to the photovoltaic market is helpful. Figure 1.2 shows the contribution of cost reduction broken down into categories by Kavlak et al. [6]. The differences between 1980-2001, 2001-2012 and overall are shown. Overall, all categories, except other costs, led to a decrease in price, but different factors had the leading role in cost decrease over time. In the first phase of cost reduction from 1980-2001, efficiency, non-Si material cost, silicon price, usage, and wafer size were the most significant contributions.

A key difference in this example is the inherent limit of lithium-ion batteries based on the weight of a cell since every charge carrier needs to be a lithium-ion. Nevertheless, especially the second part of cost reduction from 2001-2012 was heavily driven by plant size and therefore economies of scale. A significant part of the economies of scale is also the reducing oversizing of parts and components without loss of function.

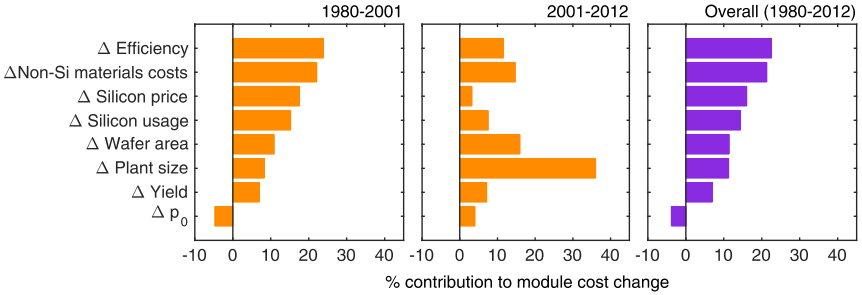

Figure 1.2: Contributions to cost reduction from Kavlak broke down into categories [6]. p_0 includes all other costs (electricity, labour, etc.).

Overall lithium-ion batteries offer the highest potential for large-scale use of energy storage devices but cannot be considered the holy grail since they are still too expensive for some applications, especially long-term storage [7]. In addition, there are special applications that cannot compromise safety. In those cases, other technologies are necessary [8], and they usually have a price. In most cases, however, the costs are the decisive criterion. On the other hand, there are applications, for example, electric city scooters, where the product is regularly collected anyway, and their replacement is straightforward. Therefore, it can be cost-effective to allow an increase in variability of the ageing rate to decrease manufacturing discards through easy replacement.

A significant factor in cost reduction is high volume in scalable, automated production. Of course, this only applies if hardly any waste is produced, which is a challenge, especially in battery production. Certain variations in product properties cannot be avoided, but they affect battery performance and ageing [9]. Rigorous process monitoring and rigid quality control reduce fluctuations, but they are expensive and increase the scrap rate. An alternative is to allow differences in the cell properties and managing them in the application. This requires handling the statistical spread of cell-to-cell variation in the initial state after production. An even greater challenge is quantifying degradation, which also differs strongly. A reliable prediction is difficult even with a large amount of data as numerous stress factors have to be considered.

Therefore, quantifiable degradation models, including variations within cells, are necessary, as well as an in-depth understanding of cell-to-cell variation.

1.2 Structure

As shown in Figure 1.3, following the fundamentals of batteries and battery-related statistics in Chapter 2, in Chapter 3.1-3.4, a literature review is presented covering the origins of cell-to-cell variations and inhomogeneities on a multiscale level, their impact on electrochemical performance, and their characterisation and tracking methods, ranging from the use of large-scale equipment to in operando studies. Finally, the review summarises the state-of-the-art understanding and characterisation of cell-to-cell variations and inhomogeneities observed upon ageing. They were tackled with a bottom-up approach from materials to battery packs and ending on the proposed characterisations.
Chapter 3.5 establishes the minimum number of cells, which should be tested to accurately represent population variability since testing many cells is expensive. Derived from various degradation datasets, including new measurements performed as part of this work, empirical capacity-versus-time ageing models were fitted. While assuming that the model parameters could be drawn from a distribution describing a larger population, then, using a hierarchical Bayesian approach, the number of cells required to be tested was estimated.
In Chapter 4.1, battery ageing data from in-house measurements and published data were combined into a uniform database; the total dataset size exceeds

1000 GB. This is the largest dataset described in the literature and is based on developing an evaluation toolchain and automatic data assessment.
In Chapter 4.2-4.4, lithium-Ion battery lifetimes from cyclic and calendar ageing tests of more than 1000 cells were compared employing novel plots termed ENPOLITE (energy-power-lifetime-temperature). At a glance, ENPOLITE plots inform about the nominal capacity, cell format, cell chemistry, average ageing test duration, measurement temperature, specific power employed for testing, energy density, and the achieved lifetime for every cell. In addition, a battery lifetime coefficient was derived, allowing the comparison of lithium-ion batteries with different weights or volumes, capacities, and cell chemistries. The combination of multiple parameters in ENPOLITE facilitated a thorough comparison of various battery degradation. In addition to the cell-specific parameters during cycling, the specific stored energy and the storage temperature were depicted in a calendar ENPOLITE plot.
Based on the evaluated datasets in Chapter 5, different health indicators are compared, and the correlation analysed. The measurement difficulty varies between health indicators: Some can be extracted from a current pulse or charge, whereas others need a well-defined and controlled setting to be recorded.
Therefore, understanding the correlation of health parameters can lead to a greater focus on easy to record parameters to better track ageing trends when high-resolution data is not available. Health indicators taken into account are, among others, impedance measurements of different pulse lengths, capacity values at different discharge procedures, check-ups, weight and initial voltage. The work is based on five different ageing sets covering variations in cell chemistry (NMC, LFP, NCA), cell type (round, prismatic), as well as size and designated application (consumer, automotive).
Based on an impedance-based cell model, in Chapter 6, a modelling framework was developed to simulate batteries' electrical and thermal behaviour as well as their ageing behaviour in different configurations. With load profiles, usage patterns and lifetime requirements, batteries can be simulated multiple times as part of a Monte-Carlo simulation with cell properties derived from the ageing rate distributions and initial spread distributions.
The work concludes in Chapter 7 with a summary and outlook.

Chapter 1: Introduction

Chapter 2: Fundamentals

Chapter 3: Inhomogeneities and lithium-ion batteries

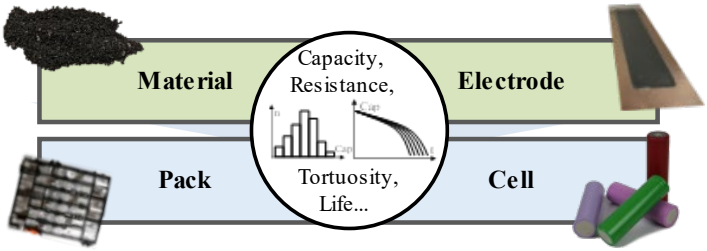

Chapter 4: Evaluation of ageing tests

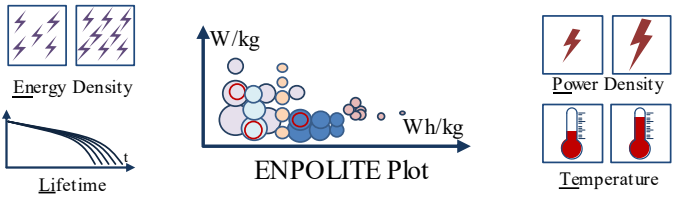

Chapter 5: Correlation of health indicators

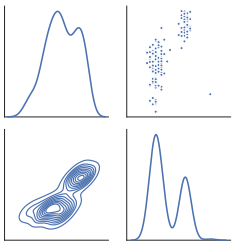

Chapter 6: Stochastic battery ageing model

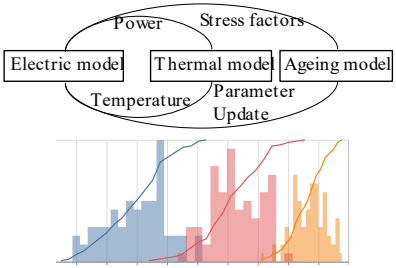

Chapter 7: Summary and Outlook

Figure 1.3: Structure of this work.

2 Lithium-Ion Batteries

In this chapter, the fundamentals of lithium-ion batteries and trends to higher energy densities are discussed.

2.1 Fundamentals of lithium-ion batteries

A lithium-ion battery consists of two electrodes in the purest form, a separator electrically insulating the two electrodes and an electrolyte for ion transport between the electrodes. Due to the low electric conductivity of most electrodes, metallic current collectors are coated with the electrode material. The positive electrode (PE) is named as the cathode and the negative (NE) as the anode for both the charge and the discharge stage per definition. During charging, lithium-ions are transported from the cathode to the anode. The process of intercalation of lithium-ions is called lithiation. During discharge, the process is reversed, and the anode is delithiated while the cathode is lithiated.

There is a multitude of material combinations considered lithium-ion batteries. Possible anode electrodes consist of intercalation, alloying, or conversion materials [10], while cathodes consist of conversion, oxide, or polyanionic materials [11]. Similarly, cathode materials are primarily based on either different variants of nickel-manganese-cobalt oxide (NMC), nickel-manganese-aluminium oxide (NCA) or lithium-iron-phosphate (LFP) [1], [11], [12]. For simplification, the combination of NMC vs Graphite is considered henceforth, including the extreme of only lithium manganese oxide NMC010 and lithium cobalt oxide NMC001.

Today, anodes are dominated by graphite and graphite-based materials with a few high power applications based on lithium-titanate [1], [10], [12]. Graphite and other carbon blacks consist of layers of graphene [13]. During charging, lithium-ions flow to the graphite anode and intercalate or migrate within the graphene layers. The anode particles are not loaded uniformly but within stages where only every other layer is loaded. In Figure 2.2, the distinct stages are shown in the schematic with an increasing state of charge or load level from stage III to stage I. Those stages also corresponded to specific voltages vs lithium [13], [14]. The stages also show distinctive visible colours. Therefore, the discharge and charge curve analysis can give information about the stages of the graphite.

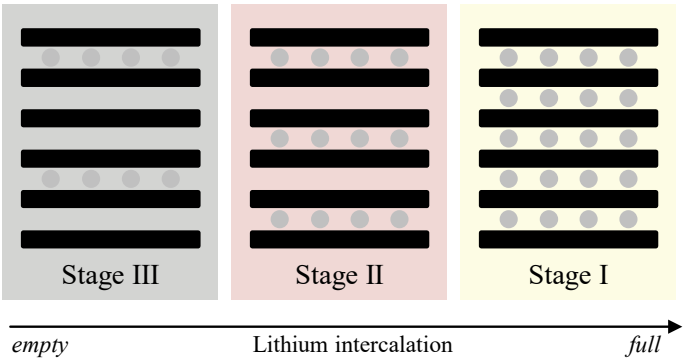

Figure 2.1: Stage wise intercalation of lithium-ions in graphite.

2.2 Increasing energy density

As discussed in Chapter 1.1, the improvement in energy density is one of the main drivers for cost reduction. Also, new applications become feasible with higher energy densities. To increase the energy density, either the number of exchangeable ions within the same volume or mass needs to increase, or the nominal voltage per charge transfer must rise. With the volumetric capacity, Ah/l and the nominal voltage V_{nom} the volumetric energy density, Wh/l, can be calculated. Many improvements within the battery are indirect. For example, the reduction of the separator, current collector and anode makes up more space for bigger cathodes that host the cyclable lithium-ions. Consequently, the goal is to reduce oversizing and enable the same energy stored with less material and volume.

Since energy density became a key performance indicator for research roadmaps and funding, calculations are often nudged in a favourable direction. Values can be inflated either by reporting capacities at shallow currents, oversized lithium inventory in half-cells, neglecting essential additives or excessive amounts of electrolyte. In full cells with realistic usage profiles, the reported energy then cannot be achieved [3]. In addition, the reference volume or mass can be chosen in favour of a high reported energy density. Compared to the lithiated state, electrodes are lighter without the lithium present or also less voluminous. Considering the extreme case of an anode-free cell, where lithium is directly deposited on the copper foil [15], the delithiated state's gravimetric and

volumetric energy density is theoretically infinitely high since there is no host material and lithium is directly plated on the copper current collector.

2.2.1 Decreasing the anode & pre-lithiation

The most common anode material, graphite, exhibits a gravimetric capacity of 370 $mAhg^{-1}$ which is comparatively low but partly compensated by the favourably low lithiation and delithiation potential of 0.1 vs Li/Li^+ [10]. Another significant advantage is the small volume change under 10 % [16]. This makes graphite extremely stable and cells with a coulombic efficiency of over 99.995 % and over 5000 full charge and discharge cycles possible [17].

An anode material currently introduced in commercial cells is silicon [18]. Silicon exhibits a volume increase of over 300 % during lithiation. Blend materials and nano-sized silicon particles are used to mitigate this effect [19], [20]. Nano-sized silicon has a high surface area, increasing the number and intensity of side reactions and SEI formation rate [21]. But the high surface area to volume ratio reduces the effects of the high volume change. Blend materials of silicon and graphite also observe more minor volume changes and do not offer pure silicon anodes' total theoretical energy density.

While the anode is larger in electrode area dimensions to prevent lithium-plating in the boundary areas, the cathode has a higher capacity [22]. On the one hand, the typical cathode materials get unstable when delithiated too much [11]. On the other hand, some of the cathode's lithium is consumed within the first cycles. Within a full cell, all active lithium is provided by the cathode material. The cell is assembled in the discharged state with the anode fully delithiated. The SEI is formed within the first cycles, consuming some of the active lithium provided by the coulombic oversized cathode.

In a typical lithium-ion battery, lithium is introduced to the cell through the cathode. Pre-lithiation is a technique used to increase the amount of lithium ions within the cell via the anode. During formation, some lithium is consumed by side reactions and the Solid-Electrolyte-Interface (SEI), decreasing lithium inventory. When some lithium is intercalated into the anode material before assembly, the total amount of lithium within the cell increased [23]. After the first few cycles of initially consuming free lithium-ions, the lithium inventory is equal to the maximum lithium usable by anode and cathode.

2.3 Mathematical description of battery failure

Understanding battery ageing analogies to other forms of ageing are helpful. Humans also age, lose their function and eventually pass away. On a population level, some people die at a very young age, while others show longevity.
To understand the nature of statistical data, the analogy of a human population survival curve for England and Wales shown in Figure 2.2 is helpful. The maximum age human beings can reach increased a few years but did not change significantly from 1851 to 2011. However, infant mortality has decreased extremely over these years, so that the profile of the curves and, in particular, the average age reached has undergone a massive change. This comparison shows that neither the maximum nor the average lifetime alone is meaningful - neither for humans nor for batteries.

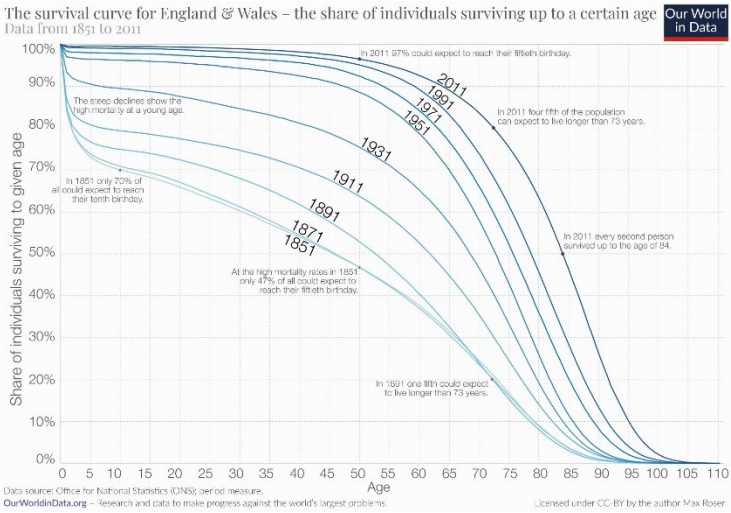

Figure 2.2: Population survival curves in England and Wales. M. Roser CC-By [24].

This analogy can be taken even further when team sports or battery modules and packs are considered. Especially in competitive sports, high requirements are demanded of the athletes. Once they drop below a threshold, they cannot fulfil the requirement anymore, so they cannot participate in the sporting event. For example, if one rower from the rowing eight gets tired and does not perform, the

other team members have to compensate, but since they are already on the highest demand the whole team fails with the decrease in total performance. This also applies to batteries that are connected in series or parallel. Thus, the worst cell is critical for performance. A gradual loss of a capability can define this kind of failure without total loss of all functions. In lithium-ion systems designed with a priority on energy, this is often 70 % or 80 % of the initial capacity, directly corresponding to range or runtime, and called the end-of-life criterion. For systems with priority on power, a 200 % resistance increase is used as the end-of-life criterion, corresponding to a reduction in power of 50 %.

On the other hand, a spontaneous total loss can occur when all function is lost at once, for example, a short-circuit in a lithium-ion battery. This behaviour is considered random since no prediction of a specific spontaneous total loss can be made. A total loss failure probability can change over time and is often described as a bathtub curve, with early faults, a plateau with low failure probability, and a rising probability when the effects of fatigue are dominant. An example of this working or not-working behaviour can be valid for current collector busbars. The function of conducting current can be fulfilled up to the moment of failure of a weld seam. Even if fatigue might be visible within the seam before, the current demand can still be fulfilled.

If multiple systems are considered, failure time data can be evaluated. Figure 2.3 a) shows the discrete depiction of failure events over time in blue and the cumulated-failure rate as the fraction of systems failed in orange. In this example, with four specimens, four individual failures occur, increasing the cumulated failure rate with each event.

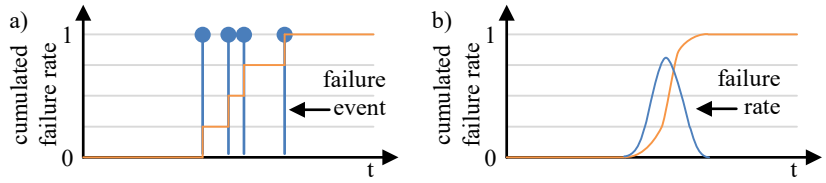

Figure 2.3: a) discrete cumulated failure rate with four failure events. b) continuous cumulated failure rate with a failure rate as a function of time.

For continuous data, Figure 2.3 b) shows the failure rate or probability density function (PDF) in blue and cumulated-failure-rate or cumulative distribution function (CDF), the integral of the failurefunction, in orange. Both functions

(PDF and CDF) fully specify the distribution and are different representations [25].Within a pure series connection, the failure or hitting the end-of-life criterion of a single cell renders the battery failed or at the end-of-life criterion as well. Comparably, a single cell within a parallel connection can be below the failure threshold but be supported by the rest of the parallel connection, so the parallel connection can still fulfil the desired demand. Looking at an example of a large fleet of electric vehicles with a battery system each, a failure rate can be fitted to the distribution of failure events.

2.3.1 Interference model

To better visualise failure occurrence over time, the interference model can be used [26]. Figure 2.4 a) shows a plot with an arbitrary capability unit on the x-axis, which can be replaced by, e.g., range or maximal power. The y-axis shows the frequency of samples, and the demand is shown in green, while the capability is shown in blue. Each plot depicts a range of samples at one moment in time. In Figure 2.4 b), the same interference plot is shown at a later moment. The demand is unchanged, but due to ageing, the capability of the samples decreased. Therefore, some of the demands cannot be fulfilled by all samples and failures (in orange) occur.

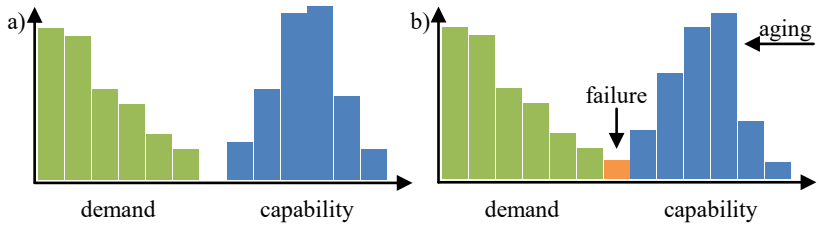

Figure 2.4: Interference model for failures, in green the demand probability and blue the capability probability is shown a) All demands can be fulfilled by the capabilities b) Some demands cannot be met, and failures occur.

Figure 2.5 a) shows the example of a total loss of function of a sample, where none of the demands can be fulfilled by some of the cells. Referring to an example of ranges within an electric vehicle fleet, the failure in Figure 2.4 b) shows an electric vehicle, which cannot make all trips and Figure 2.5 a) shows an electric vehicle without any functionality left. Figure 2.5 b) shows a progressed moment

in time, where ageing made all subsets unable to meet all demands. Within the electric vehicle fleet example and the capability range, no electric vehicle has enough range to fulfil all demanded trips.

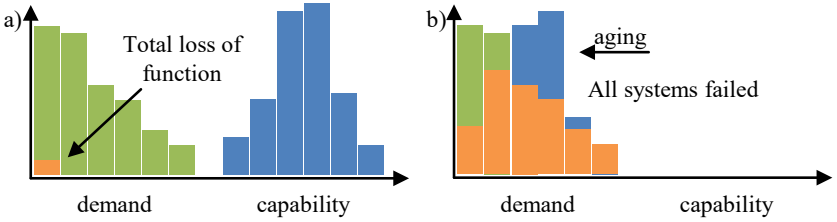

Figure 2.5: Interference model for different failure types. a) loss of all function, capability for a small subset, b) loss of all function and partial loss function on all samples.

Compared to Figure 2.4 a), Figure 2.6 a) depicts a higher demand while capability remains constant, leading to failures due to excessive stress. This could be an electric vehicle fleet with different routes and range demands, which cannot all be met. In b) the same demand can be fulfilled with the same average capability but less variability. A set with lower variability possesses less underperforming cells.

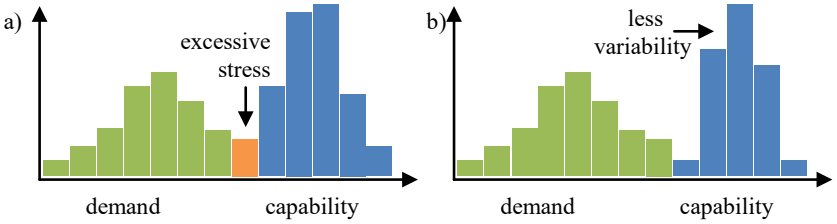

Figure 2.6: Interference model with varying demand leading to a) excessive stress and b) fulfilment of demand due to less capability variability.

3 Inhomogeneities and lithium-ion batteries

In this chapter, inhomogeneities and cell-to-cell variation in lithium-ion batteries are discussed. First, results from the literature are presented, how inhomogeneities can be monitored and measured, followed by the root causes. Parts of 3.1-3.3 are published in a review article [27] with an equal contribution by the author and David Beck. Chapter 3.5 is an extract from [28] with an equal contribution by the author and Samuel Greenbank. Here the majority of the data acquisition and preparation was performed by the author and the Bayesian approach by Samuel Greenbank.

Inhomogeneities are a significant concern for the reliability and safety of modern batteries. While significant effort must be deployed in the production process to eliminate them and with tools to identify expected variation already before assembling them to battery packs, developing advanced tracking methods to anticipate and quantify their impact is crucial. Many ways to track inhomogeneities can be found in the literature with different measuring principles and varying complexity.

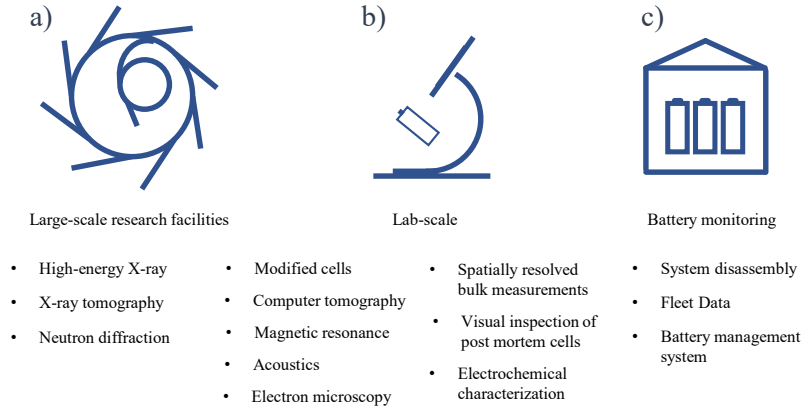

Figure 3.1: Different scales and complexity for ctcV and inhomogeneities measurements.

They differ in length scale from sub-particle to pack-to-pack variance tracking, in time scales from milliseconds to years and in the complexity of the measurement instruments from particle accelerators down to using the onboard battery

management system (BMS).In this chapter, a comprehensive set of analytical methods for evaluating inhomogeneities and cell-to-cell variation (ctcV) is presented. These methods are grouped by measurement complexity into research facility scale, laboratory scale and field-scale methods, as depicted in Figure 3.1.

3.1 Field/usage data

Data on ageing are clustered into two groups field data and laboratory data. The latter is performed by testing facilities and is often an accelerated lifetime test to predict lifetime performance for a new cell or performance. On the other hand, field data can be recorded by the manufacturer or by self-report by users.
But real-life field data has disadvantages compared to laboratory data since it relies on the State-of-Health-estimator implemented on the BMS to compress the data needed to store and transmitted. An additional impairment of self-reported data is the user group consisting of primarily electric car enthusiasts and not a representative sample. Assumably, they will care more for their car and follow the manufactures recommendations, and for example, they do less fast charging and avoid unnecessary high SoCs than worst-case users.

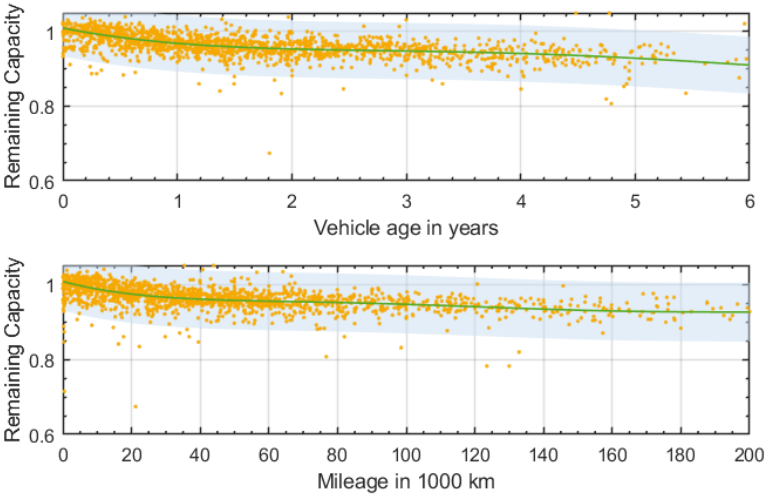

Figure 3.2: Maximal Range Survey from Tesla Motors Club with reported remaining capacity over milage and years [29]. Each orange dot is one entrance, and vehicles have multiple entries within their life. The trendline is shown in green, and the 95 % confidence interval is in light blue.

To the author's knowledge, there is no publicly available dataset from manufacturers, and evaluations are rarely shown and sparsely [30]. The following consumer reports of the state of battery systems, especially for electric vehicles, are shown [139–141].

In the *Maximal Range Survey* [29] performed by the Tesla Motors Club in the Netherlands, participants record several parameters about their private EV, including depicted range, mileage and vehicle age. In Figure 3.2, the capacity degradation is shown for up to six years and >200.000 km with some individual vehicles included at multiple times. A general degradation trend and longevity of the battery packs can be seen, but effects from stress as the temperature profile of an individual pack are not included. Since consumer reports are voluntary, typically, the participants are well informed and highly interested. This bias towards well caring consumers may only reflect a sub-portion of users with less variability. Another major drawback of consumer reports is the type of data collected.

Typically, either the State-of-Health value estimated by the BMS depicted on the driver's screen or the range after a full charge is recorded manually along with the mileage. In addition, as explained in Figure 3.3, the user typically can only see the net capacity and, therefore, only see degradation in the driver's display when the reserve is already degraded.

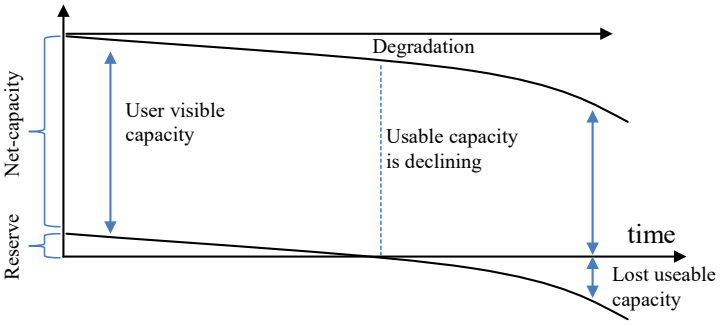

Figure 3.3: User-visible capacity from a battery management system, the reserve is not shown to the user, but the State-of-Health remains 100 % even though degradation already happened.

Range estimators as a measurement for capacity also include the driver's energy efficiency level. Comparing multiple cars reflects not only the different degradation levels but also driver-to-driver variability. The depicted range for an energy-intensive driver at the fully charged state at the same degradation level is lower compared to an energy-efficient driver. Another variability unaffected by the battery is the energy needed for cooling in a hot climate included in the energy consumption. This granular data, if collected, is not available through consumer reports.

For reducing the amount of data down-sampling, lowering the time resolution, and clustering, and lowering the spatial resolution is necessary. The BMS of the battery system monitors all cells and temperatures but only reports the critical values, as under or overvoltage and higher-order signals like the state-of-charge of the entire system. The State-of-Health (SOH) and State-of-Power (SOP) are also determined and sent to other vehicle control units or logging stations. For fleet data, only a few SOH values per vehicle are reported, and the usage for the cars varies.

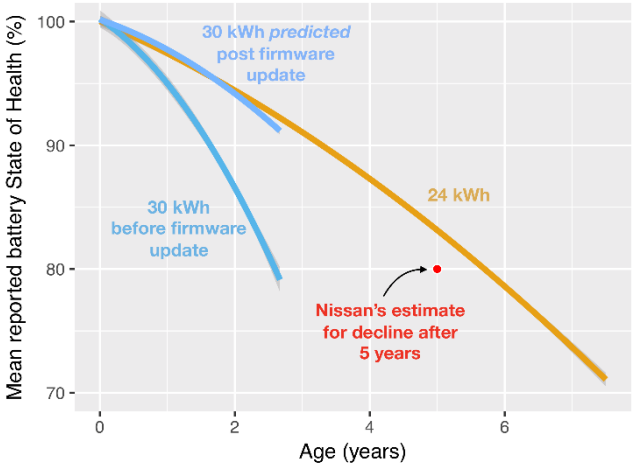

Figure 3.4: Trendline for reported SOH vs age in years for Gen1 and Gen2 Version of Nissan Leaf. 30 kWh Gen2 vehicle shown before and after firmware update to SOH estimator [31].

In addition, the SOH algorithm's function is unknown to the public and can be changed in-between measurements with an update, invalidating data collected previously since values are not comparable anymore [32]. In Figure 3.4, the "Flip the Fleet" project's reported dataset is shown, with the SOH values derived from the BMS over time [31]. The data showed substantial degradation suggesting an average life until 70 % SOH of only three years. After a software update to the SOH estimator on the vehicles, the values sharply changed.

Whilst laboratory-scale measurements rely on destructive, *ex-situ,* or *in-situ* experiments with preselected cells detached from their commercial application, field and usage data can be directly utilized *in-operando* with no need for further experimental efforts [33]. A metric for homogeneity commonly tracked from large sets of field data is the capacity variation between batteries, either tracked within the application or afterwards. This data is highly interesting for assessing the real-world degradation behaviour of batteries without accelerated ageing and with more variance on the stress factors such as climate or usage profile. Many manufacturers log data from their battery systems, but this data is rarely presented [30] and not published to the author's best knowledge. The battery community would greatly benefit from the release of large datasets.

Usage Data

In Liaw *et al.* [34], trip data from 18 vehicles were recorded and analysed for the specific use of each vehicle and differences in climate and other stress factors on the battery. For in-depth data on inhomogeneities within a battery pack, disassembly and measurement of each component are possible. Schuster *et al.* [35] disassembled two vehicle battery packs, tested the capacity of aged 954 cells and compared them to 484 new ones. On a smaller scale, 152 notebook batteries with a total of 1034 cells were dissembled by Salinas *et al.* [36], reading the capacity, manufacturing date and cycle count for each cell from the BMS chip. To the author's knowledge, system disassembly has only been reported for at most a few large-scale battery systems, giving a good inside of cell-to-cell variance within the specific pack but not for the variation in between multiple packs.

3.2 Origins of cell-to-cell variation and inhomogeneities

Inhomogeneities can occur in various regimes of the battery pack. The wiring resistance can vary at the pack or module level depending on the location within the pack and welding process [37]. But the inhomogeneities are linked since local defects induce change on the cell level [38], [39] and lead to cell-to-cell variation. Within the cell, both electrodes are made from heterogeneous materials with different particle sizes, binder compositions, and macrostructures.

From the fabrication of electrodes to the assembly in cells followed by the assembly of packs, it is impossible to achieve 100 % consistency with a zero-fault design, leading to intra- and inter-cell variations. During material synthesis, micro-tolerances or variations, among others, could lead to differences in structure, composition, or morphology [40]. Internal non-uniformities, such as disparities in architecture, composition or calendering, might affect the initial performance of electrodes of which assembly and winding can also induce inhomogeneous degradation [41], [42]. At the pack or module level, variations in wiring resistance, welding process, connectors, and environmental factors also influence the overall performance and degradation [43], [44] by affecting the local state of health, temperature, or current distribution. This first chapter presents a description and assessment of root causes, mechanisms and effects of

inhomogeneities scaling from the materials to the electrodes, then to the cell level and battery packs.

3.2.1 Material and Electrode Level

Microstructure and Composition

The electrode composition, microstructure, and architecture play a key role in shaping cell performance. Battery electrodes are complex and require active materials for capacity, additives for electronic conductivity, binder to maintain mechanical integrity, and porosity to allow ionic conductivity. Transport parameters such as ion diffusion and ionic and electric conductivity highly depend on the different pathways through the electrodes [45]–[48]. Any defects or irregularities in the electrode materials can cause local inhomogeneities that directly affect the performance, durability and safety.

The first critical source of these local inhomogeneities stems from the base materials themselves. Manufactured electrodes are affected by the characteristics and the quality of the precursor materials. This includes, among others, inhomogeneities in composition, purity, defects, and morphology. Several authors have indirectly investigated the impact of these inhomogeneities on cell performance. Harris et al. [41] showed that the structure of the graphite electrode from a commercial laptop battery was non-uniform, comprising of high and low tortuosity subregions. Low tortuosity regions were suspected to be subjected to higher Li^+ ions concentration, increasing local current density and leading to local overcharging [49]. This could, in turn, cause structural disordering or cracking of the electrode and lithium plating [50], [51], but also lead to temperature gradients. Vice versa, high tortuosity regions could deter Li^+ ions and cause some areas to be left delithiated, lowering the battery's capacity [52], [53]. Müller et al. [54] found microstructural inhomogeneities between graphite electrodes from different manufacturers at different length scales (Figure 3.5). Differences in grain size (Figure 3.5a) lead to different porosity (b) and tortuosity (c) values between electrodes. In addition, within an electrode, tortuosity also appeared to be anisotropic (Figure 3.5c), with higher values in the direction perpendicular to the current collector (TP on Figure 3.5c). Samples taken millimetres apart were shown to have different overpotentials during lithiation, which can cause the potential of the electrode to drop below 0 V vs Li^0/Li^+, triggering lithium plating.

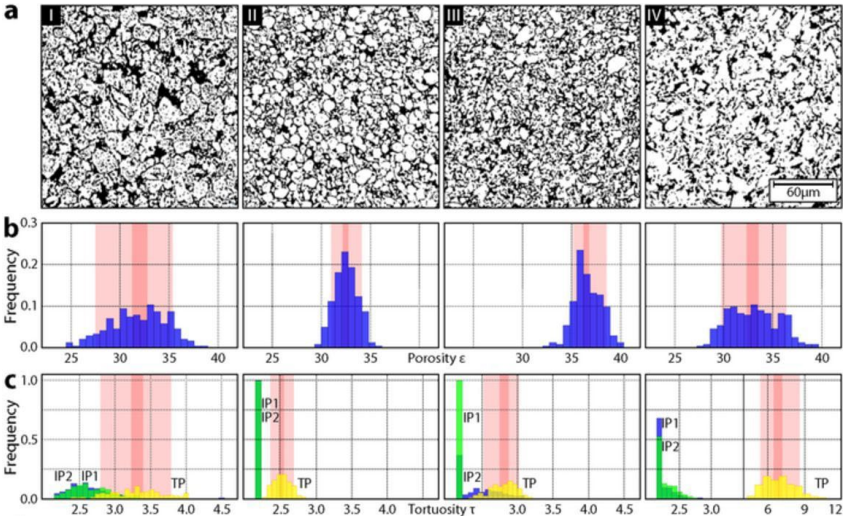

Figure 3.5: Tomogram results of one sample of four different negative electrodes revealing the types of graphite particles with porosity and tortuosity. IP1 and IP2 correspond to two in-plane directions while TP corresponds to the through-plane direction (modified from CC BY Müller et al. [54]).

Dubarry et al. [55] and Pavoni et al. [56] showed that grain size distribution could also drastically affect the kinetics of the electrochemical response. Yang et al.'s [57] in-situ optical observations revealed gas and electrolyte filled defects in the electrodes that affected Li^+ ion diffusion. Gas-filled defects decelerate Li^+ ions while electrolyte-filled defects accelerate them.

This phenomenon also contributes to uneven Li^+ ion distribution. Liu et al. [58] proposed to predict the occurrence of lithium plating by analysing the shape and size of localised inhomogeneities. Results show that, for equal surfaces, areas with larger inhomogeneities were more degraded than areas with clusters of smaller inhomogeneities. Pouraghajan et al. [59] found a strong dependence between ionic/electronic conductivities and cell chemistry. Differences in specific areas also affect Li+ ion transport and can lead to inhomogeneous distributions of current and eventually to the cell's failure [28,30,31].

During cycling, microcracks can also occur in the active material because of the volumetric changes associated with Li^+ intercalation. Concentration gradients within grains leading to localized volumetric changes are believed to be the fundamental root cause of the microcracking and the fracturing and cracking of

electrodes [60], [61]. This affects electrode tortuosity and electronic resistivity. Microcracks were shown to happen on graphite [62], [63], silicon [64]–[66], and some positive electrode (PE) materials [33,39,40]. Several studies observed increased polarisation and poorer electrical contact between active particles and the current collector. However, this electrochemical milling does not always result in worsening performances as it could increase the number of accessible intercalation sites, decreasing electrode tortuosity by opening pores and creating new ionic pathways. Birkl et al. [67] showed that graphite electrodes in Graphite//$LiCoO_2$ (LCO)–$NiMnCoO_2$ (NMC) pouch cells that were non-uniformly lithiated exhibited a higher capacity than the homogeneous cell. Dubarry et al. [68] found that electrode cracking could improve the kinetics of an LFP electrode by increasing the specific surface area of the grains.

Electrode Fabrication

Beyond the materials, proper fabrication of electrodes is also essential to obtain a consistent design. As shown in Figure 3.6, the manufacturing process of lithium-ion battery electrodes involves many steps such as the weighing of active materials, the application of the slurry on the current collectors, and the calendering process to smoothen and flatten the electrodes [9]. These steps must be done with precision to achieve consistent porosity and tortuosity. Improper mixing of the electrode slurry can lead to the inhomogeneous distribution of the active materials and additives. When coating the electrodes after the desired formulation is obtained, Higa et al. [69] reported that active material was more uniformly distributed on the electrode when slurry viscosity and heating power were higher. In [70], Lenze et al. described the impact of deliberate variations within manufacturing parameters on the performance of lithium-ion batteries. Four sets of cathode recipes, each with different active mass loading and calendering settings, were prepared. The evaluation of the resulting energy and power density show influence in order of magnitudes and high sensitivity. With similar results, Dreger et al. [71] compared different dispersing procedures and their impact on performance. Kenney et al. [72] set out to link the impact of variations in the electrode manufacturing process (electrode thickness, electrode density and active material) to the capacity of lithium-ion battery modules. Recent optimization work from Rynne et al. [73] showed the potential for the design of experiments (DOE) in electrode formulation.

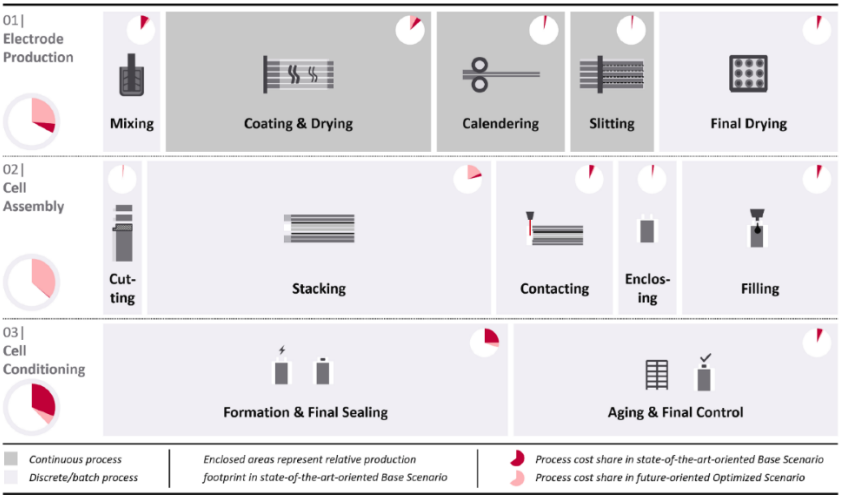

Figure 3.6: Manufacturing process steps of a lithium-ion pouch cell (CC BY Mauler et al. [74]).

The group studied almost 100 different electrode formulations and was first to report empirical equations linking electrode microstructure to cell behaviour. Results indicate that higher cell performance is linked to high active material content with a small fraction of conductive additives and minimal binder content. Several groups investigated the influence of the calendering process on the pore size distribution and particle deformation, like Haselrieder et al. [75], Ngandjong et al. [76] and Kang et al. [77]. Schmidt et al. [78] studied highly compressed NMC electrodes and found optimum calendering/compression rates necessary to obtain high-capacity retention while being able to deliver good power and long-term performance. Production parameters, therefore, must be tightly controlled to ensure consistent quality.

Although much work has been done in material synthesis and processing, further engineering and optimization [73] of the electrode microstructure, especially with the help of modelling [79]–[81] and of new machine learning techniques [82], is vital to achieving high homogeneity and high transport parameters to minimize the effects of inevitable manufacturing tolerances—whether it be large scale or laboratory scale manufacturing—on the development of high-performance cells.

3.2.2 Cell Level

A typical commercial cell is far more complex than a simple schematic with two electrodes separated by a separator. During cell assembly, process-related inaccuracies can also cause the cells to behave inhomogeneously [83]. These homogeneities are also influenced by the cell construction -cylindrical, prismatic or pouch- because of the variations in the production process between the different formats. For the classic cylindrical 18,650 cells, once the electrodes have been sized accordingly, the components are assembled into a separator-negative electrode-separator-positive electrode stack then wound into a jelly roll. The jelly rolls are then inserted in cylindrical cases, and conducting tabs are welded on the terminals. Prismatic cells generally consist of long stacks of electrodes similar to cylindrical cells but folded and pressed to fit into a hard rectangular casing instead of being wound. Pouch cells do not have a rigid enclosure and use stacked paralleled electrodes without winding or folding. The negative (NE) and positive (PE) electrodes are cut into individual rectangles stacked alternately and separated by the separator, sealed in an aluminium pouch. The assembly process of a lithium-ion battery is very intricate [74], and Figure 3.6 highlights the high number of necessary steps for a pouch cell.

Tight measures must be put in place to ensure minimal variations. Leithoff et al. [83] studied the effect of electrode deposition accuracy during the stacking process and found a linear relationship between the nonoverlapping of the electrodes and discharge capacity. Results by Paxton et al.'s [84] reveal asynchronous discharge behaviour and incomplete electrode utilization. Ziesche et al. [85] noticed that new cells already showed cracks on the PE, most definitely after-effects of the production process. The cracking is accentuated when moving towards the cell centre, where the electrode's bending radius is higher.

Slight variations are impossible to avoid, and cells from the same production line are usually sold in different grades to account for intra-batch inhomogeneities. Ranging from smaller-scale testing [86]–[90] to larger-scale testing [35], [40], [90]–[95], many studies reported cell-to-cell variations within batches. Dubarry et al. [93] were among the first to conduct systematic campaigns of ctcV characterization on new batches of cells. They focused on identifying the origins of ctcV and characterized them with three independent attributes: the amount of active material, the polarisation resistance, and the rate capability. In [94, p. 1], the researchers also investigated the variations in the electrode loading ratio and

SEI induced electrode offset. Rumpf et al. [91] addressed the much higher variation between batches than within a batch. From the labelling of cells, two batches could be identified with production dates one month apart. This could already induce ageing before testing. Differences in cell-to-cell variation could also be shown over a three-year production cycle in Schindler et al.'s [40], where three batches of cells were purchased 14-months apart. Most studies [61,65,66,68] showed that discharge capacities tend to follow and keep a normal distribution whereas the ones for polarisation are skewed with a larger tail towards higher resistances. Higher ctcV are expected for prototype cells and commercial cells with low volume production.

Cycling

Mechanically induced stress from the cycling can also cause inhomogeneities to arise. Through the charging and discharging regimes, Li^+ ions intercalation and deintercalation are often associated with volume changes, leading to mechanical stresses. An advantage of cylindrical cells is high mechanical stability as their shape allows the even distribution of internal pressure. However, when the pressure build-up is too high, the uniformity of the jelly roll can be compromised. Carter et al. [96] investigated mechanical failure in cylindrical cells by comparing cells with and without mandrels. At the pristine state, mandrel-less cells show less deformation than mandrel cells. However, the jelly roll in mandrel-less cells is more prone to mechanical collapse after cycling. Pfrang et al. [97] and Willenberg et al. [98] studied the morphology of the jelly roll of cylindrical cells. Pfrang et al. [97] noticed that the deformation almost always occurred between the PE tab and the inner pin. It was concluded that the inhomogeneous architecture of the cells is caused mainly by the PE tab deformation, which is the result of thickness variations of the NE and PE during charge/discharge cycles. Postmortem analysis showed delamination of the active material in the high-stress area and creating gaps between the aluminium current collector and PE coating, which contributed to the loss of active material (LAM). Willenberg et al. [98] correlated jelly roll deformations to cyclic ageing, stating that there were no signs of deformation at the time of delivery. However, Bach et al. [42] noticed that even new cells exhibit signs of jelly roll deformation and linked the cause to the positioning of the tabs. The slight bulkiness of the tabs deforms the jelly roll and creates low and high-pressure areas, leading to separator inhomogeneities [99], [100]. Lithium plating

was primarily observed in high-pressure areas. Mühlbauer et al. [101] focused on electrolyte distribution in cylindrical cells. Systematic results reveal lower lithium concentrations at the top and bottom of the aged cells, possibly caused by mechanical deformities or inhomogeneous pressure or temperature gradients. Lower lithium concentrations were also observed in the outer region of cylindrical cells due to the inhomogeneous distribution of the liquid electrolyte [102], [103]. The rigid case of prismatic cells helps them withstand high external mechanical stress situations; however, the folded sheets in the case experience high levels of internal stress, especially at the edges.

Figure 3.7: a) X-ray CT scan of electrode deformation in the prismatic cell; b) missing insulating tape on the cathode tabs; c) SEM cross-section of an anode tab weld (CC BY Loveridge et al. [104]).

Coupled with manufacturing inhomogeneities, such as welding burrs, high internal stress can damage electrodes or cause uneven electrolyte distribution that can trigger unwanted lithium plating, leading to internal short-circuits and thermal runaway. This happened to be the root cause of the well-known fire incident with the Samsung Galaxy Note 7 batteries [104], [105] shown in Figure 3.7.
Several authors investigated temperature gradients across cells. Werner et al. [106] compared cell degradation under spatially homogeneous and inhomogeneous temperature distributions and observed different ageing mechanisms between the two conditions. Uncontrolled inhomogeneous elevated temperatures can cause undesired side reactions that can accelerate degradation or result in thermal runaway [44]. Osswald et al. [107] used modified commercial cylindrical cells to study the influence of temperature on current distribution, leading to SOC inhomogeneities at different locations on the electrodes. The group recorded larger inhomogeneities for increasing temperatures and C-rates. Grandjean et al. [108] support Osswald's findings that thermal gradients increase with increasing C-rate and decreasing temperature. He also noted that the top of the pouch cell, where the tabs are located, is not the hottest area. A recent study by Carter et al. [109] on interelectrode thermal gradients demonstrated how they could induce certain battery degradation mechanisms. The electrochemical

reactions within a cell are highly temperature-dependent; therefore, thermal gradients can create a capacity mismatch between the PE and NE and accelerate electrode degradation. Paarmann et al. [110] add to this claim by stating that the same temperature difference has a higher impact on the current at lower temperatures.

During their lifetime, cells can be subject to various cycling—regular or abusive—conditions triggering specific degradation mechanisms that reveal themselves as inhomogeneities. This repeated process can initiate spatial inhomogeneities [111], [112]. Gas formation is known to be a byproduct of electrolyte reduction [113]. Michalowski et al. [114] observed lower chemical activity in the centre of a pouch cell and attributed it to a gas bubble creating a low-pressure zone, reducing Li-ion transport by poor contact. Similarly, in a pouch cell study performed by Devie et al. [115], [116] where gas evolution was observed, they attributed the simultaneous loss of active material (LAM) on both electrodes to the interruption of the ionic conduction pathways between the PE and NE. Displacement of the gas bubble to the top of the stack allowed the inactive areas to become active again, regaining previously lost capacity.

All of the above affect the cells, and the impact of these variations is significant. In selected cells from the same production batch with little initial cell-to-cell variability, tested under the same testing conditions [61,93,94], inhomogeneities arise and lead to significant deviations from one another. Baumhöfer et al. [86] showed that ageing 48 cells issued from the same production lot using an identical protocol resulted in large inhomogeneities, with the worst cell having a cycle life 25 % shorter than the best cell. In addition, little to no correlation was found between initial cell-to-cell variation and later degradation of the cells during cycling [117], [118]. For this reason, special attention must be exerted when dealing with battery pack assembly and highlights the need for accurate material-based state-of-health (SOH) estimation techniques [119].

3.2.3 Pack Level

Battery packs are often divided into multiple modules in series or parallel and have a battery management system to monitor performance. It is the final shape of the battery system that is deployed for the chosen application. Such assemblies are necessary to meet rigorous power and energy requirements, and proper cell balancing and their appropriate connection are critical factors to monitor to

prevent the rise of inhomogeneities. Cylindrical cells are usually welded to one another in large quantities allowing for simple construction. While space management remains somewhat suboptimal, thermal management in a pack is easier due to the spaces between cells. It is one of the cheapest methods for producing large lithium-ion battery packs. Prismatic cell battery packs can store more energy within their volumes; thus, they offer a higher energy density and can be more powerful without using more space. The box-like shaped cases are ideal candidates for spatial optimization, making the best use for available space but leaving little room for proper thermal management. Pouch cells make the most efficient use of space because they do not have any metallic enclosure, but they are usually sensitive to external stress factors and require alternative support during assembly.

Inhomogeneities in modules and packs can arise from several factors. Depending on the material properties and contact geometry of the battery casing and tabs, different welding techniques could be used to ensure proper connection between cells and proper assembly of battery packs. Brand et al. [120] presented an overview of three main welding techniques: resistance spot welding, ultrasonic welding and laser beam welding, with details on their influence on contact resistances in various types of batteries and battery casings. In all cases, the heat was very localized, which did not affect the health of the cells. Taylor et al. [121] discussed the effects of connectors and connections on the resistance of the circuit and, although the study was done for characterization experiments, their results are applicable and need to be taken into account. If done incorrectly, the integration of unmatched cells, poor cell connections or an asymmetric module design can lead to inhomogeneous currents flowing through the module [122], inducing temperature gradients which lead to inhomogeneous degradation. Rumpf et al. [123] studied the influence of ctcV on the inhomogeneity of battery modules. The importance of a symmetric module design was highlighted to obtain symmetric current distribution. They also observed that an asymmetric design of cell connectors could significantly impact inhomogeneous current distribution than ctcV. Inhomogeneous current flow due to uneven contacts was also studied by Wang et al. [124]. They stated that inhomogeneous current flow through parallel cells is induced by the resistance of the intercell connecting plates. This caused cells to be discharged unevenly, therefore, lowering the terminal voltage of the module, affecting its usability. Offer et al. [125] backs the results of the previous studies by showing that uneven current flow in a pack is more likely to

come from a defective intercell connection plate resistance than a cell with an abnormally high impedance. A pack containing 504 cells in a highly paralleled configuration was tested, and it was shown that a single high intercell connection resistance was setting off significant SOC variations between the cells in the same parallel strip, leading to the premature ageing of the pack. A recent review of SOC estimation methods in lithium-ion battery packs summarized the impact of cell inconsistencies due to manufacturing and welding processes on pack performance and SOC estimation [126].

The implementation of ctcV in battery pack models [127]–[129] helped show their impact on a multiscale level, and they were found to have a much higher impact on cells connected in series rather than in parallel. Experimentally validated simulations by Liu et al. [130] placing a cell with a high internal impedance closest to the load where the currents are higher provide better cell-to-cell current distribution because higher internal resistances lead to less current through the cell [131]. On the other hand, placing a high internal impedance cell furthest from the electrical load, further increasing the wiring resistance, would be detrimental to the pack's performance, reducing its capacity as the other lower impedance cells would reach the terminal voltage first. Neupert et al. [131] studied the current distribution depending on the position of cells with different impedances in a parallel configuration. Surprisingly, cell position in the parallel strip has a more significant influence than the cell's internal resistance at a specific position. Gogoana [88] linked resistance mismatch in parallel connected cells to capacity fade, while Grün et al. [43] researched the importance of the cell’s internal and contact resistances ratio.

Liu et al. [130] and Wu et al. [132] observed that inhomogeneous current flow drives localized heat generation, especially in cells closer to the load points of the pack. Dubarry et al. [133] used data from a deployed grid-scale battery energy storage system containing more than 2500 batteries to examine temperature gradients between modules and found a maximum temperature variation of 16.5 °C between modules. Other studies have attempted to correlate capacity loss with temperature variations [134], [135]. These thermal gradients could aggravate cell degradation and further accelerate the ageing of the concerned cells, jeopardizing the performance and safety of the pack. Several other cell sorting studies were made to achieve better cell-to-cell consistency and push for longer cycle life [136], [137]. Careful arrangement of cells in modules and modules in a

pack is primordial in assuring equal current flow throughout the module while minimizing thermal gradients, especially when high currents are in play. Cooling strategies are often thought of to help mitigate the effect of unwanted thermal gradients. Wang et al. [138] discussed multiple heat dissipation module configurations for cylindrical cells with and without forced air cooling and concluded that cubic structures are the best choice for cooling capability and cost. The temperature distribution in the module also depends on the position and airflow of the cooling source. Cells nearer to the cooling source are inherently be cooler than those farther away. Effective heat dissipation and insulation technology are vital to adjust the battery pack's temperature and help them reach their optimal operating temperature, reducing inhomogeneities while improving electrode kinetics.

All these variations present the cells within a pack with different ageing conditions, which might exacerbate or inhibit specific degradation mechanisms. Although path dependence is not considered an inhomogeneity in itself, cells/modules following different degradation paths when they are supposed to be working homogeneously can be considered inhomogeneous at the pack level. Path dependence poses an issue to predict the ageing of cells in a battery pack. These issues arise because cells are not subject to similar conditions all the time: variations in cell assembly, calendar ageing between cells from different batches, thermal gradients, current distribution, etc. Several studies about path dependence [139]–[142] have been conducted. Results show that different cycling conditions induce different mixes of degradation mechanisms such as loss of lithium inventory (LLI), loss of active material at the negative electrode (LAM_{NE}) and loss of active material at the positive electrode (LAM_{PE}). The complex interaction between the different degrees of these losses will all lead to significantly different ageing timelines. It is, therefore, challenging to associate cell constant-current laboratory tests to sporadic driving conditions [34], [143]. Path dependence is particularly notable when dealing with second-life batteries as they have been already degraded over time [144], [145]. Remanufacturing or refurbishing processes must ensure pack stability, but it can be challenging when the first life is not recorded.

3.3 Methods to track inhomogeneities

3.3.1 Large-scale research facilities

Large-scale research facilities generally allow for comprehensive investigations because they offer much higher brilliance for their spectroscopic measurements, a term that describes both the brightness and the angular spread of the beam. Synchrotron has brilliance more than a billion times larger than a standard laboratory X-ray source. Higher brilliance allows more resolution in measurements, penetrates deeper into the matter, studies much smaller features, or scans large areas much faster.

High-energy X-ray

High-energy X-ray (HEX) with energy levels over 80 keV can be used to nondestructively probe bulk probes and perform experiments with large format cells in situ and operando [146]. Paxton et al. [143] used a polychromatic synchrotron x-ray source to quantify inhomogeneities in situ to perform energy-dispersive x-ray diffraction (EDXRD). Lithium cannot be tracked with this technique, but the lithiation dependent structure of the materials can be monitored.

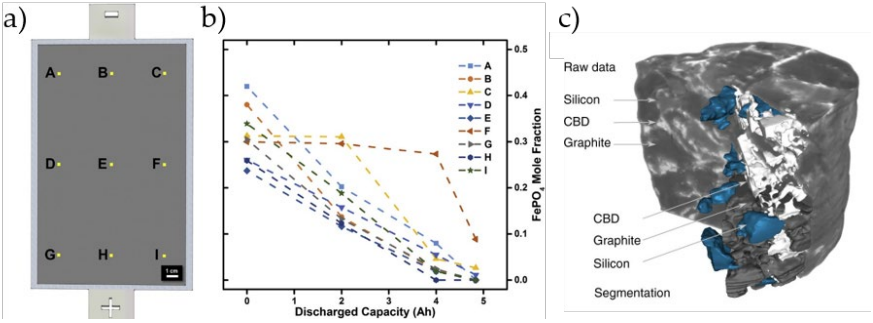

Figure 3.8: a) Location of bulk measurement points and b) spatial inhomogeneity during discharge in LFP Pouch Cell. Reproduced with permission from [48] Copyright 2015, Elsevier. c) 3D-reconstruction of tomographic raw data and segmentation of silicon-graphite anode from a transmission X-ray tomographic microscope. Scale bar 15 µm. (CC BY 4.0 Müller *et al.* [147]).

In [148], the distribution of the ratio of $FePO_4$ to $LiFePO_4$ at a particular region was used to track the local state of charge (SOC). It must be noted that with this

technique, all sheets of the cell are measured at once, and an average phase ratio is determined. An example of the determined phase ratios from [148] is presented in Figure 3.8 a) and b). The inhomogeneous discharge behaviour is visible as locations C and F are not at the same SOC as the rest of the electrode.

X-ray tomography

X-rays from synchrotrons can also be used for the 3D-reconstruction of electrodes as performed by Müller et al. [54] with synchrotron radiation X-ray tomographic microscopy (SRXTM). Four commercial graphite anodes were measured on a µm-level, and, amongst others, porosity, tortuosity, and particle size distributions were evaluated. In addition, this technique was used for determining the structure of silicon graphite negative electrodes and their 3D-reconstruction [147]. An example of the obtainable reconstructions is presented in Figure 3.8c).

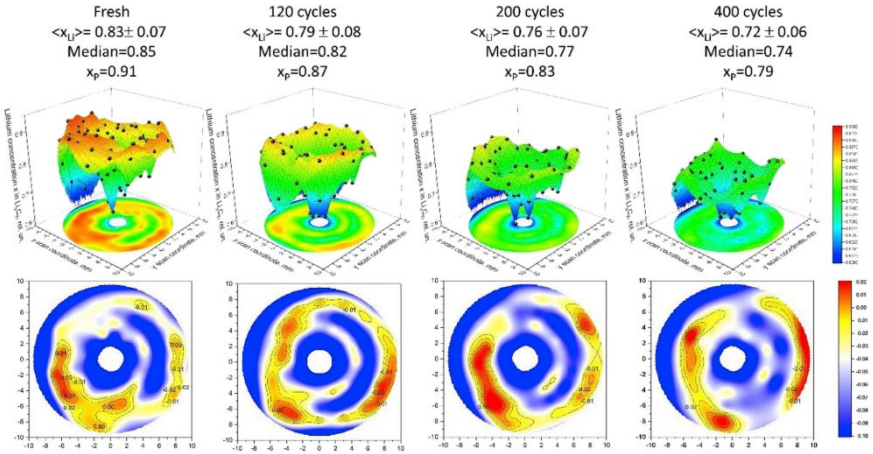

Figure 3.9: Lithium distribution as cross-section determined by differences of reflections of LiC_6 and LiC_{12} phases in graphite with spatially resolved neutron diffraction. Over cycling, inhomogeneities enhance. Reproduced with permission from [149] Copyright 2020, Elsevier.

Neutron diffraction

Neutron diffraction offers advantages such as higher resolution for small atoms like lithium or the distinction between isotopes. Neutron reflections of the LiC_6 and LiC_{12} phases of graphite anodes also differ, approximating lithium

concentration [150], [103]. Since the measurement can be performed without destroying the cell, the lithium distribution can be tracked during cell degradation [151]–[153]. With spatial resolution, this technique can be used in situ and 3D, for example, to determine lithium distribution in cylindrical 18650 full cells [149], [154] as shown in Figure 3.9.

3.3.2 Laboratory scale tracking

Compared to the very few research facilities with large instruments, laboratory-scale devices and methods generally show much more widespread availability and can be performed in most battery research laboratories. In this chapter, laboratory-scale approaches with a specific focus on identifying and characterisation of inhomogeneities are presented. For a more general perspective on post-mortem techniques, the reader is referred to Waldmann *et al.* [155], Lu *et al.* [156] and Harks *et al.* [157].

Cell Modifications

To investigate local variations in the internal state of a commercial cell, a widespread approach is modification and reconfiguration of the cell. The modification covers the introduction of sensors and reference electrodes into the cell. Fleming *et al.* placed temperature sensors inside a commercial cell to capture temperature gradients [158], while McTurk *et al.* [159] demonstrated the insertion of a wire reference electrode into a commercial pouch cell. Another approach was used by Osswald *et al.* [107], where the current tabs were separated and used to measure space-resolved EIS measurements as well as temperature changes during cycling [107]. Reconfiguration covers the extraction of single-cell parts from a commercial cell, like one of the electrodes or the separator, and the reassembly of a new cell of a new format (mostly coin cell format). This allows to evaluate the electrochemical behaviour of aged samples whilst using reference compounds for all other parts. The new cell can then be evaluated as any other cell. Spatial resolution can be achieved by using samples from different regions of the commercial cell. In this context, Wang *et al.* [160] performed cycling tests and impedance measurements at coin cells obtained from different regions of a commercial 18650 cell that aged inhomogeneous, whereas Sieg *et al.* [50] created coin cells from a commercial pouch cell to evaluate local deviations in the differential voltage analysis caused by inhomogeneous lithium distribution and

local cell ageing. With the spatial resolution of the measurements ageing maps of the electrode sheets were created, showing the location of ageing gradients.

Spatially resolved bulk measurements

Some of the measurement methods presented in this chapter can only identify bulk values for the whole sample introduced into the measurement, giving no opportunity to identify the spatial resolution of inhomogeneity within the sample. To apply these measurement methods for the evaluation of inhomogeneity, units of interest for inhomogeneity (e.g., an electrode sheet) have to be subdivided into a set of samples covering the area of the whole unit. These samples are then evaluated by bulk measurements independently. The spatial distribution of the samples hereby allows for the determination of the spatial resolution of the quantity measured by bulk measurements within the unit of interest.

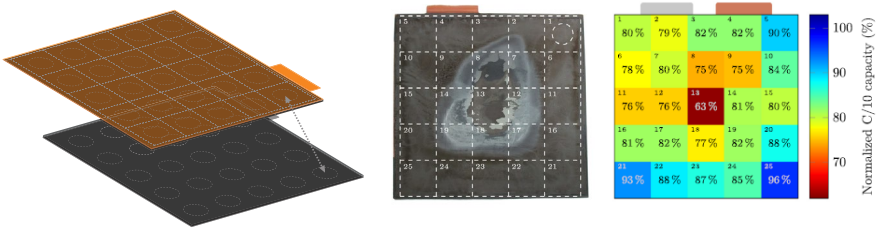

Figure 3.10: Spatially resolved capacity measurement with coin cells. a) schematic of samples, b) location of anode samples, c) Full coin cell capacity map. Reproduced and modified with permission from [50] Copyright 2020, Elsevier.

Sieg *et al.* [50] used this approach to determine the inhomogeneity of capacity distribution within a pouch cell by creating coin cells from an electrode pair and evaluating coin cell capacity. Figure 3.10 shows the spatial distribution of the samples a), the optical changes on the anode b) and the capacity distribution c) for the electrode pair. Further spatially resolved bulk measurements were performed by Warnecke [161] by the use of inductively coupled plasma optical emission spectroscopy (IPC-OES) on different areas of the anodes to track inhomogeneous manganese distribution caused by manganese dissolution at the cathode.

Visual inspection of post mortem cells

For qualitative evaluation of inhomogeneities within a cell, visual inspection of the electrodes and separator can be used to overview inhomogeneous cell behaviour. Since graphite presents different colours depending on the lithiation stage, cells with graphite anodes can be inspected visually for inhomogeneous lithium distribution [162], [163] an example from Spingler *et al.* [164] is presented in Figure 3.11 a). In addition, lithium plating as an extreme form of lithium concentration heterogeneity can be seen in some cases [58], [165].

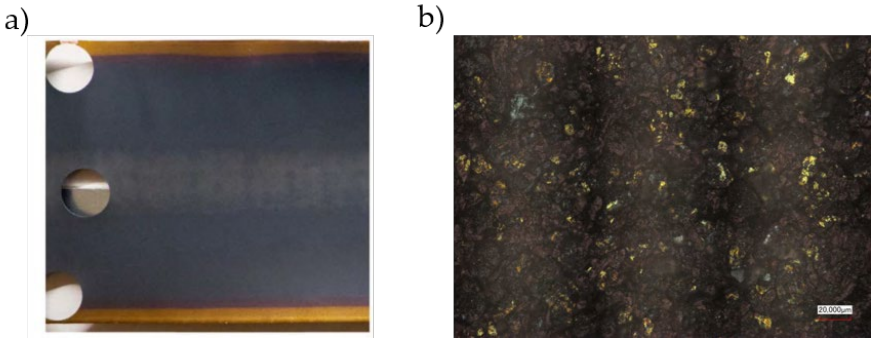

Figure 3.11: a) Part of the anode of an 18650 cell with coin cell probes taken in different locations of the cell. The outer part of the electrode shows a different lithiation than the middle part. (Modified from CC BY 4.0 by Spingler *et al.* [164]) b) optical microscopy of the outer part of an anode showing individual particles with different lithiation. (CC BY 4.0 by Käbitz [166]).

Covering layers formation [167], [168], or electrode delamination [98] have also been reported. Visual inspection of cell inhomogeneity can be further supported using light, as seen in Figure 3.11 b), where Käbitz [166] used laser microscopy to allow for higher degrees of magnification. Ecker et al. [46] also applied laser microscopy to characterise lithium plating in commercial 40 Ah pouch cells.

Electron microscopy

Compared to light microscopy, scanning electron microscopy (SEM) allows for higher magnification and can track inhomogeneities on a material level. This includes uneven particle sizes, particle cracking, delamination [104] or deformation [169]. While SEM cannot penetrate active materials, Focused Ion

Beam milling (FIB) can be applied to erode the active material layer by layer and thus allows for 3D-imaging of electrode structures using FIB/SEM [147]. Furthermore, SEM can be coupled with an energy-dispersive X-ray spectroscopy detector (EDX) to allow for spatially resolved determination of elemental composition in the active material. Burow *et al.* [170] applied SEM/EDX to detect inhomogeneous lithium plating in automotive cells cycled at low temperatures.

Computer tomography

Computer tomography (CT) uses X-rays and moving sample to reconstruct a 3D representation of the cell. On the laboratory scale, it can be used with lower resolution (up to 100µm resolution) for full cells and parts of a cell with higher resolution. The main field of application for CT is the non-destructive geometric depiction of the cell. This allows for the spatially resolved identification of deformations caused by uneven stress within the battery or by delamination. Computer tomography has shown multiple times the deformation of the jelly roll in cylindrical cells [96], [98], [168], [169], [171]. A nanoscale CT can also be used to see heterogenous particle cracking and covering layer formation [172], [173]. Li and Hou also reported a correlation between their capacity measurements and CT image data [174].

Magnetic Resonance

Magnetic resonance spectroscopy techniques enable the identification of material compositions inside lithium-ion batteries. This allows for the identification of phase compositions and active and passive materials degradation due to cell ageing. The magnetic susceptibilities of many cathode materials depend upon their lithiation state [175]. Ilott *et al.* used Magnetic Resonance Imaging (MRI) on small 600 mAh pouch cells with an induced magnetic field being changed as a function of the state of charge [175]. With various magnetic field maps taken at different charge levels, inhomogeneous lithium distribution within the cell could be found. In addition, defective cells could be identified. While MRI uses the intensity of radiation, Nuclear Magnetic Resonance (NMR) analyses the frequency of the response signal. Krachkovskiy signatures from stages of graphite lithiation can be seen in NMR spectra [176]. Furthermore, NMR can be applied for the identification of electrolyte decomposition, as shown by Wiemers-Meyer *et al.* [177]

Acoustic measurement

Acoustic measurements can be used to gain information on the geometric structure inside a cell and the composition and lithiation of the active materials. The acoustic properties of electrode materials correlate with the state of charge due to changes in the density during lithiation. Using this property, differences in lithiation during usage were mapped by Robinson *et al.* in small pouch cells with spatially resolved ultrasound measurements coupled with CT measurements [112]. Bauermann et al. showed that Scanning Acoustic Microscopy (SAM) could visualize defects inside battery cells non-destructively. With characteristic acoustic impedances, inhomogeneities are detected and localized. SAM is best used on flat and thin battery cells and effects like gas formation with a high acoustic pattern sensibility [178]. Acoustic attenuation spectroscopy (AAS) can determine the particle size distribution post mortem by dissolving binders in electrode samples, thus transforming the active material into a particle suspension [56].

Electrochemical characterisation

Unlike many of the aforementioned methods, electrochemical characterization can be performed directly on the commercial cells with no need for cell opening nor sample extraction to generate bulk information about the full cell. Moreover, it can also be performed on electrode cutouts to allow a spatially resolved analysis of the electrochemical cell behaviour. Electrochemical measurements allow gathering information on the thermodynamic state of the cell as well as its kinetics. CtcV is usually characterised during a conditioning test at the beginning of testing [179]. In addition, those measurements are part of every ageing study and can reveal cell-to-cell variation over the lifetime of a cell [117], [180]. One such experiment is shown in Figure 3.12 a) from Baumhöfer et al. with 48 cells cycled under identical conditions. This test usually involves the assessment of the distribution of capacity, rate capability, and resistance [40], [87]–[91] to assess thermodynamic and kinetic variations.

The cells are usually fully charged for a capacity test and then discharged to the end-of-discharge voltage by a defined current. The integral of the discharge current over the discharge time is the resulting cell capacity and depends on the applied C-rate but converges to the theoretical cell capacity for low C-rates. To eliminate most of those influences during a capacity test temperature, current and

charge procedure should stay constant. Most manufacturers define a standard charge protocol for their cells, which should be followed. But for some high energy cells, manufacturers state unreasonably long charge durations to achieve the nominal capacity. Therefore, when comparing different cells, the charging procedure should be matched, for example, fixing the maximum charge duration. In addition, reversible capacity effects, as discussed in 3.4, need to be considered while testing and when evaluating the capacity estimations from capacity tests.

In addition to capacity tests, a second current rate should be used. A low current rate, also called quasi-open-circuit-voltage (qOCV), allows tracking changes in the qOCV over time. For the current rate and the associated discharge duration, a compromise must be found. Small currents and the associated long discharge durations are beneficial to decrease over-potentials within the cell and the overlapping of different processes within the cell. But measurement errors are integrated over the whole discharge duration, and therefore, the test should be as short as possible. Also, total test time needs to be considered, where long check-ups decrease the time available for the ageing conditions. Depending on the measurement equipment and cell type, a discharge time between 8-20 h is suitable [181]. Especially in chemistries with hysteresis in between charge and discharge curve, both charge and discharge should be recorded with small currents [182].

Rate capability can be characterized by the Peukert constant or a ratio of two different rates [179].

Another critical indicator considering ageing is the internal resistance as a measure of power capability. Like the capacity, pulse resistance is also highly influenced by external parameters like temperature, state of charge, or current [181]. There are several ways to measure internal resistance, such as electrochemical impedance spectroscopy (EIS), charge, or discharge pulses.

During the electrochemical impedance spectroscopy, an alternating excitation current of defined frequency is applied to the battery, and the voltage response recorded. The values are transformed into the frequency domain and typically depicted in a Nyquist plot. One central application for EIS measurements is the creation of battery models of high dynamics [183] (see 6.1), as well as tracking the state of health and evolution of model parameters [184]. In addition to single-frequency EIS measurement, several frequencies can be superimposed in the time domain to measure simultaneously [185].

The pulse resistance describes the linearised resistance. A charge or discharge pulse is applied, typically between 10 or 30 seconds, and the resulting voltage

drop investigated. Before a pulse is used, the cell should be relaxed to minimize the error due to prior testing artefacts. The voltage difference between before and during the pulse is divided by the pulse-current to calculate the resistance. From a 30 second pulse, several resistances can be calculated; for example, by using the voltage after 2, 10, and 30 seconds [186]. Pulses are used to determine the available power and state of health concerning power capability. A typical end-of-life criterion for resistance is 200 % of initial resistance equivalent to 50 % remaining power capability.

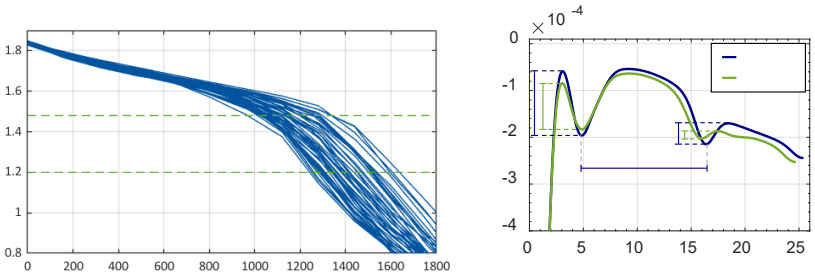

Figure 3.12: a) 48 cells under identical conditions focusing on inherent production caused cell-to-cell variance and capacity degradation over cycles; 80 % and 60 % of initial capacity are marked with green dashed lines. Reproduced from Baumhöfer *et al.*[86]. b) Differential voltage analysis on a 25 Ah cell to determine changes in the peak heights to quantify the homogeneity of lithium distribution (HLD) [126].

Lastly, the use of electrochemical voltage spectroscopies, differential voltage analysis (DVA) [187], and incremental capacity analysis (ICA) [188] were also shown to allow the visualization of differences between cells.

Inhomogeneities are hard to assess at the full cell level because of the bulk nature of the measurements. However, DVA and ICA were shown to offer some insight. Lewerenz *et al.* [189] observed some valley broadening using DVA, Figure 3.12(b), and associated them with growing inhomogeneities. If parts of the electrodes have a higher charge level due to an inhomogeneous lithium distribution, those areas show the peaks in the DVA later during a constant discharge [189]. As the overall voltage corresponds to all individual voltages, the steps in the discharge curve and peaks in the DVA should be less prominent in

inhomogeneous cells. ICA and DVA can also be used to visualise differences within cells in modules or packs [128], [190]–[193].
Another indicator for homogeneity within a cell or packs can be evaluated by tracking differences in rate capability over time [188], [194]. For this technique, the difference of rate capability, i.e. the extractable capacity at a certain current, is monitored for at least two current rates. A substantial increase in both capacities infers that parts of the active material are less accessible with high currents [194]. When applying this approach, it is necessary to verify that the resulting differences in rate capability are not just linked to an increase in resistance and to the rising overvoltage of successive discharges in the check-ups of the ageing test [179].

Characterisation of inhomogeneous cell degradation

As discussed in detail in Chapter 2.2.2, cell inhomogeneity can be strongly related to cell ageing and degradation. Thus, inhomogeneity resulting from typical cell degradation processes can be quantified by applying localized post-mortem methods for inspection of cell ageing phenomena presented in this chapter. Electrochemical characterisation methods are best fitted to characterise ctcV with further possibilities to investigate internal inhomogeneities by cell modification, spatially resolved bulk measurements and DVA/ICA. In contrast, the presented methods for visual inspection, spectroscopy and tomography are mainly applied to characterise inhomogeneities within a cell, such as lithium distribution and local degradation phenomena. Figure 3.13 illustrates the feasibility of detecting different degradation phenomena for the established post-mortem measurement procedures presented in this chapter. Furthermore, the spatial resolution of the measurement referred to as sensitivity is evaluated, indicating whether spatially resolved bulk measurements have to be performed to assess inhomogeneity.

				Cell level degradation			Electrode/separator degradation			Material degradation		
Method	cell inhomogen-ities	cell-to-cell variation	sensitivity	loss of active material	loss of lithium inventory	rise of inner resistance	growth of films on electrodes	clogging of pores	delamina-tion of electrode or separator	changes/ films on particle surfaces	particle cracks/ exfoliation	dissolution/ migration of transition metals
optical microscopy	yes	limited	surface	no	no	limited	yes	limited	yes	no	no	no
SEM	yes	limited	surface	no	no	limited	yes	yes	yes	yes	yes	no
EDX	yes	limited	surface	no	no	limited	yes	yes	no	yes	no	yes
XPS	yes	limited	surface	no	no	limited	yes	no	no	yes	no	yes
ICP-OES	yes	limited	bulk	no	yes	no	limited	no	no	no	no	yes
NMR	yes	limited	bulk	no	limited	no	limited	no	no	no	no	yes
XRD	yes	limited	bulk	limited	no	no	limited	no	no	limited	no	no
electro-chemical	limited	yes	bulk	yes	yes	yes	limited	limited	limited	no	no	no

yes limited no

Figure 3.13: Post-Mortem analysis methods. (modified from Waldmann *et al.* 2016 CC BY 4.0 [154]).

3.4 Reversible capacity loss

When evaluating ageing, only the long-term degradation trend should be considered. Effects that are reversible within a few months are not of interest for long-term trends. But in addition to irreversible capacity loss or resistance increase, part of the observable capacity reduction is reversible. One of the reasons for the reversible capacity loss is the passive anode effect. The effect was shown by Gyenes et al. [195] as a way to understand the abnormal behaviour of high coulombic efficiency tests, where efficiencies of over 100 % were measured. Figure 3.14 shows an anode and cathode with a red frame marking the active area of the full cell bounded by the cathode area. An equal or under-dimensioning of the anode in terms of the planar area induces edge lithium-plating at the anode due to local potential differences.

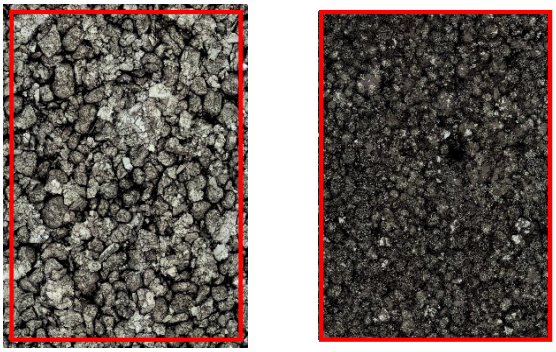

(a) *(b)*

Figure 3.14: Sketch of planar anode oversize within a lithium-ion batteries with graphite anode a) Anode with marking of cathode size, the outer area is coupled slowly (b) cathode.

The passive anode is only electrochemically connected but only weakly. Within a charge and discharge cycle for capacity estimation, this lithium is not accessible and is not shown in measured capacity [196], [197]. This is also true for real applications when the passive anode is highly lithiated, the actual driving range of an EV is reversibly decreased. When the outer anode-sheets are coated on both sides, and one of them has no counter-electrode, lithium-ion movement can still be detected after several hundred days [161].
Figure 3.15 shows several configurations of lithiated and delithiated active areas and anode overhangs. In Figure 3.15 a) the overhang is fully lithiated, and the

active area is empty. The cell voltage is low, and no more charge can be discharged. The cell spent some time at a high state of charge; the anode overhang was lithiated and discharged. If the cell is kept at this level, the overhang is slowly

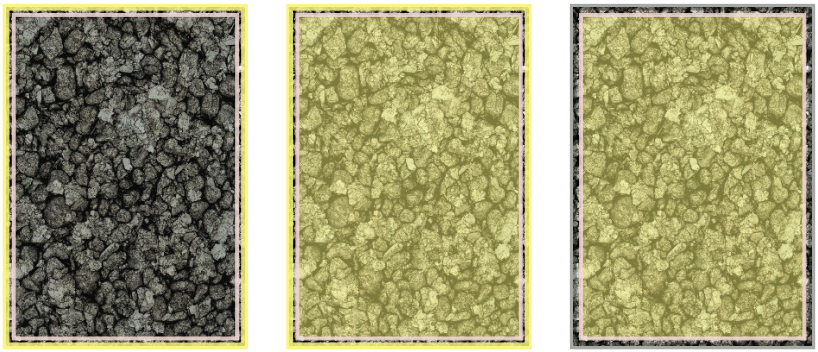

(a) *(b)* *(c)*

Figure 3.15: Effects of overhang a) overhang is fully lithiated, active area empty b) active area and overhang are fully lithiated, c) active area is lithiated, the overhang is empty.

delithiated, and the trapped lithium is converted into active lithium. In Figure 3.15 b) both the active area as well as the passive area are lithiated. Prolonged storage at a high SOC produces this state. In Figure 3.15 c), the overhang is not lithiated but the active area. In this state, following prolonged storage at a low SOC, more active lithium is available and visible in capacity testing.

In addition to the reversible effects of the overhang, capacity recovery due to re-homogenisation can be observed. Käbitz found a drastic recovery of measurable capacity [198]. The specific cell was part of the ageing matrix in [199] and cycled until an end-of-life criterion of 80 %. After a cycle test time of around 220 days, the cell was stored for 1120 days and another check-up was performed.

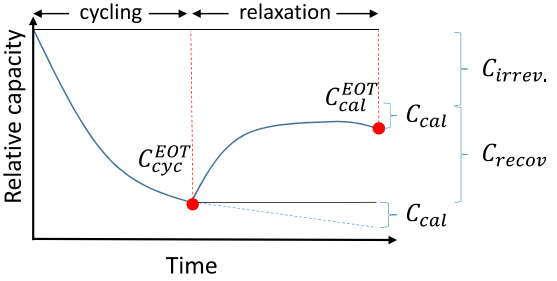

Figure 3.16: Distinction of irreversible and reversible capacity loss during cycling. Recovered capacity is determined with the relaxation phase after cycling [200].

In this storage period, the capacity recovered from 80 % to 90 % of the initial capacity. In addition, the shape and peak heights of the DVA could be restored. To further investigate this phenomenon, Lewerenz et al. [200] measured the capacity in succession to a cycling test at defined SOCs. Multiple reversible effects could be found, on the one hand, depending on the average SOC during cycling and subsequent storage time, a significant recovery of the capacity was observed as seen in Figure 3.16.

Similarly, Ebding et al. found a substantial recovery of capacities after rest periods with high current rates [201]. The current rates chosen for the experiment were above the plating threshold, and plating at 10 °C was experienced. With rest periods and the linked homogenisation, significant cycle-life improvements could be achieved. To evaluate ageing experiments for long-term trends, these effects must be recognised and addressed for accurate results.

3.5 Sample size for ageing experiments

In this chapter, a hierarchical Bayesian approach is used on comparably large datasets to determine the minimal sample size to estimate the underlying distribution.

For statistical power, a study on cell-to-cell variability ideally needs data from a very large number of cells, perhaps thousands. The costs of such large-scale testing would be prohibitive, requiring many battery test channels for multiple years, and no such datasets are openly available. However, as a compromise, some ageing datasets with order 10-100 cells used identically, or very similarly, are available and were used for this study.

Here five datasets are selected for use based on the requirement of wanting over 20 cells per dataset. Two of these are open-source; three are from inhouse experiments. Each individual dataset used identical commercially available Li-ion cells, albeit having different manufacturers, chemistries and cell sizes from dataset to dataset. All datasets used 18650 cylindrical cells, although the methods discussed below can equally be applied to other form factors. Some of the datasets featured identical experimental conditions, i.e, each cell was tested in exactly the same way, whereas others varied the testing conditions slightly beyond the expected uncontrollable experimental variability. The datasets are as follows:

1. Baumhöfer-2014 [86] consists of 48 Sanyo/Panasonic UR18650E NMC/graphite 1.85 Ah cells in a cycle ageing test, each under the same operating conditions.
2. Dechent-2020 consists of 22 Samsung INR18650-35E NCA/graphite cells, each with a nominal capacity of 3.4 Ah. The cells were cycled with a C/2 constant current and a 20 % cycle depth around an average SOC of 50 %.
3. Dechent-2017 consists of 21 Samsung NR18650-15L1 1.5 Ah NMC/graphite cells. Six of the cells were cycled with 1C charge, 6C discharge current between 3.3 V and 4.1 V (90 % cycle depth), and 15 additional cells were cycled with the same voltage range, but current rates varied by up to 15 %.
4. Severson-2019 [202], an openly available dataset, consists of 124 cells made by A123 APR18650M1A with LFP/graphite chemistry, each with a nominal capacity of 1.1 Ah. 67 of these cells with similar load profiles but slightly varying charging current were chosen as a subset for this work. The cells in this dataset re from three different experimental batches so will have been subjected to higher variance in testing conditions than the other datasets.
5. Attia-2020 [203], another openly available dataset, replicates Severson-2019, but with a fixed charging window of 10 minutes. There are 45 cells in this set.

Three of these datasets, namely Baumhöfer-2014, Severson-2019 and Attia-2020, exhibit an onset of rapid degradation in later life, sometimes called the ‘knee-point’ [86], [204]. The other two datasets show only linear degradation over usage. The behaviour before the knee-point in the Attia-2020 and Severson-2019 sets was separately extracted to produce two additional linear ageing datasets.
To accomplish the aim to investigate intrinsic rather than extrinsic variability, simple empirical curve fits of health versus time are chosen as the modelling

approach. It is examined that the consistency of the resulting model parameters as data is added drawn from increasing numbers of cells within each dataset.

Table 3.1: The dataset and empirical model combinations used.

Dataset	Linear-1	Linear-2	LinExp	Ref
Baumhöfer-2014			X	[86]
Dechent-2020	X	X		
Dechent-2017	X	X		
Severson-2019	X	X	X	[202]
Attia-2020	X	X	X	[203]

The models and the corresponding datasets that they were fitted to are shown in Table 3.1. Here, Linear-1 and Linear-2 refer to the two linear models, having one and two parameters respectively. Alternatively, LinExp is a combined linear and exponential model that was used to capture the knee-point and later life health decay, where this was evident in the data.

The three models are given by the following expressions, where t is time, B is capacity, and all other parameters $(c_1, c_2, c_3, B_0, t_f, \tau)$ were fitted to the data:

Linear-1 $(B(t) = 100\,\% + c_1 \times t)$ and Linear-2 $(B(t) = B_0 + c_2 \times t)$ differ only by the addition of the initial capacity B_0 as a fitted parameter in the latter. The cell capacities were normalised according to which model was in use. For Linear-1 and LinExp, the capacities were normalised relative to the initial capacity of each cell. Linear-2 used capacity curves normalised relative to the nominal capacity. In the LinExp $(B(t) = 100\,\% + c_3 \times t - \exp\left[\frac{t-t_f}{\tau}\right])$ model, the initial linear capacity decrease is followed by a faster exponential decrease with onset time t_f and time constant τ, as shown in Figure 3.17.

To quantify cell-to-cell variability, an approach called multi-level Bayes (MLB) was used, also known as hierarchical Bayes, where the parameters of an individual cell model are assumed to be drawn from a population distribution.

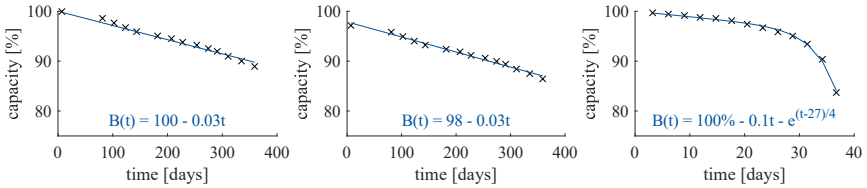

Figure 3.17: Examples of data and fitted curves. Left to right: Linear-1 model on a cell from Dechent-2020; Linear-2 model on a cell from Dechent-2020; LinExp model on a cell from Severson-2019.

In this framework, the first level of inference is on the parameters of an individual battery cell model, and the second level of inference is on the parameters of the underlying population distribution [205]–[207]. Given some data sub-sampled from the datasets described above, this approach provides an estimate of the individual (θ_k) and the population (μ_g, Σ_g) parameter values as well as their associated uncertainties, as depicted in Figure 3.18 a).

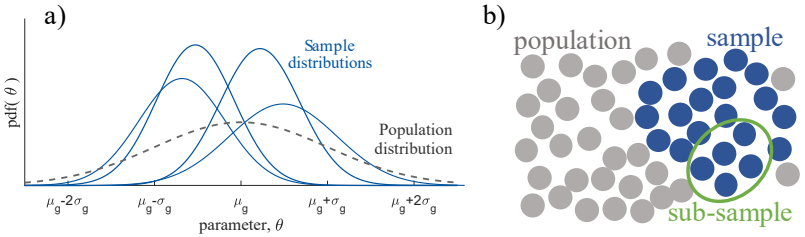

Figure 3.18: Hierarchical approach to infer population statistics. a) The relationship between population distribution and distributions of individual cells/samples. b) A sub-sample is part of a sample, which is part of a population.

Therefore, one can explore the trade-off between the number of cells' data used for fitting the models versus the stability and variance (or standard deviation) of the resulting population parameter estimates. As additional data from more cells is included in the estimation, the variance of the population mean and variance decreases (i.e., certainty of the population model increases). As illustrated in Figure 3.19 the population estimates are considered to be stable when the standard deviation of the population standard deviation estimate began to steadily decrease as a function of sub-sample size $\sim 1/N$. The condition of an acceptable variability

is set as being within a threshold, α, of the stable decreasing region. The value of α was set at 10 % as shown by the grey shaded region in Figure 3.19.
The following conventions are used throughout the remainder of this chapter. Figure 3.18 b) shows the definitions of population, sample and subsample used. The 'population' means the very large (but unavailable) group of all possible similar batteries produced in the same manufacturing batch, from which a subset was tested in a lab. (Therefore, the population statistics is expected to be different for each dataset that was introduced in the previous section.) A 'sample' refers to all the available full data in a specific dataset. Therefore, a sample is drawn from a population. Conversely, any time a smaller subset was drawn from a full test dataset, it is referred to here as a 'sub-sample'. Summary sample statistics are denoted with the Latin alphabet, while population estimates are written using the Greek alphabet. For example, mean and variance are (m, s^2) and (μ, σ^2) respectively. The letter k is used to denote value(s) for a specific cell, and K denotes the total number of cells. Probabilities and distributions are written in capitals: P, N. Battery capacities are represented by the letter B.

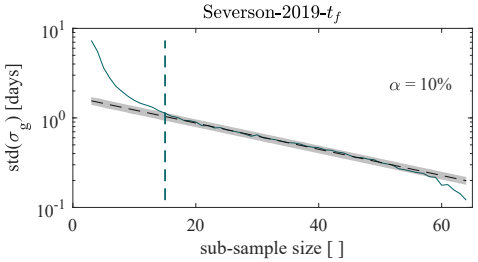

Figure 3.19: Decreasing standard deviation of the population standard deviation estimate as the number of sub-samples used for model fitting is increased. A threshold for an acceptable estimate is shown (vertical dashed line). Example taken from the t_f parameter for Severson-2019.

The Multi-Level Bayes approach is described in more detail in [208]. As a reminder, the objective is to quantify the number of battery cells that are required for a stable fit of a population model, when cells are selected at random from a population. In particular, it is wished to infer both the parameters of the capacity fade model for each cell, and the parameters of the underlying population, including their uncertainties. Now both aspects are examined in succession across the various datasets and models.

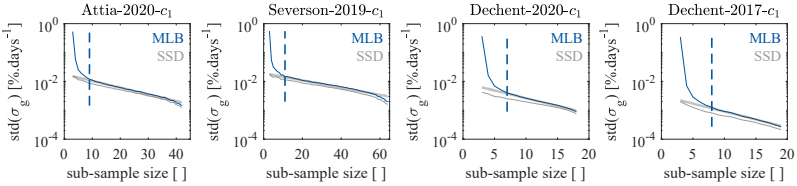

Figure 3.20: Smooth standard deviations are estimated by taking 1,000 random subsamples (with replacement), shown here with the Linear-1 model. MLB is Multi-Level-Bayes, SSD is sub-sample distribution, over the number of cells in the sub-sample.

The summary results from 1,000 repeats, with replacement, were much smoother. The estimated standard deviation of σ_g for the Linear-1 models rapidly dropped with increasing numbers of cells in a sub-sample for all datasets as shown in Figure 3.20. The SSD approach produced a lower variance at all sub-sample sizes, but appears insensitive to small sub-samples.

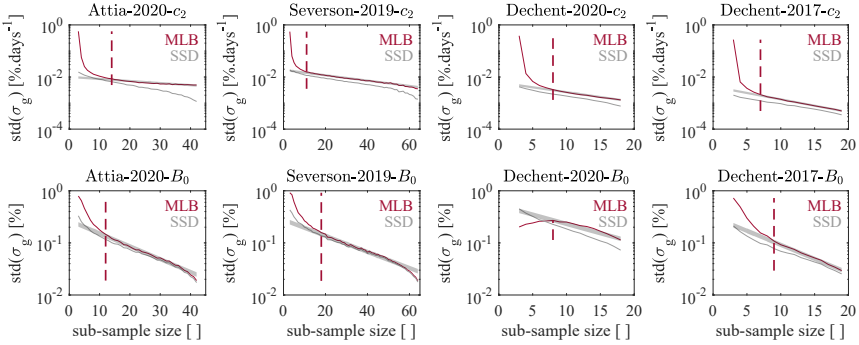

Figure 3.21: The standard deviations of the population-level standard deviation estimates for the Linear-2 model. MLB and SSD results over the number of cells in the sub-sample.

The results for Linear-2 and LinExp were very similar as shown in Figure 3.21 and Figure 3.22, although there were distinctly less stable fits for Dechent-2020-B_0 and Attia-2020-τ. All three models shared a reduced standard deviation of σ_g when using SSD.

The linear relationship between sub-sample size and the log of the standard deviations was deemed to represent a consistent fit. It was subsequently used to determine when an ‘effective’ sub-sample size had been reached. A model was considered well fit when the standard deviation of σ_g was within $\alpha = 10\,\%$ of this stable section, found using a linear extrapolation (as plotted in the figures).

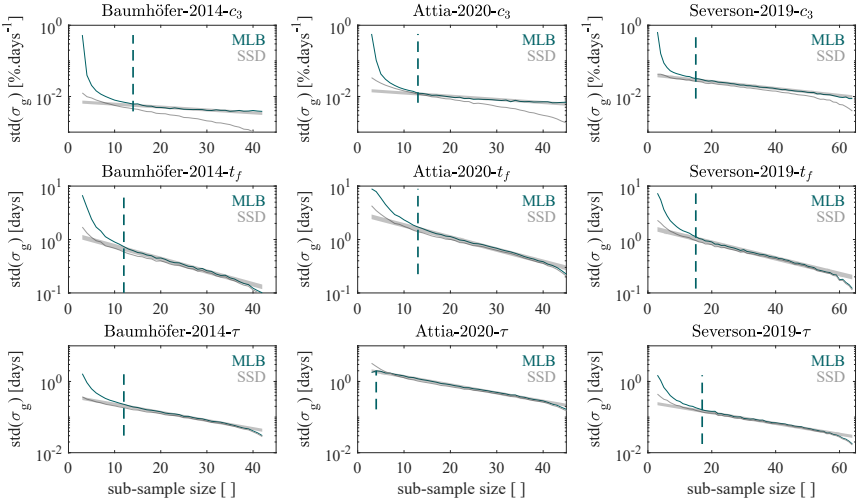

Figure 3.22: The standard deviations of the population-level standard deviation estimates for the LinExp model. MLB and SSD results over the number of cells in the sub-sample.

Figure 3.23 shows the relationship between the number of cells required to achieve 'stable' population estimates vs. the number of model parameters. The number is shown for all model, dataset and parameter combinations. The mean required sub-sample sizes for a consistent fit were 9, 11 and 13 for the 1, 2 and 3 parameter models, respectively.

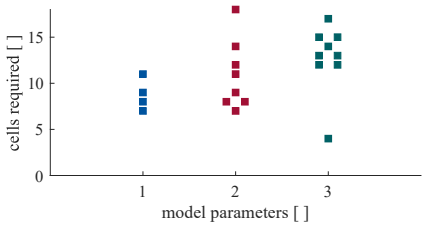

Figure 3.23: Testing with order 10 cells is required to achieve stable population estimates, with the number increasing as the model complexity increases. (Offset x-axis values were used to show identical results.)

The number of cells required to fit the various models presented here and capture a stable estimate of the population variability is of order 10. For the simplest model, Linear-1, the number was 9 cells, and for the most complex LinExp model,

the number increases to 13. The results understandably suggest that increased model complexity leads to an increase in the number of cells required to be tested to achieve a stable estimate of the population variability.

The multi-level Bayesian approach produced consistent parameter estimates from sub-samples. Given that cell-to-cell variability is an important phenomenon impacting battery performance, the estimated distributions are an invaluable tool to use in empirical modelling. Simple sample distribution techniques are limited to estimates of spread within the domain of the sample and hence showed less sensitivity to sub-sample size here when using random selection. The number of cells required to estimate population variability was fairly consistent across the datasets investigated here and was a stronger function of the model complexity than of the dataset. However, future work could test the robustness of this conclusion across a wider range of datasets.

The standard deviation of σ_g estimates reduced as sub-sample sizes were increased. In most cases, the SSD and MLB results also approached the same values as sub-sample sizes increased because the two techniques will return similar results at high sub-sample sizes. At low sub-sample sizes SSD was limited to the variability of the sub-sample, whereas MLB was less certain, resulting in higher values for both σ_g and its standard deviation. In this case, SSD appears to have been artificially confident as an estimate of the population distribution.

The chosen threshold condition for a well fit σ_g parameter resulted in consistent results. The same consistency was also found when using other threshold values of α. The hypothesis that sub-sample size increases with model complexity appears to be supported. However, it would be useful to explore this in more depth using larger datasets.

In the derivation of the MLB approach, it is assumed that there are correlations between parameters in the prior probability distributions. That assumption was found to be questionable in two cases here. Future work should explore the impact of this on population modelling.

The results for the Dechent-2020 dataset with the Linear-2 model demonstrated the robustness of the MLB approach by fitting a very similar gradient to the Linear-1 version, despite an apparently uncertain value of B_0. The estimate of μ_g for B_0 was 99.7 %, i.e., the resultant population model was very similar to that with Linear-1. Our current approach assumes a Gaussian distribution at the population level. In the case of a bi-modal (or multi-modal) population

distribution, it is expected that the MLB method would respond by estimating a wide standard deviation, but this has not been tested. Extending the method proposed in this work to other population distributions would be an interesting subject for future study.

Various ageing mechanisms are likely responsible for the degradation datasets considered in this work. In the case of the Severson dataset, it is likely that degradation was largely caused by lithium plating [202], while on the Dechent-2020 dataset covering layer formation and jellyroll deformation are key to degradation [98].

The fact that more complex models required more cells to be tested at each test point is challenging for battery lifetime experiments, since it could increase greatly the number of test channels and cells required in long term ageing experiments. Even without extrapolating to higher numbers of parameters or to other models, it is reasonable to assume that the issues explored here will be present in other, more complex cases.

One challenge with the technique used here is that it relied on limited size samples from the population. Future work could explore whether larger sample sizes lead to similar results as found here.

The number of cells required to give a stable population variance estimate was found to vary according to the number of parameters in a given model. Respectively, 9, 11 and 13 cells are estimated to be required for models with 1, 2 and 3 parameters. Both sample statistics and population estimates were shown to stabilise with under 20 cells in most cases, but this relied on the existing of a Gaussian distribution of parameters within the sample, otherwise 20 cells were required.

For capacity curve fitting, perhaps the biggest challenge going forward is the selection of appropriate ageing model order and structure. This should be done not just by looking at what functions fit the capacity profiles best but which functions produce the most reliable parameter distributions when looking at a dataset as a whole.

There was insufficient data here to test these results and conclusions as a function of variability caused by differences in usage, but this would be an interesting future exploration topic. Also, model selection across larger datasets is a challenging problem. For example, some of the battery capacity fade trajectories in this study fitted well to a linear degradation stage followed by an exponential decay starting from some knee-point. However, some of the resultant sample

distributions cannot be confidently used to calculate basic summary statistics, such as Dechent-2020-B_0.

3.6 Chapter Conclusion

Within the literature review it has been established what are the key aspects of cell-to-cell variation. The origins of cell-to-cell variations and inhomogeneities on a multiscale level are covered, their impact on electrochemical performance, and their characterisation and tracking methods, ranging from the use of large-scale equipment to in-operando studies. Finally, the review summarises the state-of-the-art understanding and characterisation of cell-to-cell variations and inhomogeneities observed upon ageing.

In addition, this chapter establishes the minimum number of cells, which should be tested to accurately represent population variability since testing many cells is expensive. Derived from various degradation datasets, including new measurements performed as part of this work, empirical capacity-versus-time ageing models were fitted. While assuming that the model parameters could be drawn from a distribution describing a larger population, then, using a hierarchical Bayesian approach, the number of cells required to be tested was estimated. Depending on the complexity, ageing models with 1, 2 or 3 parameters respectively required data from at least 9, 11 or 13 cells for a consistent fit. This implies researchers will need to test at least these numbers of cells at each test point in their experiment to capture manufacturing variability.

4 Evaluation of ageing tests

After establishing the origin of inhomogeneities and cell-to-cell variation in Chapter 3, in this chapter the results of an automated evaluation of ageing tests is shown and lithium-ion batteries compared on energy, power, lifetime and operating temperature. After this step back and the thorough evaluation of cycle and calendar data the raw data is accessible in a comparable and uniform database. This is the foundation to further look into the data and identify cell-to-cell variation within.
Parts of this chapter are published in a journal article [209] as part of this thesis with equal contribution by the author and Alexander Epp.

4.1 Foundation of comparisons

Due to their impressive energy density, power density, lifetime, and cost, lithium-ion batteries have become the most important electrochemical storage system, with applications including consumer electronics, electric vehicles, and stationary energy storage [210]. However, each application has unique, often conflicting product requirements, requiring a balanced overall assessment. The Ragone plot [211], shown in Figure 4.1 a) for lithium-ion battery chemistries, is a commonly-used plot to compare two of these specifications, energy and power; however, important parameters including cost, lifetime, and temperature sensitivity are not considered.
A standardised and balanced reporting and visualisation of specifications would greatly help an informed cell selection process. Comparisons of energy and power density can be made relatively easily via standard test protocols and within a short timeframe. However, comparing cells across other dimensions presents some practical challenges, particularly in an academic setting. First, even though the price is an essential criterion in many applications, it is also the most controversial since individual cell prices are not openly shared and depend on nontechnical factors such as production volume and operating margin. Second, lifetime comparisons of lithium-ion batteries are widely discussed in the literature [212]–[217], but these comparisons are especially challenging due to the high sensitivity of lithium-ion battery lifetime to usage conditions (e.g., fast charge, temperature control, cell interconnection, etc.). Additionally, the metrics for lifetime are not standardised, and conclusions about lifetime performance are generally

dependent on the choice of metrics used (e.g., relative vs absolute capacity or energy; see Figure 4.1 b)-c).

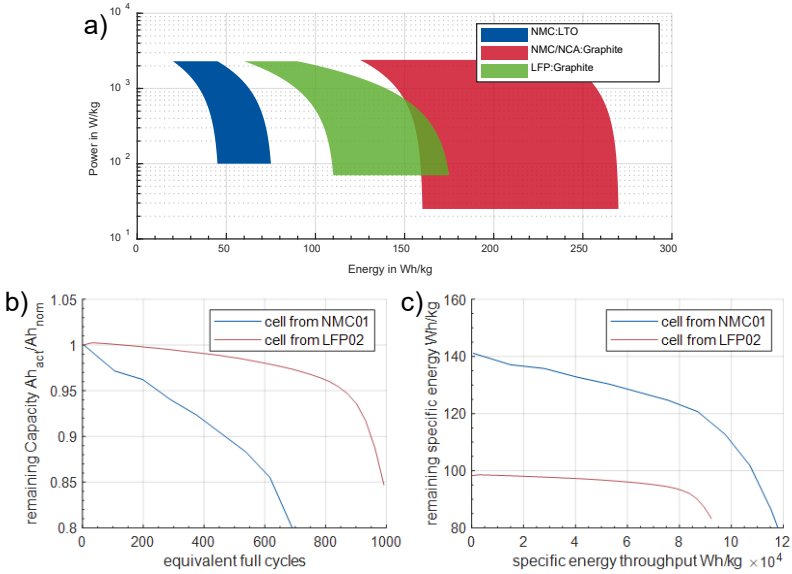

Figure 4.1: Limitation of existing comparisons a) Ragone plot b) shows relative capacity vs. equivalent full cycles, c) shows remaining specific energy vs. specific energy throughput.

Furthermore, battery degradation is often nonlinear [202], [217], [218]; therefore, using a single parameter from a linear fit (e.g., the slope) to represent nonlinear ageing trends must be handled with care. Despite these challenges, standardised reporting and visualisation of these parameters are still helpful for fundamental understanding and practical concerns such as cell selection. To this end, bubble plots have been used on the material level to compare lithium metal electrodes on four dimensions [219].

In this chapter, ENPOLITE (**en**ergy-**po**wer-**li**fetime-**te**mperature) plots are introduced to compare cells across various chemistries, designs, and usage conditions, as seen in Figure 4.2. ENPOLITE plots represent multidimensional bubble plots derived from a non-logarithmic version of the Ragone diagram [211]. Leveraging the increasing number of open-source battery datasets, ENPOLITE compares over 1000 battery cells within a single bubble plot derived from a raw

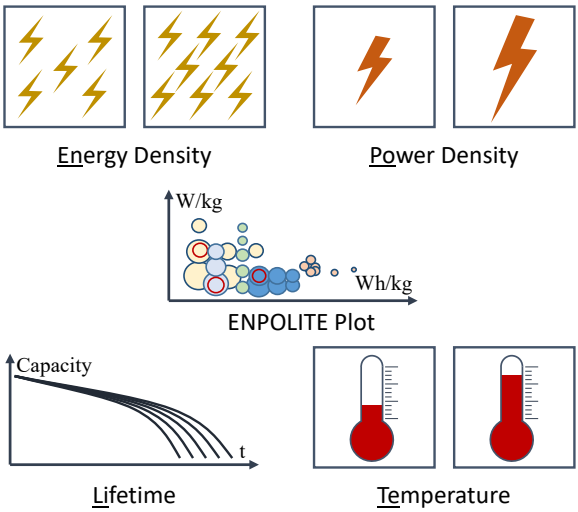

Figure 4.2: ENPOLITE plots illustrate **en**ergy **po**wer **li**fetime and **te**mperature characteristics of lithium-ion cells.

data set exceeding 1000 GB. Over 10000 check-up procedures with multiple data points are evaluated. While this plot makes some simplifications to represent the multidimensional dataset, it can be effectively used for cell comparison and selection. ENPOLITE plots of ageing-related parameters illustrate differences between lifetimes. Although various age-specific variables and metadata are contained in each set of ageing data, composed of a dataset of cells, the ENPOLITE plots present a simple two-dimensional graph, allowing easy comparison of individual battery cell types. A public website (enpolite.org) was also created that hosts interactive versions of these plots.
For this chapter, datasets were named according to the following table:

Origin of data	Identifier	Raw data/ External	#	Brief description: Cell name, nominal capacity, format	Ageing -Type	Test-duration	Ref, Year
e-production	NMC01	Raw data	48	Sanyo UR18650E, 1.85 Ah, 18650	Cyc.	~170d	[220], 2014
	NMC02	Raw data	24	Sanyo UF121285, 5 Ah, prismatic	Cyc.	~480d	
GOELK	NMC03	Raw data	13	LiTec 40 Ah, pouch	Cyc.	~550d	[221], 2019
	NMC04	Raw data	30	LiTec 40 Ah, pouch	Cal.	~650d	[221], 2019
FutureBus	LTO01	Raw data	23	Microvast 10 Ah, pouch	Cyc.	~230d	[222], 2019
e-performance	NMC05	Raw data	65	Sanyo UR18650E, 2.05 Ah, 18650	Cyc.	~410d	[223], 2014
	NMC06	Raw data	48	Sanyo UR18650E, 2.05 Ah, 18650	Cal.	~450d	[224], 2014
HV-Modal	LTO02	Raw data	10	Toshiba SCiB 2.9 Ah, prismatic	Cyc.	~630d	[225], [226], 2020
	LTO03	Raw data	16	Toshiba SCiB 2.9 Ah, prismatic	Cal.	~590d	[225], [226], 2020
MobilEM	NCA01	Raw data	183	Samsung INR18650-35E, 3.4 Ah, 18650	Cyc.	~240d	[98], 2020
	NCA02	Raw data	60	Samsung INR18650-35E, 3.4 Ah, 18650	Cal.	~450d	
LiMobility	NMC07	Raw data	27	440-Kokam, 40 Ah, pouch	Cyc.	~300d	[227], 2015
HiEnd	LFP01	Raw data	26	OMLIFE8AHC-HP, 8 Ah, cylindrical	Cyc.	~260d	[228], 2016
DriveBattery	NMC08	Raw data	39	Samsung INR18650-15L, 1.5 Ah, 18650	Cyc.	~250d	[229], 2017
	NMC09	Raw data	27	Hitachi 5 Ah, prismatic	Cyc.	~580d	[229], 2017
Severson et al.	LFP02	Raw data	124	A123 APR18650M1A, 1.1 Ah, 18650	Cyc.	-	[202], 2019
Attia et al.	LFP03	Raw data	45	A123 APR18650M1A, 1.1 Ah, 18650	Cyc.	-	[203],2020
Naumann et al. &	LFP04	External	14	Sony US26650FTC1, 3 Ah, 26650	Cyc.	~900d	[230], [231], 2020
Spingler et al.	LFP05	External	17	Sony US26650FTC1, 3 Ah, 26650	Cal.	~900d	[232], 2020

Harlow et al.	NMC10	External	11	Li-FUN Technology 0.24 Ah, pouch	Cyc.	~860d	[233], 2019
	NMC11	External	24	Li-FUN Technology 0.24 Ah, pouch	Cal.	~580d	[233], 2019
Preger et al.	LFP06	Raw data	28	A123 APR18650M1A, 1.1 Ah, 18650	Cyc.	~640d	[217], 2020
	NCA03	Raw data	22	Panasonic NCR18650B, 3.2 Ah, 18650	Cyc.	~170d	[217], 2020
	NMC12	Raw data	24	LG Chem 18650HG2, 3 Ah, 18650	Cyc.	~220d	[217], 2020
Schmitt et al.	NMC13	External	8	Sony US18650V3, 2.15 Ah, 18650	Cal.	~470d	[234], 2017
Schimpe et al.	LFP07	External	10	Sony US26650FTC1, 3 Ah, 26650	Cal.	~230d	[235], 2018
Keil et al.	NMC14	External	32	Sanyo UR18650E, 2.05 Ah, 18650	Cal.	~310d	[236], 2016
	LFP08	External	32	A12318650M1A, 1.1 Ah, 18650	Cal.	~280d	[236], 2016
	NCA04	External	32	Panasonic NCR18650PD, 2.8 Ah, 18650	Cal.	~290d	[237], 2016
Devie et al.	NMC15	Raw data	15	LG Chem ICR18650C2, 2.8 Ah, 18650	Cyc.	~670d	[238], 2018

4.2 Cyclic ENPOLITE plot

In contrast to the Ragone plot, the ENPOLITE plots do not show the power and energy capabilities of a cell but the energy and power density at the respective lifetime's operating condition. Therefore, the same cell type is shown at different energy and power levels when cycling currents or cycle depths are different. The x-axis represents the used specific energy density of the individual battery cell at the beginning of life (BOL) within its ageing test and is calculated using Equation 1. In this work, the calculations are based on battery cell weight, which is less controversial yet equally important in many technical applications.

$$(1)\quad \frac{\Delta \boldsymbol{DOD} \cdot \boldsymbol{C}_{\mathbf{Cell(BOL)}} \cdot \overline{\boldsymbol{U}}_{\mathbf{Cycle}}}{\boldsymbol{m}_{\mathbf{Cell}}} \left[\frac{\mathbf{Wh_{Cycle}}}{\mathbf{kg}}\right]$$

Here, $\mathbf{\Delta DOD}$ represents the cycling depth, $\mathbf{C_{Cell(BOL)}}$ the discharge capacity, $\overline{\mathbf{U}}_{\mathbf{Cycle}}$ the mean voltage while cycling, and $\mathbf{m_{Cell}}$ the cell mass. Thus, the x-axis represents the average amount of energy a cell has charged and discharged per kg

and per cycle in the completed ageing test and describes the battery cell-specific operating point. Although the capacity changes with the cell lifetime, its position is not updated within the ENPOLITE plot. If the raw data is available, the cycling depth is calculated; if not, the cycling depth is taken from the publication.
It should be noted that cells used with different cycle depths may have the same used specific energy. A cell with an energy density of 200 Wh/kg with a cycle depth of 50 % and a cell with 125 Wh/kg and a cycle depth of 80 % have an equal used specific energy of 100 Wh/kg.
The y-axis represents the specific power of the individual battery cells during cycling and is calculated using Equation 2:

$$(2)\quad \frac{\overline{I}_{\mathbf{Charge}} \cdot \overline{U}_{\mathbf{Cycle}}}{m_{\mathbf{Cell}}} \left[\frac{\mathbf{W_{Charge}}}{\mathbf{kg}}\right]$$

Here, $\overline{I}_{\mathbf{Charge}}$ represents the mean charge current, $\overline{\mathbf{U}}_{\mathbf{Cycle}}$ the mean cycling voltage, and $\mathbf{m_{Cell}}$ the cell mass. A typical Ragone plot depicts the dischargeable power, which can be used to determine the capability of a cell to fulfil an application requirement. Since charge currents generally have a more significant influence on ageing than discharge currents[214], [239], [240], the y-axis shows the power used while charging. Similar to the x-axis, the y-axis in the ENPOLITE plots is normalised to the cell weights. It should be noted that cells with different used C-Rates may have the same used specific power. This can be caused by differences in cell chemistry and the average cycle voltage. A cycle ENPOLITE plot relative to the cell volume can be found in Figure 4.10 at the end of this chapter.
The achieved lifetime of the individual cells is also portrayed in the ENPOLITE plots. The comparison of lifetime data requires a measure of ageing that normalises cell weight or volume and reflects the cell's realistic usability. It is expressed in the graphic as the bubble area. In this work, the used lifetime coefficient is a linear ageing model, expressed in energy throughput per percentage point of cell capacity lost, normalised to the respective cell weight. While the linear model is a simplified description of cell degradation, unable to follow nonlinear ageing patterns accurately, it allows a comparison with only one value. Other more complex ageing models could be part of further Big-Data lithium-ion ageing analysis that can be executed with the datasets used in this work.
The lifetime coefficient (and therefore the area of the bubble) is calculated using Equation 3:

$$(3)\quad \frac{\boldsymbol{N_{\mathrm{FCE(EOT|EOL)}} \cdot C_{\mathrm{Cell(BOL)}} \cdot \bar{U}_{\mathrm{Cycle}}}}{\boldsymbol{m_{\mathrm{Cell}} \cdot \%_{\mathrm{Cap.Loss(EOT|EOL)}}}} \left[\frac{\mathbf{Wh_{Throughput}}}{\mathbf{kg \cdot \%_{Cap.Loss}}}\right]$$

Here, $N_{\mathrm{FCE(EOT|EOL)}}$ represents the equivalent full cycles to reach the end-of-life-criterion (EOL) or the end of the test (EOT), $\mathbf{C_{Cell(BOL)}}$ the discharge capacity, $\bar{\mathbf{U}}_{\mathbf{Cycle}}$ the mean cycling voltage, $\mathbf{m_{Cell}}$ the cell mass, and $\%_{\mathrm{Cap.Loss(EOT|EOL)}}$ the capacity percentage points lost. If raw data is available, the charge throughput is extracted directly. A doubling of the circle area is equivalent to a doubling of the lifetime coefficient.

In line with published literature, the lifetime linearisation was normalised to a relative capacity loss of 20 %. If cells did not lose 20 % of their initial capacity within their ageing tests, the linearisation was based on their EOT. Generally, different EOL criteria can also be used. Unlike most published lifetime comparisons, the lifetime coefficient calculated here also considers cell size and compares battery cells using the mass-normalised energy throughput. Thus, different cell masses, charge throughputs, and cycling voltages, driven by different mean DODs and different cell chemistries, can be considered.

Depending on the data availability, either the actual raw data is used to calculate the charge throughput or the throughput is estimated by multiplying the achieved equivalent full cycles and the cell rated capacity at the beginning of its ageing test. The average cycle voltage is multiplied, and the overall coefficient is normalized to the cell mass and percentage point of capacity loss. Therefore, the formula above gives a fundamental approach to calculate the normalized energy throughput for sparse data availability.

For the figures given in this chapter, the degradation is fitted to a linear ageing model to an EOL of 80 % relative capacity. For this, the first available capacity measurement beneath the 80 % relative capacity mark was used. The latest available data point was used for cells that did not reach 80 % relative capacity, and the capacity degradation was linearized upon that data point. The graphics given in the work can be made with other EOL criteria lying above or beyond the 80 % mark.

Besides a simple linear approximation of the ageing curves, different approaches like a logarithmic or partial linear fitting, which was used for calendar ageing, were considered. However, other models did overall not lead to a more accurate

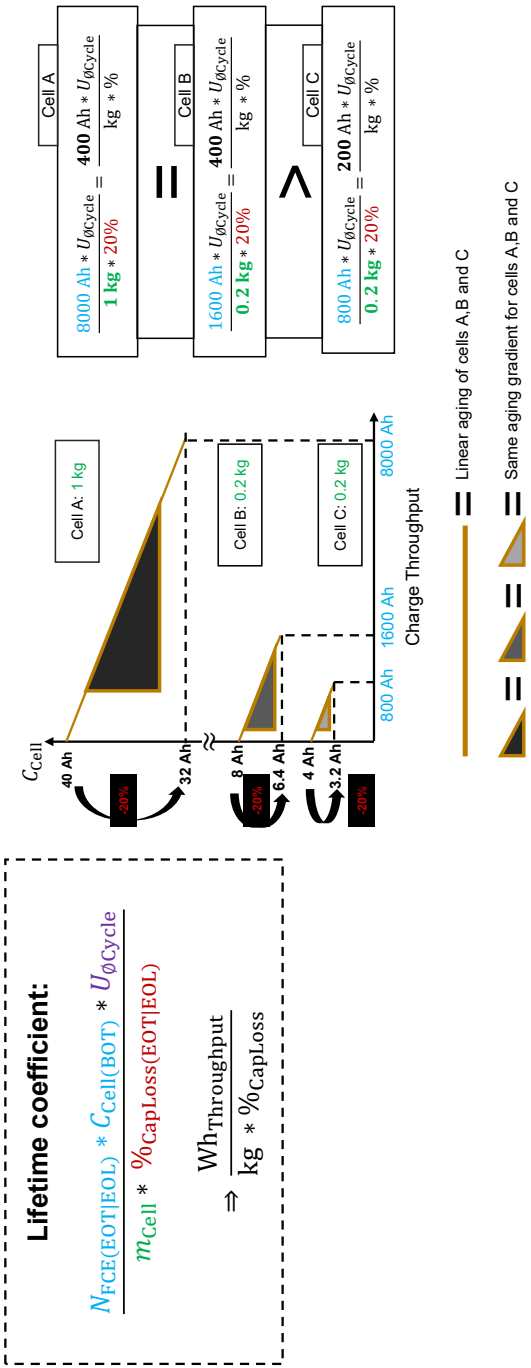

Figure 4.3: Cyclical lifetime coefficient calculation and comparison.

approximation for all datasets. Besides, these models have multiple parameters, which cannot be put in the one-dimensional circle area.

Figure 4.3 illustrates the advantages of the lifetime coefficient compared to a typical ageing plot. For simplicity, capacity instead of energy was used. It compares three theoretical cells with different weights and energy densities, illustrating which cells have the same lifetime coefficient. Cell A has five times the weight but the same energy density as Cell B; both degrade the same when normalized to weight. Cell C is the same weight and has the same ageing gradient as Cell B, but the lifetime coefficient is lower with a lower energy density.

Finally, the cell-specific cycling temperature also plays a decisive role in explaining the ageing behaviour of lithium-ion cells. The colour of each bubble circumference depicts the cell temperature during cycling, providing vital information to explain differences in individual cell lifetimes at similar operation points. If available, the mean cycling temperature at the can or pouch of the cell is used. If the individual cell temperature is not available, the temperature chamber setpoint was used. It should be noted that the temperature within a cell and the temperature chamber can vary significantly, especially for high power cycling. For cells without extractable cycling temperature, the bubble circumference is grey.

With the values for the x- and y-axis and the lifetime bubble area established, all cyclic ageing datasets can be sorted into the ENPOLITE plot. Figure 4.4 shows the translation of an initial ageing test result to the ENPOLITE plot for a cell from a data set with 2.9 Ah LTO cells. The relevant metadata for the lifetime coefficient calculations is given in the lower-left corner. The green area shows the calculation for the x-axis; the red area shows the calculation for the y-axis; the blue colour shows the calculation for the lifetime coefficient and is reflected in the bubble area within the graphic. A higher lifetime coefficient and more normalised energy throughput are reflected in a larger bubble area.

In addition to the metadata (cell chemistry, nominal capacity, cell format, cycling time) of the individual datasets, Figure 4.5 depicts an ENPOLITE plot of one complete data set of 10 cells. The colour of the bubble circumference, which corresponds to the temperature, explains the differences in the lifetime coefficient for cells with similar electric operating points. Not surprisingly, cells cycled at higher temperatures (i.e., red-coloured bubble edges) are found to also have shorter lifetimes (i.e., bubble sizes).

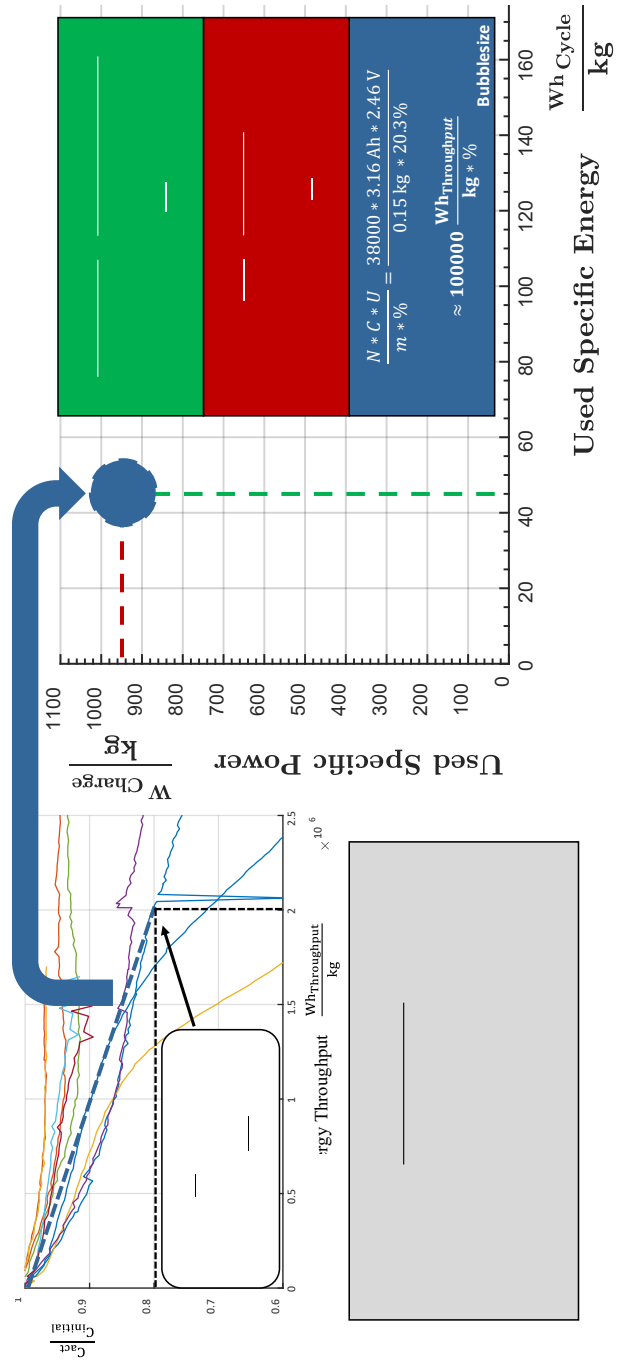

Figure 4.4: Calculation of a single bubble data point for the ENPOLITE plot.

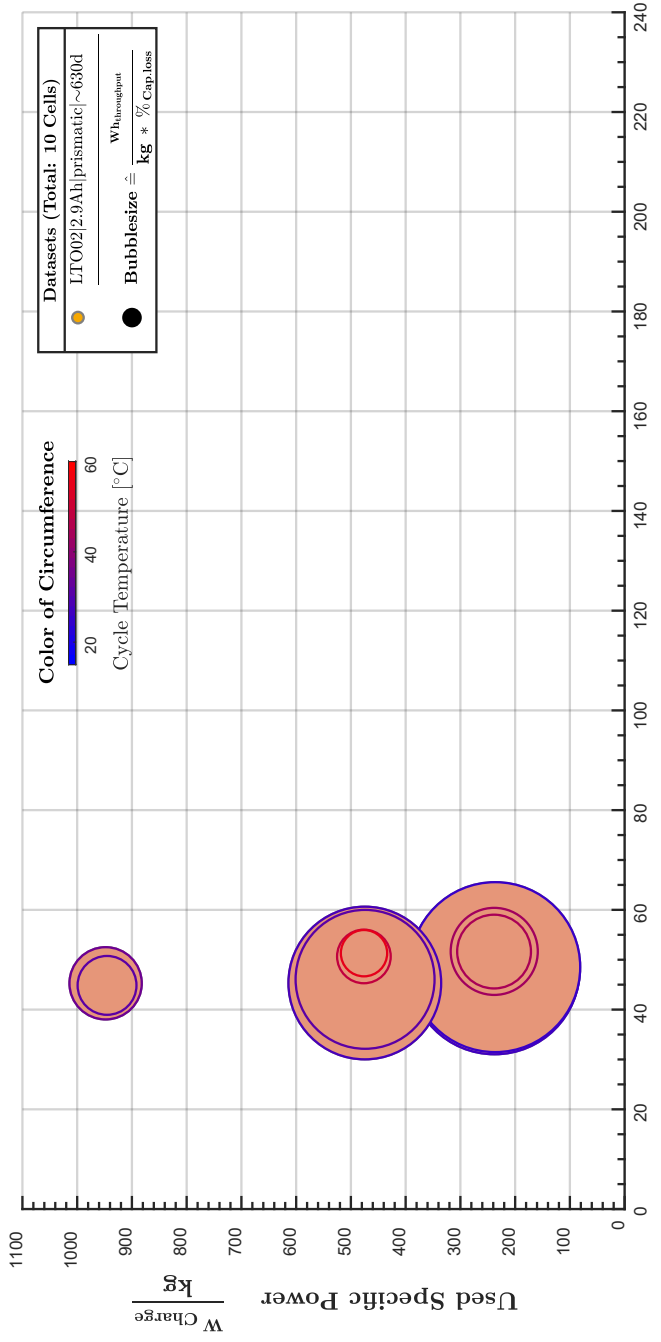

Figure 4.5: : Dataset LTO02 with 10 cells illustrated in the

Figure 4.6 shows the complete ENPOLITE plot for the cyclic ageing tests of 783 different cells from 19 datasets shown in detail in Table 1. An interactive version and detailed description can be found in the Supporting Information and on the website (enpolite.org). In total, the ENPOLITE plot in Figure 4.6 displays eight critical parameters determining the lifetime behaviour of lithium-ion battery cells: i) used energy density, ii) used power density, and iii) energy throughput per percentage point, as well as the metadata on the ageing test including iv) cycle temperature, v) cycle duration, vi) cell chemistry, vii) cell format, and viii) nominal capacity. The plot reflects the general trend that lifetimes tend to decrease with higher energy densities and power densities. The dark-yellow-coloured dataset with cells from Devie et al. [238] (NMC15|2.8Ah|18650|~670d.) shows the highest used specific energy with up to 230 Wh/kg. The high energy cells from LG Chem were cycled at 100 % DOD. Only a few cells achieved above-average lifetimes at either high energy or high power densities, such as the dark-blue-coloured dataset (NMC10|0.24Ah|pouch|~860d.) from Harlow et al. [233]. Furthermore, it was also observed that high power densities were only achieved in conjunction with lower energy densities. In most datasets, higher cycling temperatures resulted in a reduced lifetime, corroborating the well-known behaviour of lithium-ion battery cells. This can also be seen for the above mentioned NMC10 cells at 165 Wh/kg and 50 W/kg, for which the circle area significantly decreases for cells cycled at higher temperatures within the same operating point. Occasionally, tiny data points are also visible, representing cells quickly destroyed at their operating point in the ageing test, for example, due to lithium plating at low temperatures. The exceptionally high lifetimes of cells with Lithium Titanate (LTO) anodes are also well represented; the peach-coloured dataset (LTO02|2.9Ah|prismatic|~630d.) of Nemeth and Schröer et al. [225], [226] stands out with the highest lifetime observed of any cells in this plot. Furthermore, these cells also achieve the highest used specific power with up to 950 W/kg, corresponding to current rates of up to 20C. Lastly, neighbouring data points with a similar circumference colour but strongly differing circle areas illustrate cell-to-cell ageing variation within a dataset, with an in-depth evaluation in upcoming work.

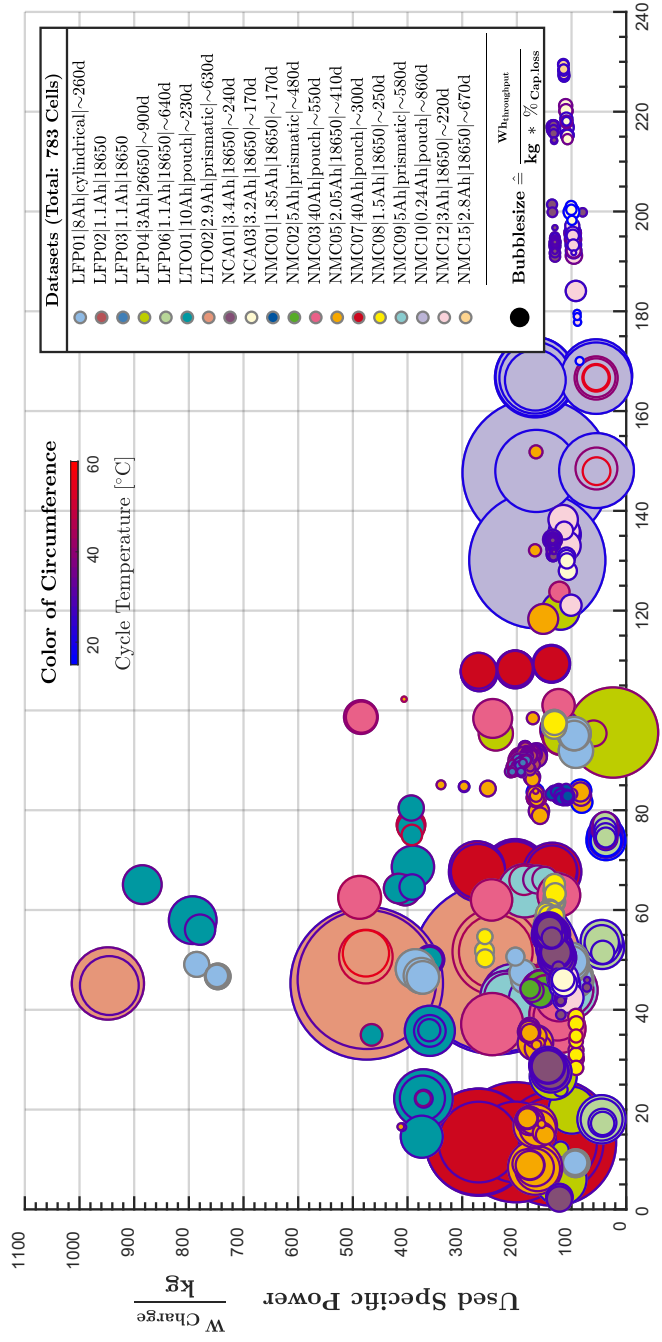

Figure 4.6: Cyclic ENPOLITE lifetime plot representing 783 battery cells. An interactive version can be found online at enpolite.org.

4.3 Calendar ENPOLITE Plot

An ENPOLITE plot depicting calendar life was created using a similar approach. The X-axis for the calendar ENPOLITE plot depicts the state of charge (SOC) of the cells in storage, expressed as the usable stored energy in the cell normalized to its weight. The used specific storage energy coefficient was calculated using Equation 4:

$$(4)\quad \frac{\boldsymbol{C_{\mathrm{Cell(BOL)}}} \cdot \boldsymbol{U_{\mathrm{nom}}} \cdot \boldsymbol{SOC_{\mathrm{Storage}}}}{\boldsymbol{m_{\mathrm{Cell}}}} \left[\frac{\mathbf{Wh_{SOC}}}{\mathbf{kg}}\right]$$

Here, $\mathbf{C_{Cell(BOL)}}$ represents the discharge capacity at the beginning of life, $\boldsymbol{U_{nom}}$ the nominal voltage, $\boldsymbol{SOC_{Storage}}$ the state of charge, and $\mathbf{m_{Cell}}$ the cell mass.

The X-axis indicates how much energy per kg was stored by the cell at the beginning of life (BOL), and the Y-axis coefficient represents the cell storage temperature in degrees Celsius (°C).

This X-axis describes the stored energy during the ageing normalized to the weight of the cell. Ideally the integrated mean storage voltage is used to determine the energy contained in the cell during storage, but due to data availability, $\boldsymbol{U_{nom}}$ was used instead. Most of the datasets used in the calendar ENPOLITE Plot are from extracted ageing diagrams where often just the storage SOC is given. The used approximation for the stored specific energy considers differences in cell chemistry and the respective storage SOC and could be evaluated for sets with incomplete data. Cells with a storage SOC of 0 % are mapped at 0 $\frac{\mathrm{Wh_{SOC}}}{\mathrm{kg}}$ in the calendar ENPOLITE Plot. A calendar ENPOLITE plot relative to the cell volume can be found in Figure 4.11 at the end of this chapter.

Figure 4.9 depicts a calendar ENPOLITE diagram, representing 307 calendar-aged cells in total. In this plot, the typical calendar ageing test matrices are readily recognised. Most cells are stored at temperatures of 25°C, 40 °C, or 50 °C. Each cell type is typically stored at multiple SOC levels; therefore, multiple points of the used specific storage energy are shown.

Similar to the cyclic ENPOLITE plot, an ageing measure was developed for the calendar ageing data, which better reflects the battery cells' actual usability than the relative loss of capacity metric often used in literature. The passive anode effect [196], [241], commonly seen in calendar tests, was included in the evaluation and described in detail in the Supporting Information. The ageing

coefficient's bubble area corresponds to the number of days until the cell energy density is reduced by 1 Wh/kg due to degrading capacity.
The lifetime coefficient was calculated using Equation 5:

$$(5)\quad \frac{\boldsymbol{Date_{T2} - Date_{T1}}}{\dfrac{(\boldsymbol{C_{T1} - C_{T2}}) \cdot \boldsymbol{U_{nom}}}{\boldsymbol{m_{Cell}}}} \left[\frac{\mathbf{Days}}{\frac{\mathbf{Wh_{Lost}}}{\mathbf{kg}}}\right]$$

Here, $\boldsymbol{Date_{T2} - Date_{T1}}$ represents the time difference between measurements, $\boldsymbol{C_{T1}}$ and $\boldsymbol{C_{T2}}$ the first and second capacity measurements, $(C_{T1} - C_{T2})$ the capacity lost between measurements, $\boldsymbol{U_{nom}}$ the nominal voltage, and $\mathbf{m_{Cell}}$ the cell mass.
The structure and input of each data point with respect to the X- and Y-axis and the size of the circle area, represented by the ageing coefficient, are similar to the cyclic diagram structure shown in Figure 4.6. For the representation of the calendar lifetime data, however, some striking differences have to be considered. Particularly in calendar ageing tests, cells sometimes retain over 100 % of their initial capacity even after a long ageing period. Examples of this can be found in dataset NMC11 from Harlow et al. [233]. It can be seen that individual cells still increase in capacity even up to the last capacity measurement published after 580 days. However, an increase in capacity in the linear part of the ageing process leads to a negative value by definition of the used lifetime coefficient according to the formula above. For this reason, the value ∞ was inserted into the calendar ENPOLITE plot. This value does not imply that the cells last forever but is used when the lifetime coefficient cannot be evaluated because the corresponding cell capacities are still rising. The size of these bubbles is fixed and does not represent an absolute lifetime; they should not be compared with other datapoint sizes. Cell data with this exception are illustrated with transparent shading in the calendar ENPOLITE plot and may in fact point to excellent durability.
Figure 4.7 again shows some exemplary cells for calculating the lifetime coefficient illustrating the advantages over regular ageing diagrams. It compares three theoretical cells with different weights and ageing gradients, illustrating which cells have the same lifetime coefficient. Cell A has five times the weight and the same ageing gradient as cell B. But cell B loses more capacity per day, and 5 cells of type B would still only work for 160 days; the lifetime coefficient of cell A is better than B. Cell C is half the weight of cell B and has a slower

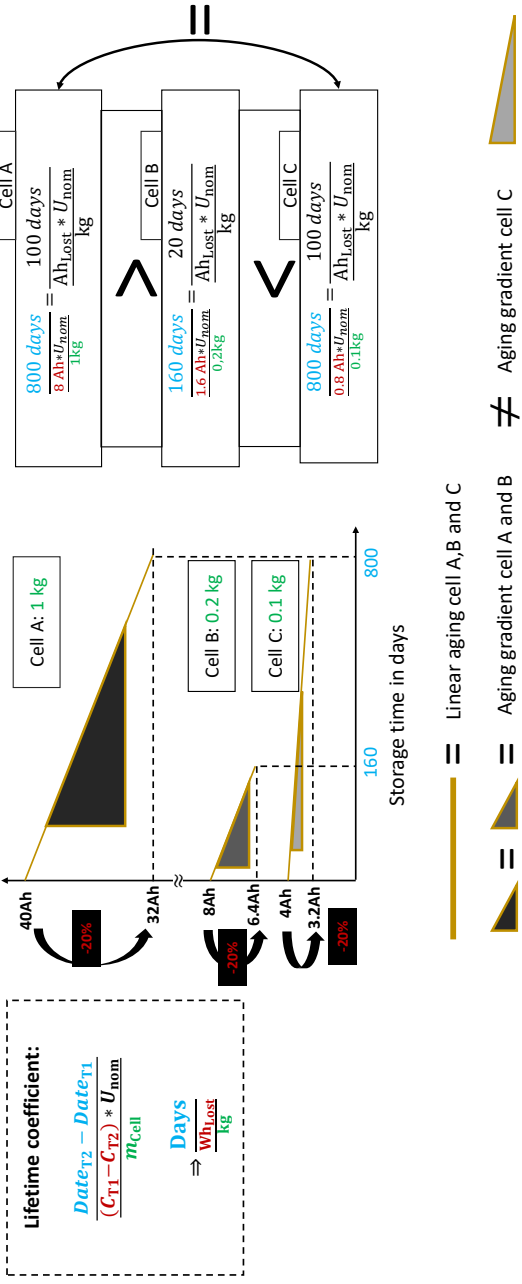

Figure 4.7: Calendar lifetime coefficient calculation and comparison.

ageing gradient. Therefore, it has a better ageing coefficient than B and the same as A. For simplification reasons, the voltage was considered as constant in this scheme. In actual usage, the voltage is another critical parameter in which the cell lifetime rating may be distinguished. In contrast to the lifetime coefficient used for the cyclical ENPOLITE Plot, a different approach was used for the calendar case. A partial linear fitting was used to exclude the common reversible ageing phenomena due to the anode overhang [196]. For this, only the best linear fitting part of the capacity degradation was calculated. Since the duration in which the reversible ageing takes place varies in different circumstances, initially, the first 90 days of the respective ageing test are not used when calculating the lifetime coefficient. Afterwards, various possible linear ageing degradation curves are created with the constraint that at least 50 % of the remaining data points are included in the linear fit. Afterwards, the fit with the highest coefficient of determination is selected.

If the overall data points without the first 90 days of ageing are less than four for a cell, the fit is executed with every remaining data point. Figure 4.8 illustrates an example of this procedure.

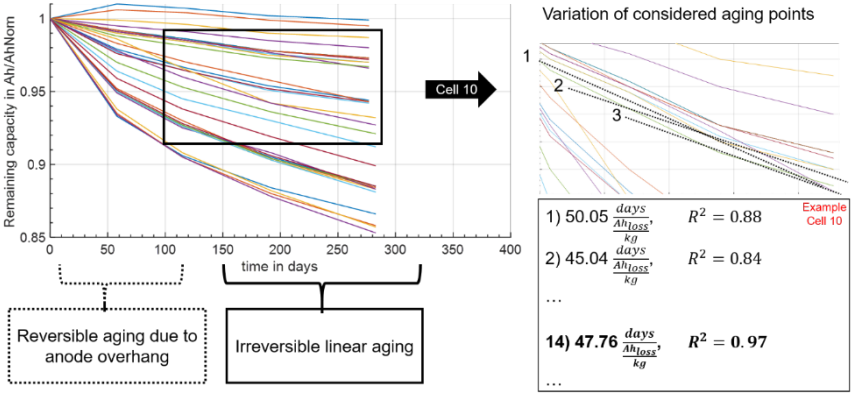

Figure 4.8: Anode overhang effect often visible in calendar ageing tests.

Figure 4.9 shows the ENPOLITE plot of calendar lifetime data for a total of 307 cells from 11 datasets. A reference bubble, equivalent to 100 days to a loss of 1 Wh/kg, can be found in the bottom-right corner of the diagram for better

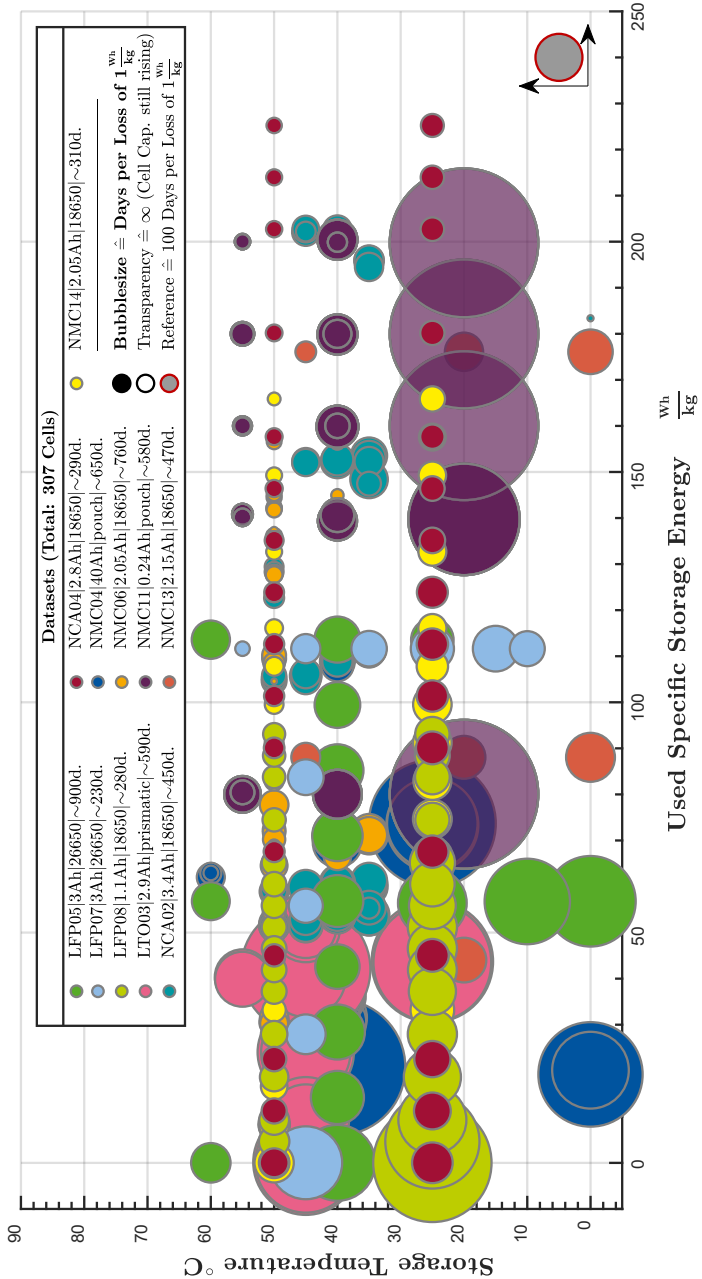

Figure 4.9: Calendar ENPOLITE lifetime plot representing 307 battery cells. An interactive version of the plot can be found online at enpolite.org.

estimation of the bubble area. In this diagram, a doubling of the circle area also doubles the calculated lifetime coefficient.
Generally, Figure 4.9 illustrates that cells stored at higher energy/charge states lose storable energy (and thus capacity) faster than cells stored at low energy/charge states. Used specific storage energies range from 0 Wh/kg (0 % SOC) up to 225 Wh/kg represented by the dark-red-coloured dataset (NCA04|2.8Ah|18650|~290d.) from Keil et al. [237], which were stored at 100 % SOC at 25 °C and 50 °C, respectively. Outstanding lifetimes were achieved by lithium-nickel-manganese-cobalt-oxide (NMC) cells (NMC11|0.24Ah|pouch |~580d.) from Harlow et al. [233], depicted by turquoise dots, even at high used specific storage energies. Especially at 20 °C, they outperformed other cells without visible ageing after 580 days even at high SOC. The authors attributed this to the single-crystal structure of the NMC532 cathode particles and electrolyte additives [233]. The influence of the storage temperatures on the lifetimes is also clearly visible. In general, within all datasets, higher temperatures were associated with shortened lifetime. Few data points were aged below 20 °C and none of these belonged to the datasets showing the longest lifetime. No cells tested above 60 °C were part of the datasets in the calendar ENPOLITE plot, since side reactions prevent valid accelerated ageing tests[242].

4.4 Chapter conclusion

Lithium-ion batteries must satisfy multiple requirements for a given application, including energy density, power density, and lifetime. However, visualizing the trade-offs between these requirements is often challenging; for instance, battery ageing data is presented as a line plot with capacity fade versus cycle count, a difficult format for viewing multiple datasets. Also, standard lifetime plots can be challenging to interpret (e.g., high cycle count with low energy throughput). In this work, the ENPOLITE plots are introduced, which can be used to compare large datasets of lithium-ion battery cycling and calendar ageing across multiple battery chemistries and usage conditions. ENPOLITE plots capture performance metrics that are relevant for applications. Similar comprehensive representations of large datasets of variable battery ageing data were, to the best of our knowledge, never before shown in published literature. ENPOLITE plots (and, more generally, multidimensional plotting) may greatly facilitate informed decisions on battery technology development. Some of the observations were

known before, e.g., that LTO are suitable for high power, or that batteries cannot be both high power and high energy density. This commonplace knowledge is now substantiated by specific values for energy and power application-specific selection. The ENPOLITE plots also reveal exemplary cells across a number of dimensions. As the battery community continues to publish data, particularly on new chemistries, the ENPOLITE plots enable unbiased comparisons of key operating parameters to be added to published battery databases. Finally, it is remarkable that with non-uniform data formats being the biggest hurdle for inclusion of additional datasets, the battery community would greatly benefit from standardized and uniform battery data formats for automated evaluation.

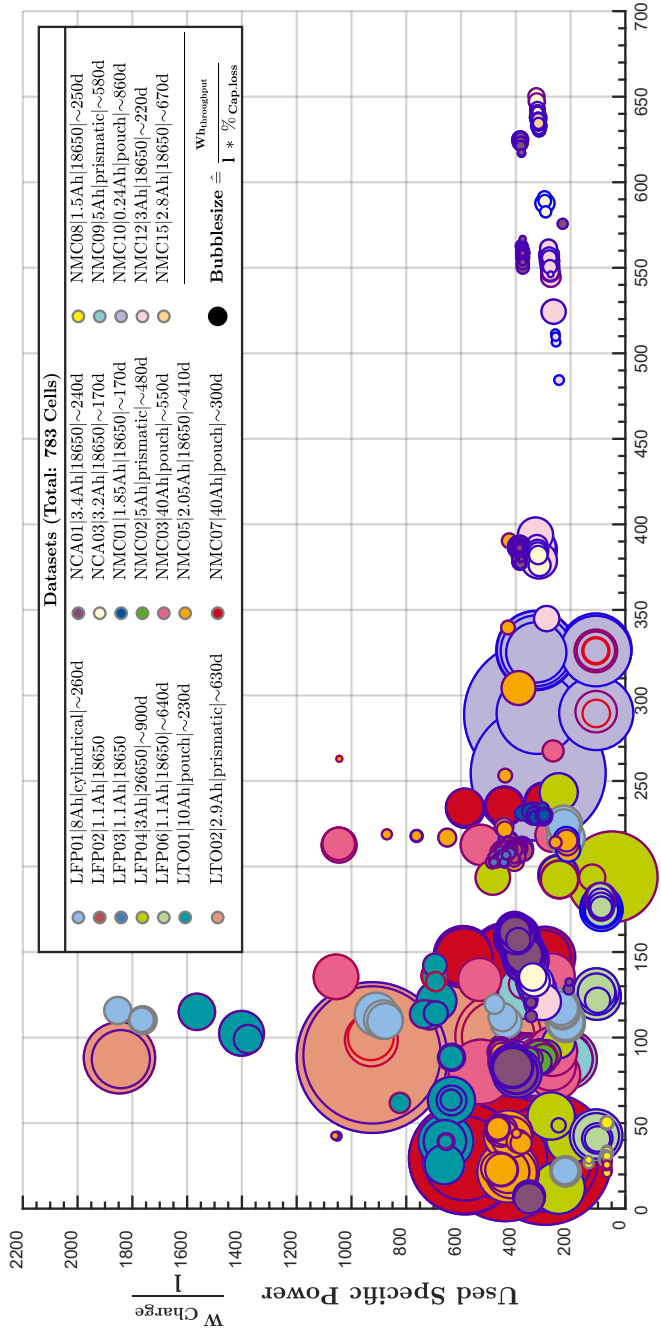

Figure 4.10: Complete volumetric cycle ENPOLITE lifetime plot with 783 cells.

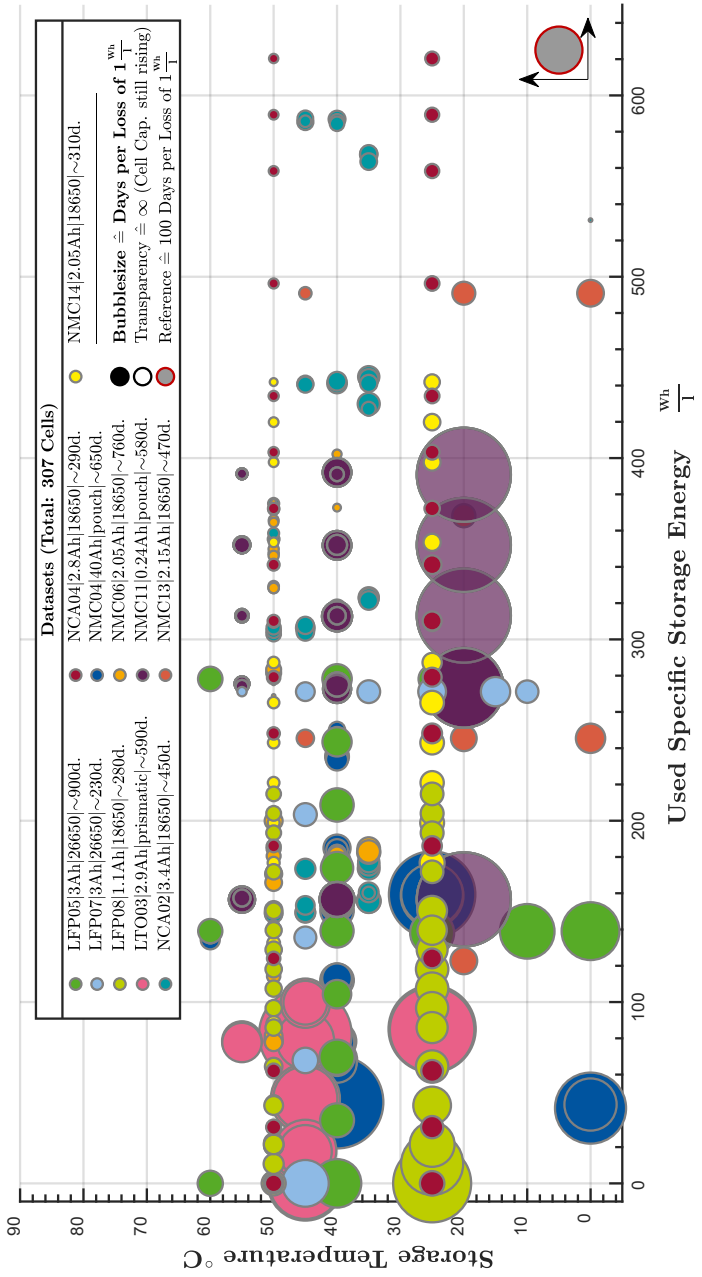

Figure 4.11: Complete volumetric calendar ENPOLITE lifetime plot with 307 cells.

5 Correlation of Health Indicators

To quantify ageing and to describe cell-to-cell variation, different measurements may be used. The most frequently employed indicators are the remaining capacity and the internal resistance. In principle, however, any measure that continuously changes with ageing is suitable as a health indicator. Quantities that can be measured reliably and with little effort are beneficial. With regard to inhomogeneities, the permanent monitoring of each individual cell is quite reasonable, which is only feasible with an extremely simple measurement method or when indicators can be extracted from the load profile. Satellites with positional motors, for example, are only used every other day, so the cells experience a pulse profile and open-circuit voltage (OCV) values that can be easily determined but never the full capacity. EVs, in contrast, are usually fully charged with a constant voltage (CV) phase, and the relaxed voltage after full charge can be tracked. It is also possible to use the frequency response of an application with repeating loads (e.g. every second pulsed load for 50ms) to calculate an impedance for the battery. Furthermore, the significance of the various indicators depends on the application. For example, for high-power applications, the resistance is more critical than the capacity.

While even operating conditions have to be ensured on system-level by, e.g., an even temperature distribution, the other two have to be met on cell level or cell selection process, respectively. First, high-quality cells have to be used, which lead to a minimum spread in cell-to-cell variation throughout the system's lifetime. Secondly, measures must be found during the cell selection process to grade the cells and exclude cells with a possibly diverging behaviour from the good-to-be-used cells.

In automotive applications, system size is currently limited to a comparatively small size below 100 kWh. Yet, as they are mass-produced and cost-saving potential shall be addressed on cell as well as on system-level, direct cell-to-pack architectures such as the BYD blade are considered [243]. This results in a high individual cell capacity. However, as a drawback, no cell-level smoothing behaviour of a parallel connection occurs.

Finally, there are also production-related effects resulting in a diverging ageing behaviour on using unmatched cells. These imbalances can be accounted to manufacturing tolerances and the formation process, as well as varying conditions during shipment and storage. Strictly speaking, the latter is standard calendar

ageing under different conditions. Yet, as it takes place before integration in modules, it has to be considered as an initial deviation in the new state and tracking those variations is necessary.
In this chapter, different health indicators are compared, and their correlations are analysed. Understanding the correlation of health parameters enables a focus on easily recordable parameters to better track ageing trends when high-resolution data is unavailable. Considered health indicators are, among others, impedance measurements of different pulse lengths, capacity values at different discharge procedures and check-ups, weight and initial voltage. The following analysis is based on the data already used in the previous chapters.
A comprehensive overview of the cell parameters of the individual datasets according to the respective datasheets is provided in Table 5.1. As already indicated in the list of datasets, not every analysis is presented for all datasets. Therefore, an overview of investigated health indicators can be found in Table 5.2

Table 5.1: Analysed cells of the individual test sets used in this chapter.

	Baumhöfer-2014	Schöneberger-2019	Willenberg-2021
Manufacturer	Sanyo/Panasonic	LiTec	Samsung
Cell name	UR18650E	HEI40	INR18650-35E
Cell type	18650	pouch	18650
Cathode material	NMC	NMC	NCA
Nominal Capacity/Ah	1.85	40	3.35
Nominal voltage/V	3.6	3.6	3.6
Min. voltage/V	2.5	3	2.65
Max. voltage/V	4.2	4.2	4.2
Max. charge current/A	2.05	80	2
Max. discharge current/A	6.15	120	8
Mass/g	45.5	1200	50

The list gives an overview of the main test set boundaries and states the identifier used later on in order to distinguish between the different test sets:

1. Baumhöfer-2014 [86] consists of 48 Sanyo/Panasonic UR18650E NMC/carbon 1.85 Ah cells in a cycle ageing test each under the same operating conditions. The dataset is used in the analysis of initial cell parameters at delivery.
2. Schöneberger-2019 [221], LiTec HEI40 40 Ah, pouch Automotive large scale pouch cells. The dataset is used in the analysis of calendar and cyclic test conditions.
3. Willenberg-2021 [98], Samsung INR18650-35E, NCA/Graphite cell with a nominal capacity of 3.4Ah cylindrical 18650 type. The dataset is used in the analysis of initial cell parameters at delivery.

5.1 Health indicators

As the primary visual element to analyse the correlation of the health indicators, a multi-plot with an even number of subplots aligned in x- and y-direction, as shown in Figure 5.1, is used and shall be briefly introduced. The health indicators such as, e.g., the first capacity and cell weight are pairwise combined by using each health indicator once as a column identifier and once as a row identifier.

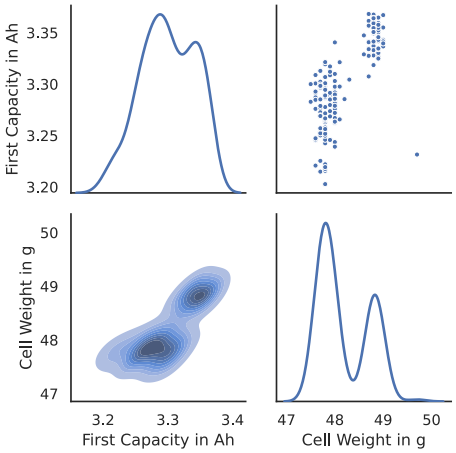

Figure 5.1: Example of the correlation matrix plot used in this chapter. Scatter plots in the upper right corner, KDE plots in the lower left and density plots on the diagonal. The y-axis label does not apply for the density plots.

As the n-th position in row and column has the same identifier, the identity relationship is shown on the diagonal from upper left to lower right. It is depicted as a kernel density estimation (KDE) that smooths a Gaussian kernel's observed values to a continuous density estimation rather than depicting, e.g., the values binned in histograms. The general shape of the KDE allows the identification of the individual distribution function of a parameter visually and by a goodness-of-fit test. The maxima indicate the most likely values.
In the upper triangle, the discrete measurement points are depicted in a scatter plot. By the resulting point cloud, it is likely to identify clusters and linear dependencies. A drawback of scatter plots is that the various points can overlap and thus become invisible. This is valid, especially for large test sets with pronounced data pairs.
The same combination of health indicators is analysed in the lower triangle but with a reversed x- to y-axis allocation. Instead of points within the scatter plot, the bivariate KDE contour plot is drawn with each line indicates the region containing the value pairs resulting in a density above the line's threshold. Hence, significantly pronounced areas of a high density can be identified very easily by the plot and the steepness in the different directions around it.
The health indicators used are described in Table 5.2.

Table 5.2: Description of health indicators

Indicator	Description
First Capacity	Discharge Capacity determined in the first check-up procedure
Second Capacity	Discharge Capacity determined in the second check-up procedure
Weight	Measured cell weight
Initial Voltage	Cell voltage at delivery
1 kHz impedance	1 kHz impedance measured at delivery
Impedance	Cell impedance can be determined using a different pulse current (in C-Rates), duration (in seconds) and observed cell SOC (in %). Example ResCHA1C2sec30

	is a charge pulse resistance with a current of 1C after 2 seconds at a state-of-charge of 30 %
TestTemperature	Temperature of the ageing test (cycle, calendar)
Capacity-CHA-CC	Measured Capacity of constant current phase (CC) until the upper cell voltage level is reached
MeanTemp	The mean cell temperature within the test

5.2 Correlation of initial health

Figure 5.2 shows the capacity at the first and second check-up in Ah, the cell weight in g, the initial voltage before cycling in V, and a 1 kHz impedance in mΩ measured upon arrival from Willenberg-2021. The 18650 cylindrical cells from Samsung SA35E were bought in three batches in March 2018 (in blue), November 2018 (in orange) and November 2019 (in green). Cells from the first batch showed a lower first capacity compared to the latter two. The cells showed a higher impedance while being, on average, around 1 g lighter. Cells within the batches varied below 1 g while in total, the lightest and heaviest cell differed in around 2 g. In the initial voltage at delivery, a batch dependence is also visible. This can be caused by material differences or differences in storage time since this can reduce the charge within the battery through calendar ageing. Similar differences over the production cycle were reported by Schindler et al. [40]. The first capacity ranges between 3.3 and 3.4 Ah, with bigger variances observed than other single datasets, for example, by Kuntz et al. [244] with a mean discharge capacity of 3.328 Ah and a standard deviation of 0.019 Ah. This can be attributed to a slightly higher current of 0.3C or on batch dependence with similar differences over the production cycle reported by Schindler et al. [40]. Kuntz et al. also observed tighter tolerances within the cell weight with a standard variation of only 40 mg. The 1kHz impedance varied within the dataset from around 20 to 24 mΩ, with a strong batch dependence. This resistance is highly temperature-sensitive, so it needs to be accounted for when checking at delivery, and cells need to adjust to the same temperature.

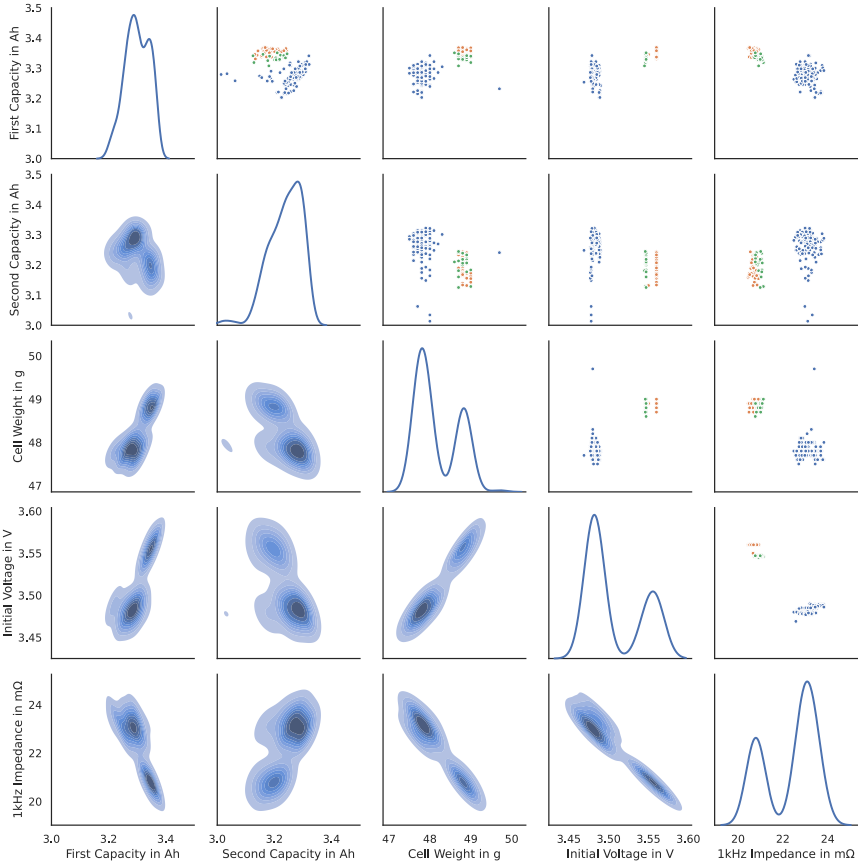

Figure 5.2: Correlation of the following initial parameters of dataset Samsung 35E: First Capacity, Second Capacity, cell weight, initial voltage and 1 kHz impedance. Capacities are determined within the check-up procedure; weight, voltage and impedance are recorded at delivery. Cells were bought in 3 batches, batch 1 in blue, 2 in orange and 3 in green.

Figure 5.3 depicts the initial parameters for the Baumhöfer-2014 set. Here displayed are the capacity at the first and second check-up in Ah, the capacity during the constant current charging phase in Ah, the mean temperature in Celsius during the check-up, and two discharge pulse resistance values at 1C and 50 % state-of-charge at 2 and 10 seconds. For this evaluation, the 1C capacity is used, so they are slightly varying from the values depicted in the capacity vs cycles plots in Baumhöfer et al. [86]. The first discharge capacity shows values between 1.76 and 1.79 Ah increasing to a spread of 1.70 to 1.75 Ah in the second check-up. A correlation is visible between the first and second check-up with higher first capacities also trending to higher second capacities. But some of the lowest values of the second capacity show comparably high first capacity values. So, the first capacity captures the general trend, but higher ageing rates cannot be captured, resulting in differences in the second capacity. The capacity from the constant current charge shows no clear trend compared to the first or second capacity. A small temperature dependence can be seen between test temperature and resistance, with higher resistances leading in general to lower resistance values, as is expected. The mean temperature of the whole check-up ranges from 26.5 °C to 28.5 °C, and the other values do not show an influence of temperature in the depicted range.

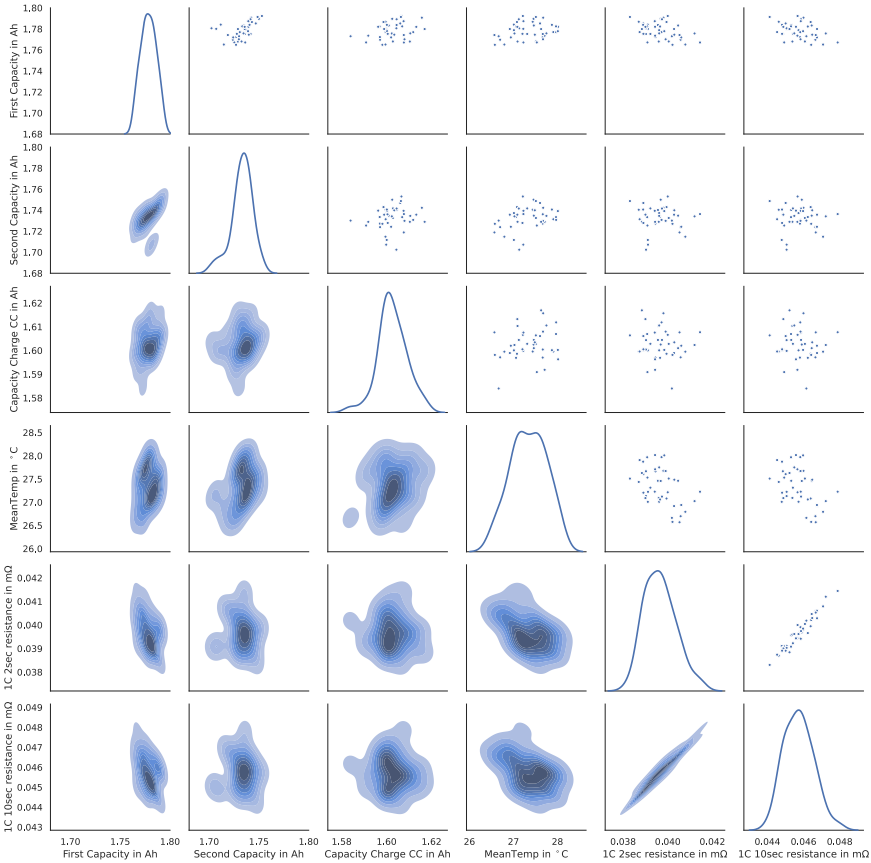

Figure 5.3: Correlation of the following initial parameters of dataset Baumhöfer-2014: First Capacity, Second Capacity value, Charge capacity during the constant current phase, Mean Temperature during the check-up and 2-sec and 10-sec pulse resistances at 1C, 50 %SOC. All values are determined within the check-up procedure.

5.3 Correlation of pulse resistance measurements

To illustrate the content of Figure 5.6, first, a subset of the values is depicted in Figure 5.4. Here three different pulse resistance values are shown, and all values over the whole lifetime of all cells correlated. The correlation coefficient for each pairing is given in the lower-left half as part of the scatter plots. In the next step, Figure 5.5 shows the same correlation but as a heat map. Each resistance is shown once on the x-axis and on the y-axis, and the correlation coefficient for each pairing is given as a colour code at the intersection and a legend at the side.

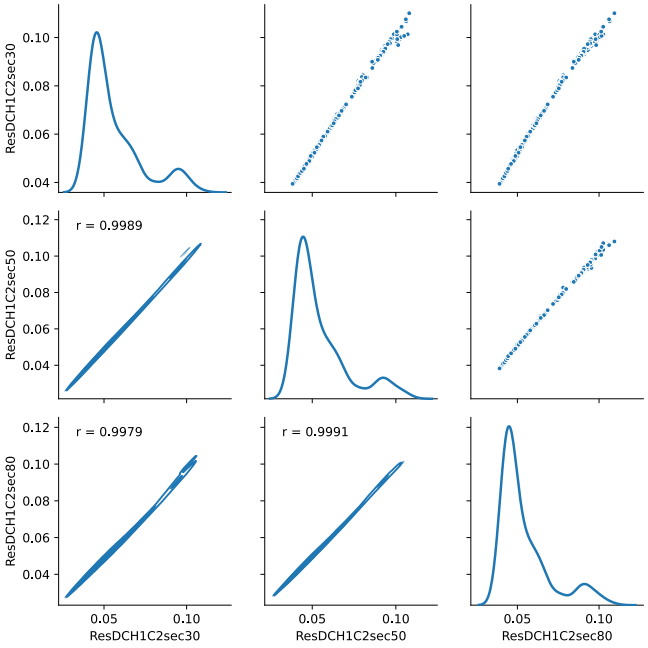

Figure 5.4: Scatterplot of 3 pulse resistance values at SOCs of 30, 50 and 80% of dataset Baumhöfer-2014 over all check-ups with the addition of the correlation coefficient of each pairing.

A bright value depicts a good correlation between two pulse resistances, a dark value shows poor or no correlation. The correlation includes values from each check-up over the whole lifetime of all cells of the Baumhöfer-2014 data set. The labels are named in the following way: Res is short for resistance, CHA for charge pulse and DCH for discharge pulse, next to the current as a C-rate, a leading zero indicates a fraction, so 025 indicates 0.25C, afterwards the pulse length either 2

or 10 seconds and last the state-of-charge in percent. Concluding ResCHA1C2sec30 is a charge pulse resistance with a current of 1C after 2 seconds at a state-of-charge of 30 %.

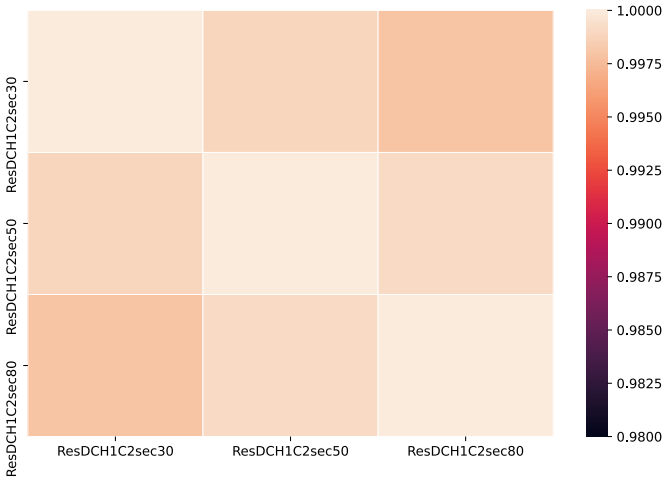

Figure 5.5: Heatmap of the same 3 pulse resistances as in Figure 5.4 at SOCs of 30, 50 and 80% of dataset Baumhöfer-2014 over all check-ups with the correlation coefficient as the colour of the heatmap.

As shown in Figure 5.6 overall, the correlation of pulse resistances within this dataset is very high, with the lowest values still above 0.98. Pulse length, in this case, an evaluation after 2 and 10 seconds, correlates more than 0.995 in all operating conditions expect the charge pulse resistance at 80% SOC. At an aged condition, charge pulses will approach the upper cell voltage limit faster. Nevertheless, the correlation is still around 0.99, and it can be assumed that differences in pulse length are minimal and, therefore, slightly different pulse lengths, for example, 2 and 10 seconds, can be used to compare ageing trends on multiple datasets. For significant timescale differences, for example, as part of the impedance spectroscopy, low correlations were observed between the timescales [245], limiting comparisons to the same order of magnitude.

The highest and lowest current rates do not correlate as well. One explanation is that the voltage response for low current rates is also smaller, leading to a lower signal-to-noise ratio. In addition, high currents excite different chemical and physical processes, which can develop differently over the lifetime.

The state-of-charge levels compared in this dataset set at 30 %, 50 % and 80 % highly correlate. To analyse the ageing trend while limiting the time of a check-up procedure, one of these charge levels would give similar conclusions to 3 charge levels. But it can also be sensible for a more detailed analysis to include other SOCs since resistance also has a SOC dependence, especially at low and high SOCs [184].

In addition to pulse resistances at a defined state-of-charges, other resistances can be calculated without any additional measurements. Each current, either charge or discharge, generates a voltage change to determine a resistance value. For example, the first 10 seconds of a discharge can be handled as a pulse. Or, as Rumberg et al. [246] suggest, the resistance can be calculated after a discharge, with the last cell voltage during discharge and the voltage the cell relaxes to.

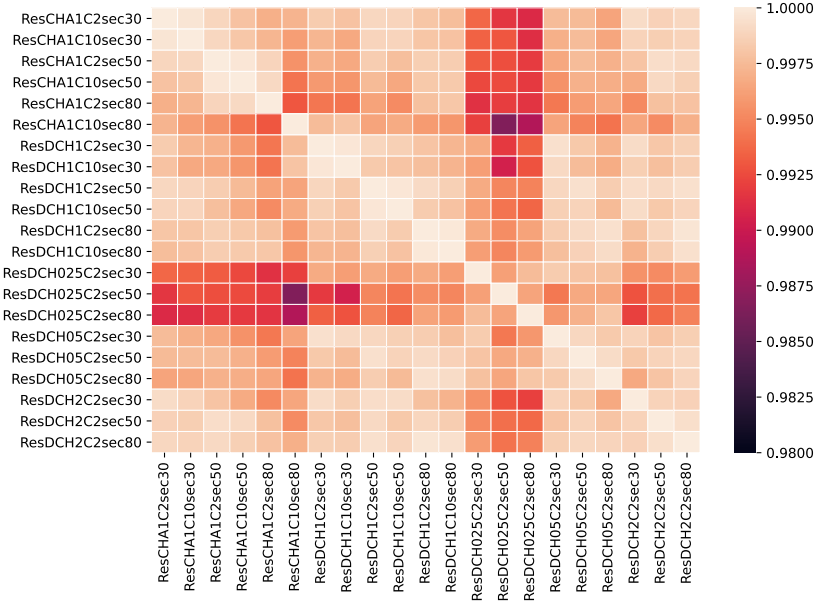

Figure 5.6: Heatmap of correlation of different pulse resistances from Baumhöfer-2014 dataset. The colour of the heatmap shows the correlation coefficient of each pairing in the matrix.

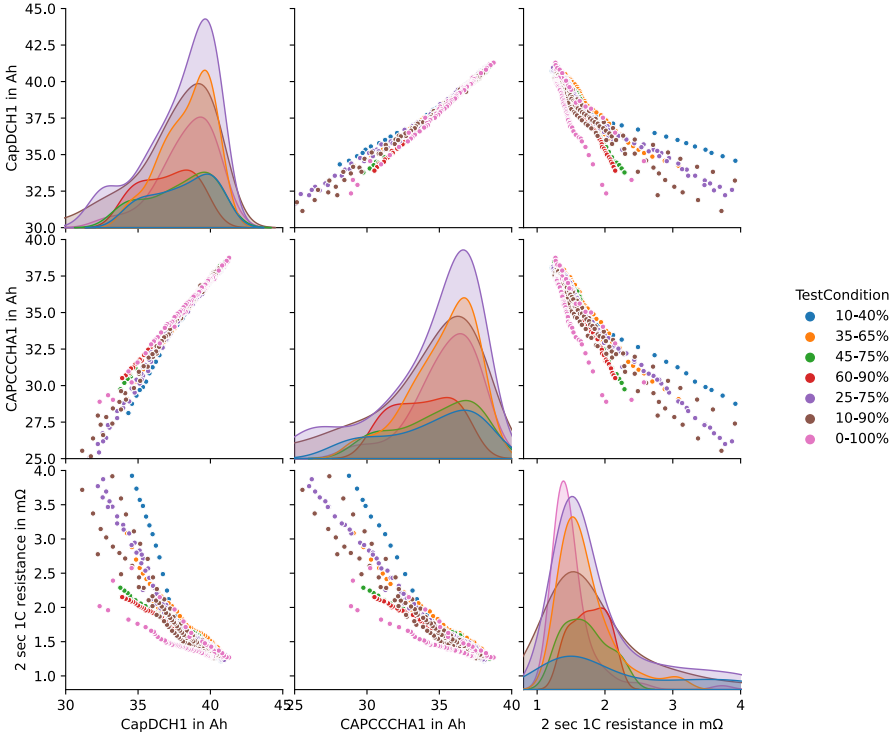

Figure 5.7: Correlation of discharge capacity, charge capacity and pulse resistance over cycle ageing for dataset Schönberger-2019. Colour represents different test conditions of cycle test with lower and upper SOC during cycling shown in the legend.

Figure 5.7 shows the influence of different test conditions on the correlation of health indicators. For these 3 values, the discharge CapDCH1 capacity, the Ah throughput during constant current charge CAPCCCHA1 and one pulse resistance value were used. The test conditions all used a current of 1C but were cycled with different cycle depth and mean state-of-charge and with one cell each. The upper and lower SOC during cycling is shown in the legend. While the discharge and charge capacity show a strong correlation, slight differences are already visible for the different test conditions. When substituting health indicators for ones that are easy to measure, the relation must be independent of the history of prior cycling. This, unfortunately, cannot be observed, showing different resistance to capacity relations depending on the cycling condition. For higher cycling depths, capacity degrades quicker compared to the resistances in this data set. Discharge and charge capacity show a high correlation and can likely be substituted for an ageing analysis if one is not available. This is not the case for the resistance capacity correlation with clear differences visible for the different test conditions. For example, cycling from 0-100% shows the highest capacity degradation in relation to the resistance measured. At around 35 Ah remaining discharge capacity, the pulse resistance is still below 2 mΩ, while cells from other test conditions already show a pulse resistance of up to 4 mΩ. When the ageing condition triggers different ageing regimes, the correlation will not be the same for those conditions. Similar results for different ageing conditions but less pronounced are reported by Schuster et al. [247].

Not only for cycle tests but calendar aged cells with a path dependency of the correlation are shown in Figure 5.8. Three cells were tested for each test condition and aged at 40 °C, except for one test at 25 °C and one at 60 °C, both at 66 % SOC. At 40 °C, 8 different SOCs were tested, ranging from 10-100 %. Just as the cycle aged cell 3 values, the discharge CapDCH1 capacity, the Ah trough put during constant current charge CAPCCCHA1 and one pulse resistance value were used in the comparison. Similar to cycle ageing, both capacity values strongly correlate with the 60 °C cells standing out, showing generally lower constant current charge capacities at similar discharge capacity levels. For cells at 60 °C, a disproportional increase of resistance can be seen. The highest SOC levels, 90 % and 100 %, also have higher capacity loss relative to the resistance increase.

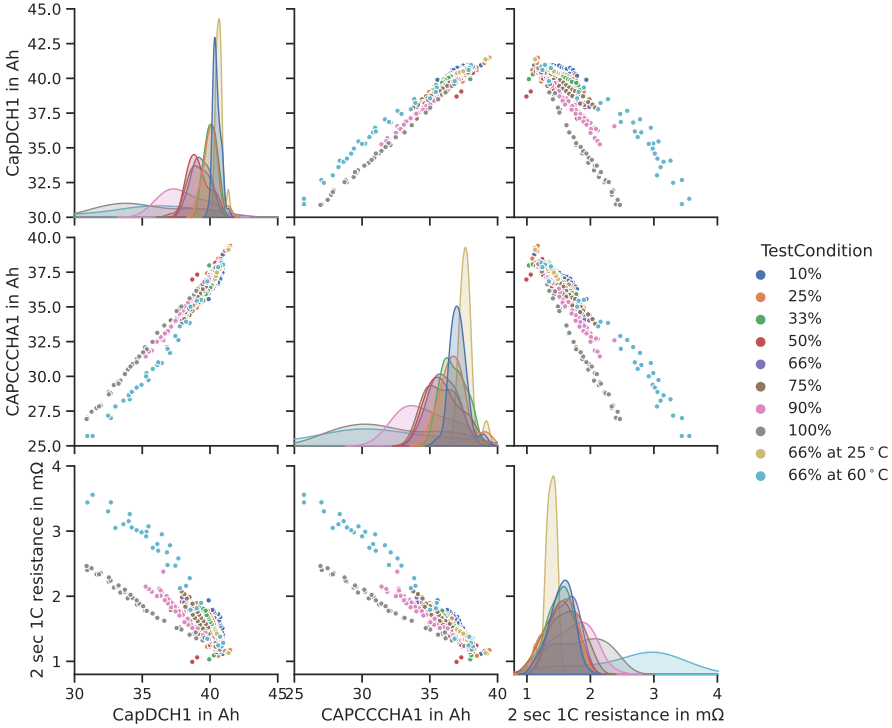

Figure 5.8: Correlation of discharge capacity, charge capacity and pulse resistance over calendar ageing for dataset Schönberger-2019. Colour represents different test conditions of calendar test with SOC shown in legend. Temperature of test is 35 °C if not stated otherwise in legend.

6 Stochastic battery ageing model

In this chapter, a stochastic battery ageing model and its implementation is described. This includes an electrical model, a thermal model as well as an ageing model. In addition, a model library named CXML was developed for all models to combine models from different cells to approximate the cell behaviour when measurement data is lacking. Parts of the results are published in [248] and [249].

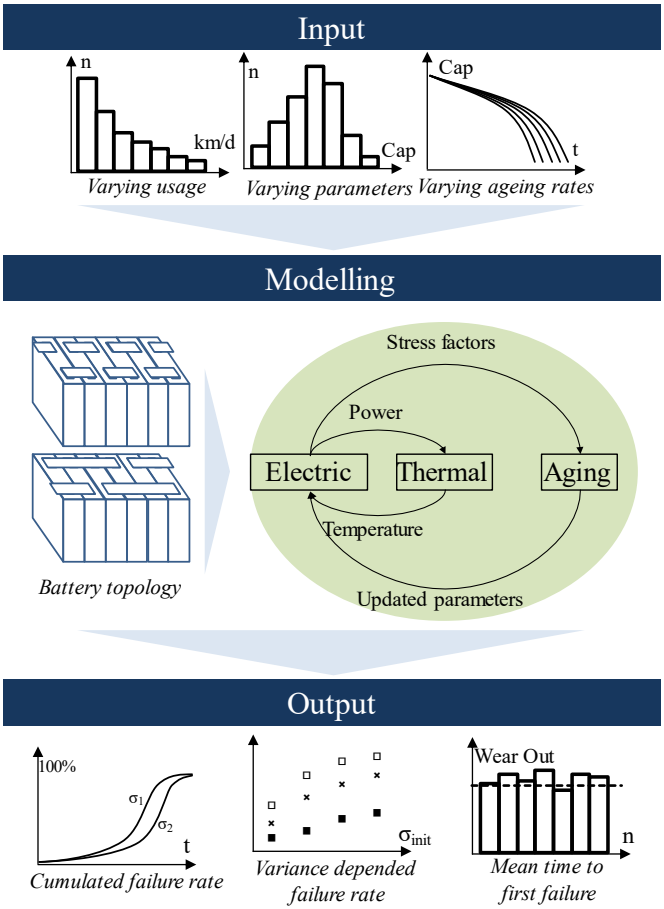

Figure 6.1: Overview of the stochastic battery ageing model.

6.1 Electrical model

An electrical model seen in Figure 6.2 describes the electrical behaviour of the battery, with current or power and temperature as input and voltage, current, SOC and power as output. The electrical response of batteries can be modelled with various levels of detail, mostly based on electrochemical models based on the early work of Newman et al.[250] [251] [252] or equivalent-circuit-models (ECM).

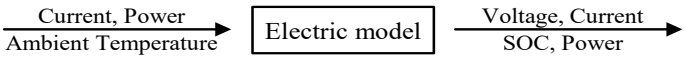

Figure 6.2: Input and output of an electrical model.

Depending on the application, simple models with just an equivalent circuit of a resistance in series to capacitance might be suitable, allowing very fast computing times. The data for parametrising the ECM are obtained with electrochemical impedance spectroscopy (EIS) and current pulses. All measurements should be performed in a temperature-controlled environment since some parameters are highly temperature depended. In [183], Witzenhausen proposed a measurement scheme consisting of EIS and current pulses at different charge levels and temperatures. With the described measurement scheme, physically motivated complex models and simpler ECM models can be parametrised.
The battery simulation framework for ECM used in work is described in Hust [253] and is available online at https://git.rwth-aachen.de/isea/framework. The parameters of the electrical model are part of an electric simulation library.

6.2 Thermal model

As the temperature has an essential impact on the parameters of the electrical simulation, the combination of electrical and thermal simulation is necessary to allow greater accuracy, especially at higher currents, which lead to a self-heating of the battery. The electric model calculates the heat generated within the cell through ohmic losses and side reactions and is used as input for the thermal model as seen in Figure 6.3, and temperature is the output. The spatial resolution of the thermal model is directly coupled to the computing time, and a trade-off must be made. For small cells, for example, a coarse spatial temperature resolution is

enough since gradients are low. For big cells, parts of the cell in direct proximity to the cooling system are significantly cooler under heavy load, and a finer grid should be applied.

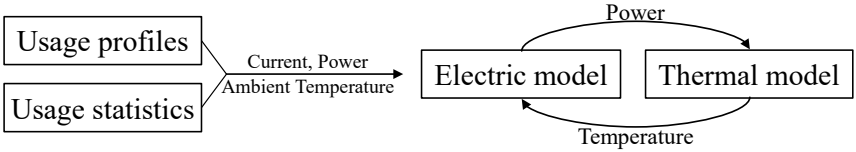

Figure 6.3: Input and output for a thermal model in conjunction with an electric model.

The thermal model is part of the simulation framework described in Hust [253] and depends on heat capacity, cell weight density and heat conductivity. Heat conductivity is typically anisotropic since heat conductivity is much higher in-plane due to the copper/aluminium current collectors than through-plane over the electrode/separator stack. The parameters of the thermal models used in this work are from literature and shown in Table 6.1. When a thermal model was unavailable for a given cell, the parameters of the cell closest in form factor were used.

Table 6.1: Thermal parameters of different cell types used in this work.

Cell	Heat Capacity *J/kg K*	Heat Conductivity (x, y, z or r, z) *W/mK*	Density *kg/m³*	Source
Prismatic 5 Ah LMO:NMC (10:1) - HardCarbon	854	30, 30, 0.49 (x, y, z)	1961	[229]
Cylindrical 4.4 Ah LFP - Graphite	1020	0.4 , - (r, z)	2135	[254]
Cylindrical 3.1 Ah NCA - Graphite	892	2.17, 31.2 (r, z)	2830	[253]
Pouch LCO – Graphite	1028	37, 37, 1.63 (x, y, z)	2510	[255]
Pouch LCO – Si:C	990	32, 32, 1.19 (x, y, z)	2510	[255]

6.3 Ageing model

An ageing model predicts the function and parameters of the battery from specific stress factors. Ageing models for lithium-ion batteries vary in their level of abstraction. In basic terms of Failure mode and effects analysis (FMEA), those levels are classified as effect level, mode level, and mechanism level. As seen in Figure 6.4, the highest level, effect level, are the observable states of capacity fade and rise of internal resistance or power fade.

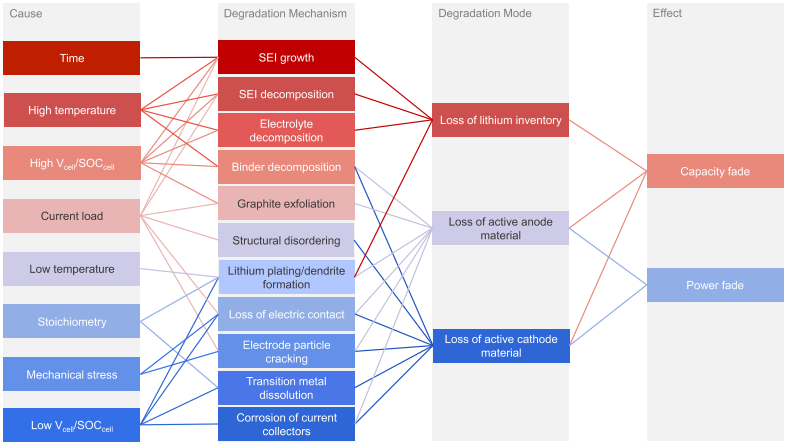

Figure 6.4: Influence of degradation modes on capacity and power fade and degradation mechanisms and their root causes. CC-BY Birkl et al. [256].

For more details, capacity fade is subdivided into modes, on the one hand, the irreversible loss of lithium inventory and loss of active material [256] and on the other hand, reversible modes like homogeneity of lithium distribution or the passive anode effect [196]. For even a greater detail level, individual degradation mechanisms can be modelled with their cause as input [257].

In this work, two kinds of ageing models were used: a semi-empirical effect ageing model based on Schmalstieg et al. [255] and a degradation mode based model from Dubarry et al. [258]. The stress factors are cumulated for both models and simulation parameters updated at certain time intervals for a given simulation period, as seen in Figure 6.5.

More detailed models allow for a better understanding of the failure modes and probabilities but depend on characterisation measurements many times more granular. For the passive anode overhang, for example, cells must be disassembled and the electrode dimensions determined.

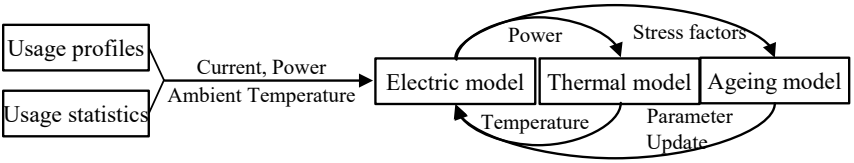

Figure 6.5: Combined model with electric, thermal, and ageing submodel.

Ageing processes inform the semi-empirical ageing model within the battery, such as the growth of the SEI, but it is not directly modelled. Only the effect level capacity and resistance changes of the overall battery are modelled. These changes are described as functions of time, temperature, voltage, DoD, and Ah throughput [259]. For example, elevated temperatures and high SoCs induce a high ageing rate. Figure 6.6 shows a schematic of the model based on Ecker and Schmalstieg [214], [259], and it is split into a cycle ageing and a calendar ageing. Calendar ageing is independent of the usage but is dependent on the SOC, temperature and cell age. Cycle ageing is dependent on the charge throughput, the cycle depth and the mean SOC of the battery during operation.

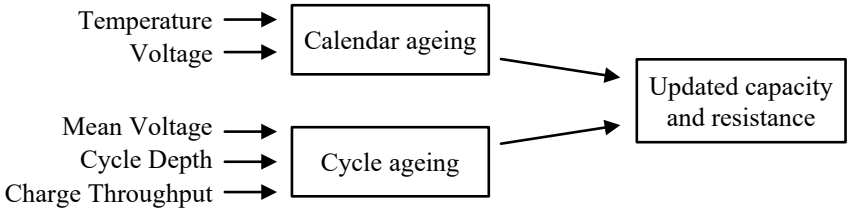

Figure 6.6: Structure of semi-empirical effect ageing model from Schmalstieg et al. [259].

To derive the parameters for the ageing model, first, the calendar ageing function is determined. For example, Figure 6.7 shows an ageing test from [199], in a) degradation curves of all different SOCs at 50 °C are shown, and in b) the complete ageing matrix of this dataset. Next, the parameters of the ageing equations are fitted to ageing data and then used for the cycle ageing fit. Since all

ageing tests also have a time component, calendar ageing is also present in all cycling tests. Therefore, the calendar ageing factor is deducted before the cycle ageing influence is determined.

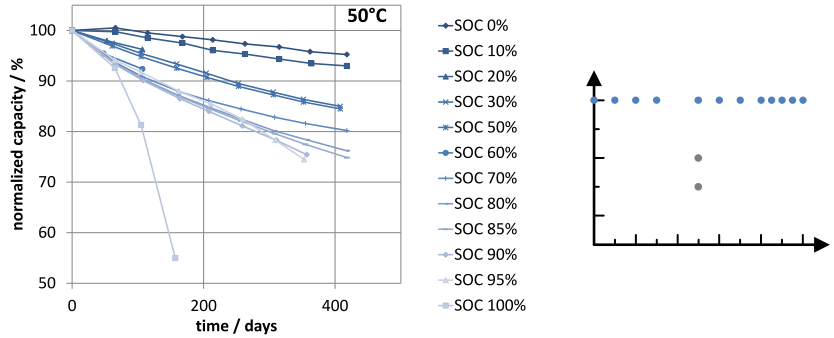

Figure 6.7: a) Calendar ageing test at different SOC at 50°C as part of a more extensive test setup from Ecker et al. [199] b) corresponding ageing matrix, blue dots represent tests shown in a), dots for tests not shown are grey.

The other model used in this work is based on degradation modes from Dubarry et al. [258]. Instead of modelling the capacity/power fade directly, a physical informed intermediate step with degradation mechanisms and modes. Three distinct degradation modes are differentiated: First, Loss of Lithium Inventory (LLI) describes the amount of lithium lost to side reactions or trapped. Second Loss of Active Material at the anode or Negative Electrode (LAM_{NE}) describes the amount of active material not available anymore, such as through particle cracking and exfoliation leading to a loss of electrical contact. Similarly, the ionic contact can be inhibited through covering layers. Both electrical, as well as ionic contact, is necessary to charge and discharge. Loss of Active Material at the cathode or Negative Electrode is named LAM_{NE} accordingly.

For example, as seen in Figure 6.3, the degradation mechanism SEI growth leads to the degradation mode of loss of lithium inventory, causing the effect of capacity loss. On the other hand, the mechanism is caused by the stress factors time, high temperatures, high voltages, and current loads, as shown in Figure 6.8.

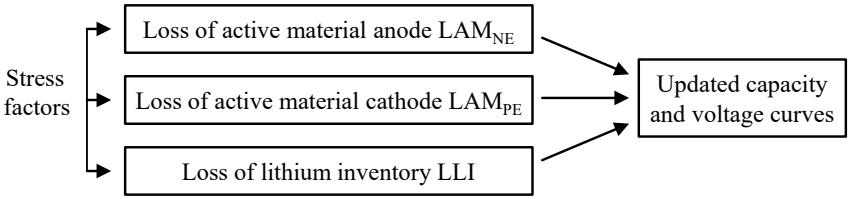

Figure 6.8: Degradation mode based ageing model by Dubarry et al. [258].

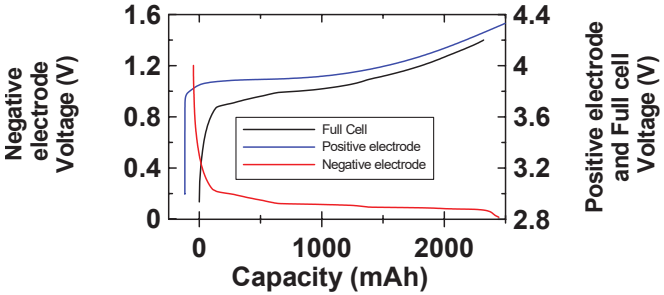

Figure 6.9 Voltage vs capacity for full and half-cell slow discharge curves allow tracking the electrodes' matching. Dahn et al. [260] Reproduced with permission from IOP Publishing.

To determine the parameters for this model in a first step, slow discharge rate measurements of the full cell and half-cell measurement for both electrodes are needed. With either the DVA or ICA technique, the shape of the derivative of the discharge curve is used to determine the matching between anode and cathode voltage curves to combine to the full cell curve (Figure 6.9).

For simulations in this work, the model parameters are used from Dubarry et al. [261], and the per-cycle degradation modes were extracted to LLI is 0.033 %, LAM_{PE} 0.01 % and LAM_{NE} to 0.005 %. This degradation value from literature is used since the datasets used for the other models did not contain all the necessary measurements to track the modes during ageing.

This ageing model not only scales the cell voltage response as seen in these discharge curves but simulates the underlying electrode combination and the electrode specific degradation and their combination. In this example, the battery simulation is run for 720 cycles with an update of the ageing model every 60 cycles. Figure 6.10 a) shows the discharge curves for different ageing conditions

relative to the SOC relative to the apparent capacity and b) relative to the nominal capacity.

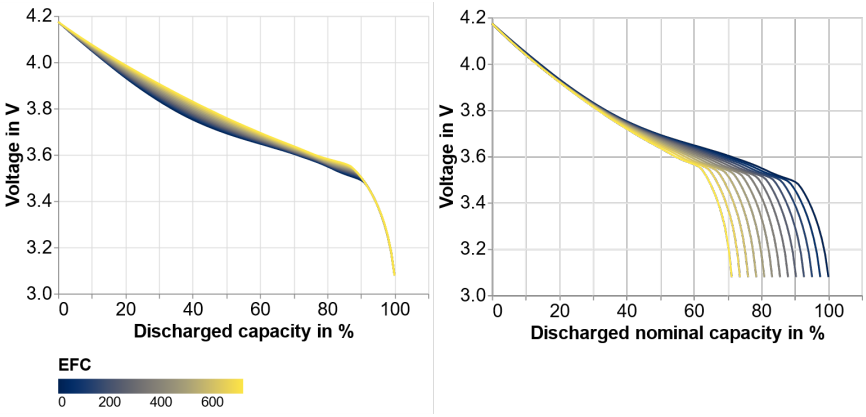

Figure 6.10: Degradation mode based ageing simulation with the model by Dubarry et al. [261].

The differences in voltage response are caused by differences in the amount of LLI and LAM. With the equal loss of each of the values, the voltage curve would keep the same shape.

6.4 Monte-Carlo Simulation & Input variation

The Monte-Carlo-Method or Monte-Carlo simulation describes functions or algorithms which use random numbers as input. As seen in Figure 6.11, varying usage with current profiles, varying parameters of the electric simulation, for example, capacity, and varying ageing rates in the battery ageing model are used. Part of the Monte-Carlo simulation is the use of random numbers or mostly pseudo-random numbers in computing. Since the random values are assigned before the ageing simulation, the random number generator can be called in series. This addresses the problem of software pseudo-random-number generators in parallel computing. Parallel calls of the random functions might produce non-random numbers due to the same seed values [262].

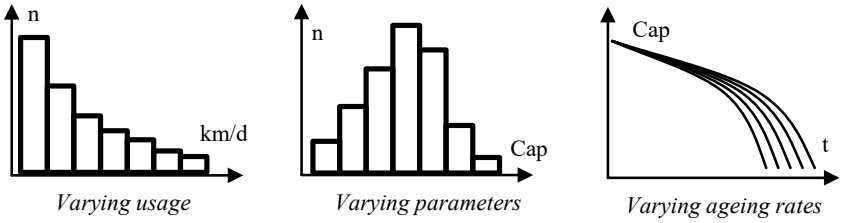

Figure 6.11: Random input parameters for Monte-Carlo simulation. Varying usage through current/power profiles, initial parameters of the electric model and ageing rates.

As Figure 6.12 shows, simulating variation with a Monte-Carlo Simulation is as follows; first ageing experiments are evaluated as shown in Chapter 4, and an ageing model fitted. The fitting error of an ageing rate distribution is derived as a Gaussian distribution with the fitting value as mean and with the same standard deviation. Within the model library CXML, the distribution of the parameters of the ageing model is defined. This ageing rate distribution is an estimation of population variability and can now be used to compare different datasets as well as be used for further simulations. As seen in Chapter 3.5, the sample size, mostly 3 cells per the ageing condition, cannot be regarded as a "big enough" sample size but is limited by data availability. In future work, if resources are available, more extensive ageing tests with around 10 cells per ageing condition would significantly increase the accuracy of the population estimation.

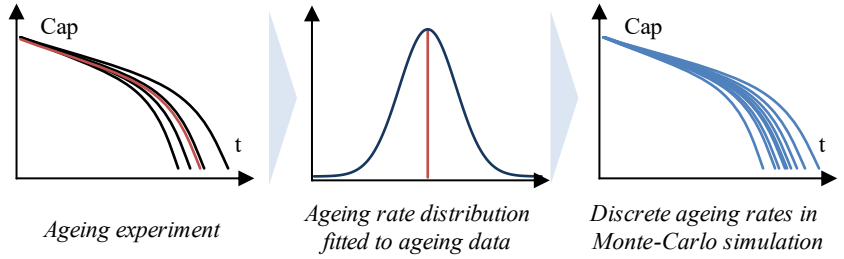

Figure 6.12: From ageing experiments, an ageing rate distribution is derived and used to create random ageing rates for the Monte-Carlo simulation. The mean of the ageing rate distribution is marked in red and also shown as the fit of the curves in the ageing experiment

For load profiles in addition to simple constant current cycling, more complex profiles, for example, the Worldwide harmonized Light vehicles Test Procedure (WLTP), are used. Since the WLTP only defines a target velocity, a real vehicle or full vehicle model is necessary to determine the power demand. The model used to create power profiles in this work is described in [263]–[265] and uses a full vehicle model including a driver model, drive train, aerodynamics, power electronics as well as a battery system.
In [128], [266], Dubarry et al. describe a combined ageing and electrical model framework. Based on an electric circuit model, the Dubarry ageing model described in 6.3, battery pack models as well as BMS models, the behaviour of an aged battery pack can be modelled. The critical difference in the simulation presented here is the feedback loop from ageing to the electrical-thermal simulation enabling intermediate steps within the ageing model.

6.5 Stochastic simulation

In the development, numerous test cases were simulated to test different parts of the model framework as well as the evaluation of such simulated data. Over 5.000 packs, 500.000 cells were simulated with over 20 different electrical models, 5 thermal models and 2 ageing models generating more than 5 Terabytes of simulation data with around 40.000 CPU core hours of computing. As an example for the modelling framework in the following, two applications of stochastic ageing simulations are shown.
The first use case is to test the robustness of the battery system towards variations in the battery cell properties. If the system is also robust with cells with higher variability, manufacturing can be allowed wider tolerances. This can lead to tools being used for an extended time in production even if the initial specifications can no longer be met. In addition, lithium-ion batteries typically go through a grading system where the best cells are sorted into grade A and cells below a certain threshold in grade B or C [85]. A system allowing a broader range of cells can therefore be cheaper.
The second use case is optimising the battery topology with a given cell variability. In this case, the influence of parallel and serial connections is investigated. However, there are limits for the design space depending on the application. Connecting all cells in parallel, for example, provides higher robustness of the system but lowers the pack voltage to the single-cell voltage,

which is not suitable for high-power applications. In electric vehicles, one degree of freedom is system voltages between 400 V and 800 V. Here, not only does the number of voltage levels to be monitored by the BMS increases with 800 V, and also fewer cells are connected in each parallel connection. Since the whole system performance depends on the weakest link in a serial connection, weak cells can barely be compensated for with fewer parallel cells.

Before the impact of cell variations is analysed in different topologies in the second part of this section, the spread in ageing is evaluated for single cells, but different spreads in cell properties. Therefore, the degradation mode model from Dubarry is implemented. All three parameters of the model, loss of lithium inventory and loss of active material at anode and cathode, are considered. All cells are modelled with the same stress profile and only differ in the respective ageing model's parameters assigned from an ageing rate distribution before the Monte-Carlo simulation. All simulations were run for the 720 cycles with an ageing step every 60 cycles, and the results are shown in Figure 6.13- Figure 6.15.

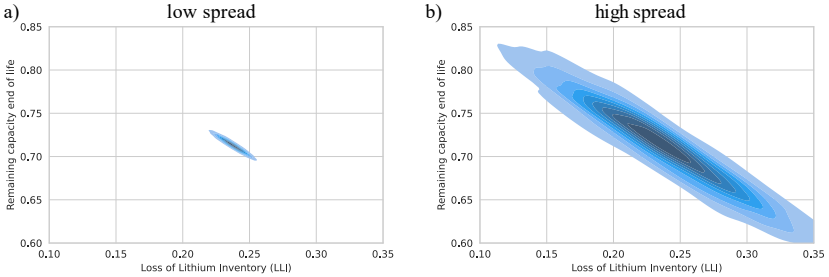

Figure 6.13: Remaining capacity at the end of the simulation vs Loss of Lithium Inventory for a) a low spread and b) a high spread in ageing parameters.

Figure 6.13 shows the loss of lithium inventory vs the remaining capacity at the end of the simulation. The low spread of ageing rates shown with a standard deviation of 3 % in a) comprises of 10,000 cells, and the high spread of ageing rates with a standard deviation of 10 % in b) of 1,000 and both plots show the same mean values of the distribution. Both plots depict the kernel density estimation (KDE) instead of a scatter plot to better show data points very close to each other. A dark colour indicates a high probability, and lines of equal probability are between two different coloured areas. The higher the correlation in the KDE plot, the tighter the plot shape gets, so a correlation of 1 would be

shown as a straight line, and no correlation would be shown as round circles. In Figure 6.13, both graphs a) and b) show a correlation between LLI and the remaining capacity, but the plane's width covered by the KDE for plot b) is significantly increased.

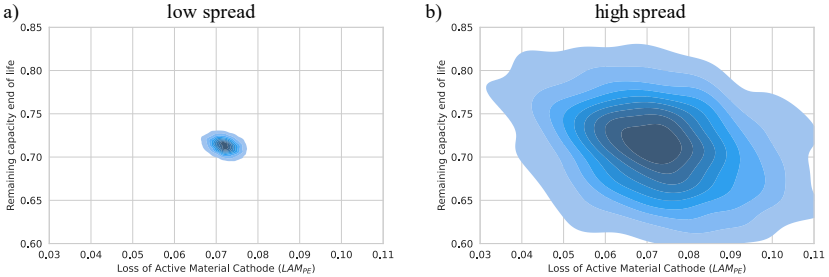

Figure 6.14: Remaining capacity at the end of the simulation vs Loss of Active Material at the Positive Electrode a) for low spread b) for high spread.

In Figure 6.14, similar plots are shown for the Loss of active material on the positive electrode. Again, the low spread of ageing rates shown in a) comprises 10,000 cells, and the high spread of ageing rates in b) of 1,000. Here a small correlation is visible so that the outer bound of the KDE for a given LAM_{PE} includes a range of the remaining capacity of more than 20%.

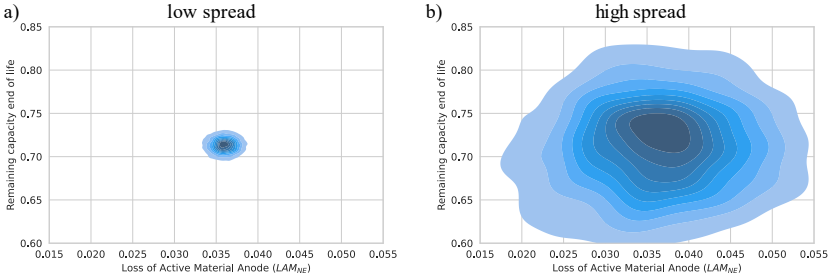

Figure 6.15: Remaining capacity at the end of the simulation vs Loss of Active Material at the Negative Electrode. a) for low spread b) for high spread.

The last plot for the two spreads in ageing rate, Figure 6.15, shows the KDE of Loss of active material at the negative electrode vs the remaining capacity. Here again, a) is for the low spread and b) for the high spread scenario. In this representation, LAM_{NE} has a low correlation with the remaining capacity, visible

as high roundness in the KDE plot. The correlation to remaining capacity is beneficial if one of the above-mentioned degradation modes is observable while capacity is not. In addition, analysed for different cells, it indicates which mode is dominating the degradation.

After the spread in ageing rate and the correlation of the degradation modes are evaluated for single cells, the different spreads in cell properties are now analysed regarding different topologies. Therefore, a generic battery module consisting of 100 cells is created for the simulation framework. Each cell has specific start parameters, e.g., capacity and specific ageing rates assigned from the ageing rate distributions mentioned earlier from the prior ageing model fit. 300 modules were simulated using the three topologies 100s1p, 20s5p and 50s2p, meaning that 30,000 virtual cells were simulated in total.

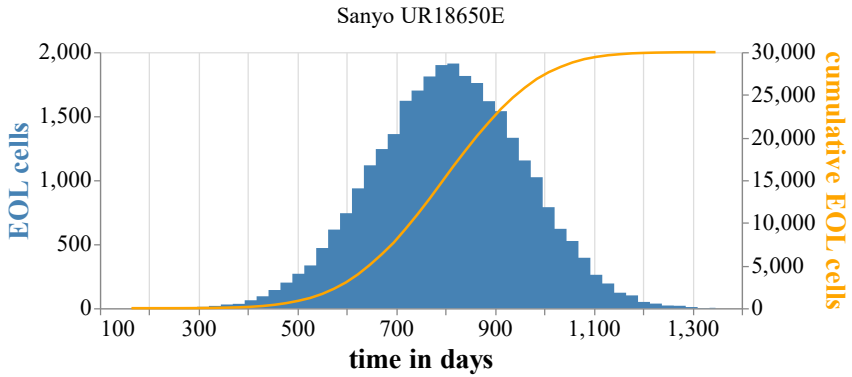

Figure 6.16: Number of cells reaching end-of-life after x days (blue histogram) for 30,000 cells. In orange cumulative of cells already reaching their end-of-life.

Figure 6.16 illustrates the simulated lifetime distribution of those 30,000 cells from Sanyo. The blue histogram depicts the number of cells that reach the end-of-life criterion, here 80 % remaining capacity, at a certain time in days. This is depending on the initial parameters as well as the ageing rates. In orange, the cumulative number of cells is shown that have already reached the end-of-life. The first cells start to fail at around 300 days, and the last cells die at about 1,200 days. So, the mean value is around 800 days. Additionally, most cells reach the end-of-life criterion at around 800 days.

Since all cells in this simulation are part of a pack, the serial connection's worst-performing cell/parallel connection determines the whole pack capacity.

Therefore, the distribution of failing packs also changes since there are also packs with comparable good cells in the whole pack failing later. This is shown in Figure 6.17, where the days until the end-of-life for packs are shown in blue, and the cumulative number of packs failed in orange.

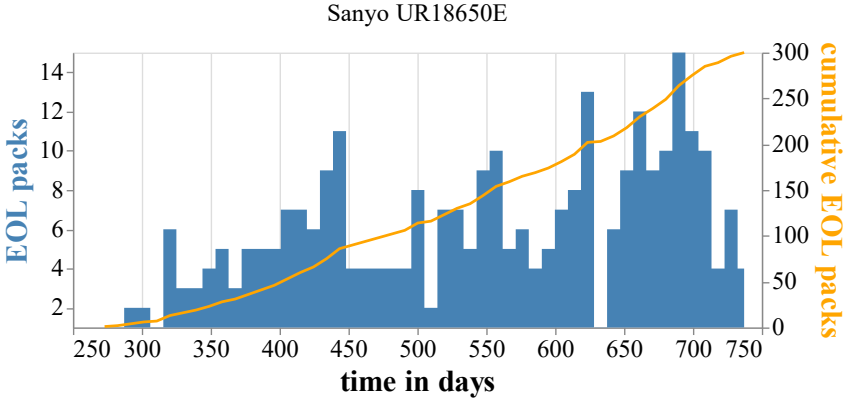

Figure 6.17: In the blue histogram of days until end-of-life is reached for 300 packs. In orange cumulative of packs already reaching their end-of-life.

Looking closer into the data, the three topologies can be distinguished as shown in Figure 6.18 and Figure 6.19. The 100 cells of each pack are part of three different topologies, namely 100s1p in blue, 20s5p in orange and 50s2p in red. In 100s1p, all cells are in serial, while 20s5p has 5 cells in parallel and 50s2p 2 cells in parallel.

As seen in Figure 6.18, the differences between the topologies on cell level are minimal. The differences in the 100s1p configuration can be explained by the DOD dependency of the ageing rate in the model. When a cell has a lower capacity, the same charge throughput equals a higher relative depth of discharge. With the dependency in the ageing rate model of the DOD, the low-capacity cell also has a higher ageing rate. This influences the packs with only one cell in parallel the most, and they, on average, die the quickest. But the effect has limits, so there is no significant difference between two cells in parallel and five cells in parallel since the average capacity of the parallel connection is already much closer together.

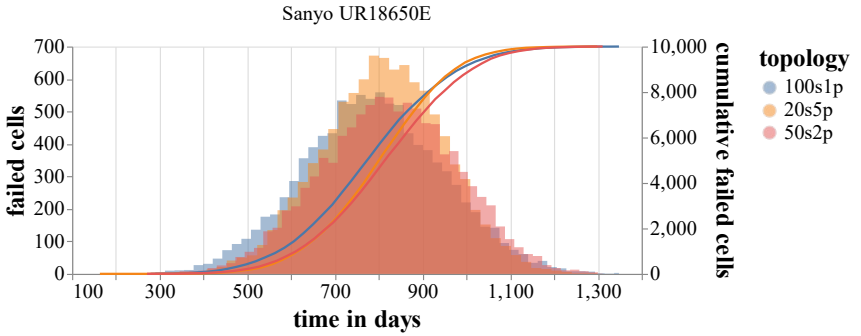

Figure 6.18: In the histograms of days until end-of-life is shown for 3 topologies with 10,000 cells each. In addition, the cumulative of cells already reaching their end-of-life is shown.

The most significant effect is shown in Figure 6.19, where the cumulative failure rate of packs is shown, and there are significant differences between the topologies.

Since in the serial connection, the worst cell determines the end of life of the pack, with the first cells dying at around 300 days also the first packs of the 100s1p pack topology start to fail. After that, the 2p topology can be found in the middle, with packs dying from 450 to 650 days. The other packs, with the five parallel cells, start to die last at around 600 days.

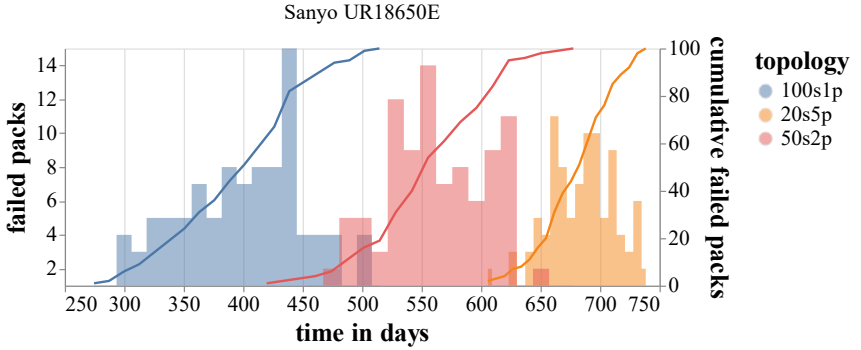

Figure 6.19 In the histograms, the days until end-of-life is shown for 3 topologies for 100 packs each. In addition, the cumulative of packs already reaching their end-of-life.

6.6 Chapter conclusion

Based on an impedance-based cell mode, a modelling framework was developed to simulate batteries' electrical and thermal behaviour as well as their ageing behaviour in different configurations. With load profiles, usage patterns and lifetime requirements, batteries can be simulated multiple times as part of a Monte-Carlo simulation with cell properties derived from the ageing rate distributions and initial spread distributions. Within the framework, the number of failed cells, as well as the cumulative amount cells, can be calculated given a certain topology and distribution, enabling comparisons on a “fleet-level”.

7 Summary and Outlook

7.1 Summary

This work deals extensively with the variation of properties of battery cells of one type. This includes the analysis of a very large amount of experimental data, the development of a system for the evaluation and presentation of performance data of batteries in comparison, the development of test procedures with statistical relevance and the modelling of ageing taking into account the variance of the individual cells.

Within this work, a framework to simulate battery ageing, including variation in ageing rate and initial parameters, is introduced. Derived from various degradation datasets, empirical capacity-versus-time ageing models were parametrised with data from more than 1,000 cells, with an automated method to analyse battery ageing data.

Overall, with the deeper understanding and quantification of cell-to-cell variation developed within this work, advances in several aspects have been achieved. Most relevant is target-oriented testing of batteries incorporating variation for enhanced statistical certainty, resulting in decreased cost and testing efforts through a predetermined sample size. The minimum number of cells, which should be tested to accurately represent population variability, was estimated by assuming that the model parameters could be drawn from a distribution describing a larger population and then using a hierarchical Bayesian approach. Thus, the minimum data for each point in the test matrix was determined to be from at least 9, 11 or 13 cells for a consistent fit depending on the complexity of the ageing model with 1, 2 or 3 parameters, respectively.

A thorough evaluation and correlation of the variety of possible health indicators proved a possibility to reduce the measurement effort during check-ups. A high correlation between two or more indicators reveals that measuring one of them is sufficient to quantify ageing reliably. In particular, the resistance measurements with pulses showed a high correlation for different pulse lengths, currents and states of charge.

Furthermore, this thesis introduced ENPOLITE, an approach that allows a comprehensive comparison and an overall evaluation of lithium-ion batteries by modifying the Ragone plot and incorporation lifetime and testing conditions. It considers the trade-off between multiple requirements, including energy density,

power density, and lifetime. As a result, the critical operating parameters of large datasets of lithium-ion battery cycling and calendar ageing across multiple battery chemistries and usage conditions can be compared unbiased.
In addition, lifetime prognosis models with additional confidence intervals allow more representative predictions of lifetime and failure scenarios in the application considering different topologies.
The research in this thesis aims to optimise system topologies for individual applications to find suitable cells, avoid oversizing battery systems and give forecasts of a lifetime and quantifiably failure rates for battery packs while decreasing cost. A simulation toolchain was developed to incorporate variability and spread of ageing rates in the system design process. In the scope of the simulation tool, battery topologies can be simulated with varying usage profiles, cell parameter spreads and varying ageing rates. The simulations showed increasing robustness against cell failure for different topologies when a larger number of cells are connected in parallel. Thus, with the help of the toolchain developed in this work, cell-to-cell variations can be accounted for and their effects included in the cell selection and design process. The first step towards allowing differences in the cell properties and managing them in the application is made with this work. The toolchain can handle the statistical spread of cell-to-cell variation in the initial state after production and even quantifies degradation, which differs strongly. Still, a reliable prediction is difficult even with a large amount of data as numerous stress factors have to be considered.

7.2 Outlook

To really make the expensive rigorous process monitoring and rigid quality control dispensable without increasing the scrap rate, more work on this topic is necessary. The key lies in collecting as much and valuable data in a given time to incorporate the uncertainties experienced in the ageing test into simulation models. This will include developing techniques to accelerate ageing as fast as possible without triggering additional and unwanted ageing mechanisms. Secondly, the measuring techniques need to develop in order to already track slight changes and ageing effects, so cells need to be tested for a shorter time to predict their ageing behaviour earlier. Lastly, techniques for testing more cells at the same time (parallel testing) need to be developed.

Additional ageing models can also be implemented, especially on a more detailed level of degradation mechanisms. Those models will need even more data, so good data availability is key for all future work, including the basis of stochastic ageing models.
Since for batteries, a lot of the associated cost is during investment, good ageing prediction enables an informed decision based on the total cost of ownership and reduces the premium rates associated with financing uncertainty. Therefore, good prediction enables the confidence to make necessary investments early to move to a renewable economy.

8 List of Abbreviations

BEV	Battery electric vehicle
BMS	Battery management system
BOL	Begin of life
CCCV	Constant current constant voltage
CDF	Cumulative distribution function
CPU	Central processing unit, main computer processor
CT	Computer tomography, 3D-Xray
CTCV	Cell-to-cell variation
DOD	Depth of discharge/cycling depth
DVA	Differential voltage analysis
ECM	Equivalent circuit model
EIS	Electrochemical impedance spectroscopy
ENPOLITE	ENergy-POwer-LIfetime-TEmperature plot
EOCV	End of charge voltage
EODV	End of discharge voltage
EOL	End of life
EV	Electric vehicle
HLD	Homogeneity of lithium distribution
ICA	Incremental capacity analysis
LAM	Loss of active material
LFP	Lithium iron phosphate (cathode material)
LLI	Loss of lithium inventory
LMO	Lithium manganese oxide (cathode material)
LTO	Lithium titanate oxide (anode material)
KDE	Kernel density estimation

MLB	Multi-level Bayes
NCA	Lithium nickel cobalt aluminium oxide (cathode material)
NE	Negative electrode
NMC	Lithium nickel manganese cobalt oxide (cathode material)
OCV	Open circuit voltage
PDF	Probability density function
PE	Positive electrode
qOCV	Quasi open circuit voltage
RMSE	Root-mean-square error
SEM	Scanning electron microscopy
SEI	Solid-Electrolyte-Interface
SOC	State-of-Charge
SOH	State-of-Health
SOP	State-of-Power
SSD	Sub-sample distribution
STEM	Scanning transmission electron microscopy
WLTP	Worldwide harmonized Light vehicles Test Procedure

9 Bibliography

[1] G. E. Blomgren, “The Development and Future of Lithium Ion Batteries,” *J. Electrochem. Soc.*, vol. 164, no. 1, pp. A5019–A5025, Jan. 2017, doi: 10.1149/2.0251701jes.

[2] O. Schmidt, S. Melchior, A. Hawkes, and I. Staffell, “Projecting the Future Levelized Cost of Electricity Storage Technologies,” *Joule*, vol. 3, no. 1, pp. 81–100, Jan. 2019, doi: 10.1016/j.joule.2018.12.008.

[3] H. Li, “Practical Evaluation of Li-Ion Batteries,” *Joule*, vol. 3, no. 4, pp. 911–914, Apr. 2019, doi: 10.1016/j.joule.2019.03.028.

[4] M. S. Ziegler and J. E. Trancik, “Re-examining rates of lithium-ion battery technology improvement and cost decline,” *Energy Environ. Sci.*, vol. 14, no. 4, pp. 1635–1651, 2021, doi: 10.1039/D0EE02681F.

[5] N. P. Lebedeva, F. D. Persio, T. Kosmidou, D. Dams, A. Pfrang, A. Kersys, and L. Boon-Brett, “Amount of Free Liquid Electrolyte in Commercial Large Format Prismatic Li-Ion Battery Cells,” *J. Electrochem. Soc.*, vol. 166, no. 4, pp. A779–A786, Jan. 2019, doi: 10.1149/2.1151904jes.

[6] G. Kavlak, J. McNerney, and J. E. Trancik, “Evaluating the causes of cost reduction in photovoltaic modules,” *Energy Policy*, vol. 123, pp. 700–710, Dec. 2018, doi: 10.1016/j.enpol.2018.08.015.

[7] N. A. Sepulveda, J. D. Jenkins, A. Edington, D. S. Mallapragada, and R. K. Lester, “The design space for long-duration energy storage in decarbonized power systems,” *Nature Energy*, pp. 1–11, Mar. 2021, doi: 10.1038/s41560-021-00796-8.

[8] C. Yang, J. Chen, T. Qing, X. Fan, W. Sun, A. von Cresce, M. S. Ding, O. Borodin, J. Vatamanu, M. A. Schroeder, N. Eidson, C. Wang, and K. Xu, “4.0 V Aqueous Li-Ion Batteries,” *Joule*, vol. 1, no. 1, pp. 122–132, Sep. 2017, doi: 10.1016/j.joule.2017.08.009.

[9] O. Schmidt, M. Thomitzek, F. Röder, S. Thiede, C. Herrmann, and U. Krewer, “Modeling the Impact of Manufacturing Uncertainties on Lithium-Ion Batteries,” *J. Electrochem. Soc.*, vol. 167, no. 6, p. 060501, Mar. 2020, doi: 10.1149/1945-7111/ab798a.

[10] D. Andre, H. Hain, P. Lamp, F. Maglia, and B. Stiaszny, “Future high-energy density anode materials from an automotive application perspective,” *J. Mater. Chem. A*, vol. 5, no. 33, pp. 17174–17198, Aug. 2017, doi: 10.1039/C7TA03108D.

[11] D. Andre, S.-J. Kim, P. Lamp, S. F. Lux, F. Maglia, O. Paschos, and B. Stiaszny, “Future generations of cathode materials: an automotive industry perspective,” *J. Mater. Chem. A*, vol. 3, no. 13, pp. 6709–6732, Mar. 2015, doi: 10.1039/C5TA00361J.

[12] R. Schmuch, R. Wagner, G. Hörpel, T. Placke, and M. Winter, “Performance and cost of materials for lithium-based rechargeable automotive batteries,” *Nature Energy*, vol. 3, no. 4, p. 267, Apr. 2018, doi: 10.1038/s41560-018-0107-2.

[13] J. O. Besenhard and H. P. Fritz, “The Electrochemistry of Black Carbons,” *Angewandte Chemie International Edition in English*, vol. 22, no. 12, pp. 950–975, 1983, doi: 10.1002/anie.198309501.

[14] J. R. Dahn, “Phase diagram of Li_{x}C_{6},” *Phys. Rev. B*, vol. 44, no. 17, pp. 9170–9177, Nov. 1991, doi: 10.1103/PhysRevB.44.9170.

[15] M. Genovese, A. J. Louli, R. Weber, S. Hames, and J. R. Dahn, “Measuring the Coulombic Efficiency of Lithium Metal Cycling in Anode-Free Lithium Metal Batteries,” *J. Electrochem. Soc.*, vol. 165, no. 14, pp. A3321–A3325, Jan. 2018, doi: 10.1149/2.0641814jes.

[16] W.-J. Zhang, “A review of the electrochemical performance of alloy anodes for lithium-ion batteries,” *Journal of Power Sources*, vol. 196, no. 1, pp. 13–24, Jan. 2011, doi: 10.1016/j.jpowsour.2010.07.020.

[17] S. J. Harris and P. Lu, “Effects of Inhomogeneities—Nanoscale to Mesoscale—on the Durability of Li-Ion Batteries,” *J. Phys. Chem. C*, vol. 117, no. 13, pp. 6481–6492, Apr. 2013, doi: 10.1021/jp311431z.

[18] L. K. Willenberg, P. Dechent, G. Fuchs, D. U. Sauer, and E. Figgemeier, “High-Precision Monitoring of Volume Change of Commercial Lithium-Ion Batteries by Using Strain Gauges,” *Sustainability*, vol. 12, no. 2, Art. no. 2, Jan. 2020, doi: 10.3390/su12020557.

[19] A. J. Louli, J. Li, S. Trussler, C. R. Fell, and J. R. Dahn, “Volume, Pressure and Thickness Evolution of Li-Ion Pouch Cells with Silicon-Composite Negative Electrodes,” *J. Electrochem. Soc.*, vol. 164, no. 12, pp. A2689–A2696, Jan. 2017, doi: 10.1149/2.1691712jes.

[20] M. Wetjen, S. Solchenbach, D. Pritzl, J. Hou, V. Tileli, and H. A. Gasteiger, “Morphological Changes of Silicon Nanoparticles and the Influence of Cutoff Potentials in Silicon-Graphite Electrodes,” *J. Electrochem. Soc.*, vol. 165, no. 7, pp. A1503–A1514, Jan. 2018, doi: 10.1149/2.1261807jes.

[21] E. Peled and S. Menkin, “Review—SEI: Past, Present and Future,” *J. Electrochem. Soc.*, vol. 164, no. 7, pp. A1703–A1719, Jan. 2017, doi: 10.1149/2.1441707jes.

[22] E. Deichmann, L. Torres-Castro, J. Lamb, M. Karulkar, S. Ivanov, C. Grosso, L. Gray, J. Langendorf, and F. Garzon, “Investigating the Effects of Lithium Deposition on the Abuse Responseof Lithium-Ion Batteries,” *Journal of The Electrochemical Society*, vol. 167, no. 9, p. 090552, 2020, doi: 10.1149/1945-7111/ab9941.

[23] F. Holtstiege, P. Bärmann, R. Nölle, M. Winter, and T. Placke, “Pre-Lithiation Strategies for Rechargeable Energy Storage Technologies: Concepts, Promises and Challenges,” *Batteries*, vol. 4, no. 1, p. 4, Mar. 2018, doi: 10.3390/batteries4010004.

[24] M. Roser, “Life Expectancy - Our World in Data.” https://ourworldindata.org/life-expectancy (accessed May 01, 2021).

[25] J. D. Kalbfleisch and R. L. Prentice, *The statistical analysis of failure time data*, 2nd ed. Hoboken, N.J: J. Wiley, 2002.

[26] C. Sundararajan, Ed., *Probabilistic Structural Mechanics Handbook*. Boston, MA: Springer US, 1995. doi: 10.1007/978-1-4615-1771-9.

[27] D. Beck, P. Dechent, M. Junker, D. U. Sauer, and M. Dubarry, “Inhomogeneities and Cell-to-Cell Variations in Lithium-Ion Batteries, a Review,” *Energies*, vol. 14, no. 11, Art. no. 11, Jan. 2021, doi: 10.3390/en14113276.

[28] P. Dechent, S. Greenbank, F. Hildenbrand, S. Jbabdi, D. U. Sauer, and D. Howell, “Estimation of Li-ion degradation test sample sizes required to understand cell-to-cell variability,” *Batteries & Supercaps*, vol. n/a, no. n/a, doi: 10.1002/batt.202100148R1.

[29] “MaxRange Tesla Battery Survey,” *Tesla Motors Club*. https://teslamotorsclub.com/tmc/threads/maxrange.35978/ (accessed Mar. 08, 2021).

[30] B. Delobel, “Lessons Learned from Field Data Analysis, and Future Challenges - Renault EV,” presented at the AABC Europe - xEV BATTERIES, Strasbourg, France, Jan. 30, 2019. [Online]. Available: https://www.advancedautobat.com/europe/

[31] "30 kWh Nissan Leaf firmware update to correct capacity reporting - FlipTheFleet." https://flipthefleet.org/2018/30-kwh-nissan-leaf-firmware-update-to-correct-capacity-reporting/ (accessed Apr. 17, 2019).

[32] D. Myall, "30 kWh Nissan Leaf firmware update to correct capacity reporting," *FlipTheFleet*, Jul. 25, 2018. https://flipthefleet.org/2018/30-kwh-nissan-leaf-firmware-update-to-correct-capacity-reporting/ (accessed Mar. 08, 2021).

[33] R. Prosser, G. Offer, and Y. Patel, "Lithium-Ion Diagnostics: The First Quantitative In-Operando Technique for Diagnosing Lithium Ion Battery Degradation Modes under Load with Realistic Thermal Boundary Conditions," *J. Electrochem. Soc.*, vol. 168, no. 3, p. 030532, Mar. 2021, doi: 10.1149/1945-7111/abed28.

[34] B. Y. Liaw and M. Dubarry, "From driving cycle analysis to understanding battery performance in real-life electric hybrid vehicle operation," *Journal of Power Sources*, vol. 174, no. 1, pp. 76–88, Nov. 2007, doi: 10.1016/j.jpowsour.2007.06.010.

[35] S. F. Schuster, M. J. Brand, P. Berg, M. Gleissenberger, and A. Jossen, "Lithium-ion cell-to-cell variation during battery electric vehicle operation," *Journal of Power Sources*, vol. 297, pp. 242–251, Nov. 2015, doi: 10.1016/j.jpowsour.2015.08.001.

[36] F. Salinas, L. Krüger, S. Neupert, and J. Kowal, "A second life for li-ion cells rescued from notebook batteries," *Journal of Energy Storage*, vol. 24, p. 100747, Aug. 2019, doi: 10.1016/j.est.2019.04.021.

[37] T. Grün, K. Stella, and O. Wollersheim, "Influence of circuit design on load distribution and performance of parallel-connected Lithium ion cells for photovoltaic home storage systems," *Journal of Energy Storage*, vol. 17, pp. 367–382, Jun. 2018, doi: 10.1016/j.est.2018.03.010.

[38] K. Rumpf, A. Rheinfeld, M. Schindler, J. Keil, T. Schua, and A. Jossen, "Influence of Cell-to-Cell Variations on the Inhomogeneity of Lithium-Ion Battery Modules," *J. Electrochem. Soc.*, vol. 165, no. 11, pp. A2587–A2607, Jan. 2018, doi: 10.1149/2.0111811jes.

[39] K. Rumpf, "Causes and effects of inhomogeneity in lithium-ion battery modules: A physicochemical modelling approach," PhD thesis, Technische Universität München, München, Germany, 2018. [Online]. Available: http://mediatum.ub.tum.de?id=1453734

[40] M. Schindler, J. Sturm, S. Ludwig, J. Schmitt, and A. Jossen, "Evolution of Initial Cell-to-Cell Variations During a Three-Year Production Cycle," *eTransportation*, p. 100102, Jan. 2021, doi: 10.1016/j.etran.2020.100102.

[41] S. J. Harris and P. Lu, "Effects of Inhomogeneities—Nanoscale to Mesoscale—on the Durability of Li-Ion Batteries," *J. Phys. Chem. C*, vol. 117, no. 13, pp. 6481–6492, Apr. 2013, doi: 10.1021/jp311431z.

[42] T. C. Bach, S. F. Schuster, E. Fleder, J. Müller, M. J. Brand, H. Lorrmann, A. Jossen, and G. Sextl, "Nonlinear aging of cylindrical lithium-ion cells linked to heterogeneous compression," *Journal of Energy Storage*, vol. 5, pp. 212–223, Feb. 2016, doi: 10.1016/j.est.2016.01.003.

[43] T. Grün, K. Stella, and O. Wollersheim, "Influence of circuit design on load distribution and performance of parallel-connected Lithium ion cells for photovoltaic home storage systems," *Journal of Energy Storage*, vol. 17, pp. 367–382, Jun. 2018, doi: 10.1016/j.est.2018.03.010.

[44] S. Ma, M. Jiang, P. Tao, C. Song, J. Wu, J. Wang, T. Deng, and W. Shang, "Temperature effect and thermal impact in lithium-ion batteries: A review," *Progress in Natural Science: Materials International*, vol. 28, no. 6, pp. 653–666, Dec. 2018, doi: 10.1016/j.pnsc.2018.11.002.

[45] T.-T. Nguyen, A. Demortière, B. Fleutot, B. Delobel, C. Delacourt, and S. J. Cooper, "The electrode tortuosity factor: why the conventional tortuosity factor is not well suited for quantifying transport in porous Li-ion battery electrodes and what to use instead," *npj Computational Materials*, vol. 6, no. 1, Art. no. 1, Aug. 2020, doi: 10.1038/s41524-020-00386-4.

[46] M. M. Forouzan, C.-W. Chao, D. Bustamante, B. A. Mazzeo, and D. R. Wheeler, "Experiment and simulation of the fabrication process of lithium-ion battery cathodes for determining microstructure and mechanical properties," *Journal of Power Sources*, vol. 312, pp. 172–183, Apr. 2016, doi: 10.1016/j.jpowsour.2016.02.014.

[47] I. V. Thorat, D. E. Stephenson, N. A. Zacharias, K. Zaghib, J. N. Harb, and D. R. Wheeler, "Quantifying tortuosity in porous Li-ion battery materials," *Journal of Power Sources*, vol. 188, no. 2, pp. 592–600, Mar. 2009, doi: 10.1016/j.jpowsour.2008.12.032.

[48] D. Antartis, S. Dillon, and I. Chasiotis, "Effect of porosity on electrochemical and mechanical properties of composite Li-ion anodes,"

Journal of Composite Materials, vol. 49, no. 15, pp. 1849–1862, Jun. 2015, doi: 10.1177/0021998314568653.

[49] R. Elango, A. Nadeina, F. Cadiou, V. De Andrade, A. Demortière, M. Morcrette, and V. Seznec, "Impact of electrode porosity architecture on electrochemical performances of 1 mm-thick LiFePO4 binder-free Li-ion electrodes fabricated by Spark Plasma Sintering," *Journal of Power Sources*, vol. 488, p. 229402, Mar. 2021, doi: 10.1016/j.jpowsour.2020.229402.

[50] J. Sieg, M. Storch, J. Fath, A. Nuhic, J. Bandlow, B. Spier, and D. U. Sauer, "Local degradation and differential voltage analysis of aged lithium-ion pouch cells," *Journal of Energy Storage*, vol. 30, p. 101582, Aug. 2020, doi: 10.1016/j.est.2020.101582.

[51] M. Ecker, P. Shafiei Sabet, and D. U. Sauer, "Influence of operational condition on lithium plating for commercial lithium-ion batteries – Electrochemical experiments and post-mortem-analysis," *Applied Energy*, vol. 206, pp. 934–946, Nov. 2017, doi: 10.1016/j.apenergy.2017.08.034.

[52] B. Suthar, P. W. C. Northrop, D. Rife, and V. R. Subramanian, "Effect of Porosity, Thickness and Tortuosity on Capacity Fade of Anode," *J. Electrochem. Soc.*, vol. 162, no. 9, p. A1708, Jun. 2015, doi: 10.1149/2.0061509jes.

[53] M. Singh, J. Kaiser, and H. Hahn, "Effect of Porosity on the Thick Electrodes for High Energy Density Lithium Ion Batteries for Stationary Applications," *Batteries*, vol. 2, no. 4, Art. no. 4, Dec. 2016, doi: 10.3390/batteries2040035.

[54] S. Müller, J. Eller, M. Ebner, C. Burns, J. Dahn, and V. Wood, "Quantifying Inhomogeneity of Lithium Ion Battery Electrodes and Its Influence on Electrochemical Performance," *J. Electrochem. Soc.*, vol. 165, no. 2, pp. A339–A344, Jan. 2018, doi: 10.1149/2.0311802jes.

[55] M. Dubarry, J. Gaubicher, D. Guyomard, N. Steunou, J. Livage, N. Dupré, and C. P. Grey, "Synthesis of Li1+αV3O8 via a Gel Precursor: Part II, from Xerogel to the Anhydrous Material," *Chem. Mater.*, vol. 18, no. 3, pp. 629–636, Feb. 2006, doi: 10.1021/cm051508+.

[56] F. H. Pavoni, L. E. Sita, C. S. dos Santos, S. P. da Silva, P. R. C. da Silva, and J. Scarminio, "LiCoO2 particle size distribution as a function of the state of health of discarded cell phone batteries," *Powder Technology*, vol. 326, pp. 78–83, Feb. 2018, doi: 10.1016/j.powtec.2017.12.059.

[57] L. Yang, H.-S. Chen, W.-L. Song, and D. Fang, "Effect of Defects on Diffusion Behaviors of Lithium-Ion Battery Electrodes: In Situ Optical

Observation and Simulation," *ACS Appl. Mater. Interfaces*, vol. 10, no. 50, pp. 43623–43630, Dec. 2018, doi: 10.1021/acsami.8b15260.

[58] X. M. Liu, A. Fang, M. P. Haataja, and C. B. Arnold, "Size Dependence of Transport Non-Uniformities on Localized Plating in Lithium-Ion Batteries," *J. Electrochem. Soc.*, vol. 165, no. 5, pp. A1147–A1155, Jan. 2018, doi: 10.1149/2.1181805jes.

[59] F. Pouraghajan, A. I. Thompson, E. E. Hunter, B. Mazzeo, J. Christensen, R. Subbaraman, M. Wray, and D. Wheeler, "The effects of cycling on ionic and electronic conductivities of Li –ion battery electrodes," *Journal of Power Sources*, vol. 492, p. 229636, Apr. 2021, doi: 10.1016/j.jpowsour.2021.229636.

[60] W. Zhou, "Effects of external mechanical loading on stress generation during lithiation in Li-ion battery electrodes," *Electrochimica Acta*, vol. 185, pp. 28–33, Dec. 2015, doi: 10.1016/j.electacta.2015.10.097.

[61] J. Christensen, "Modeling Diffusion-Induced Stress in Li-Ion Cells with Porous Electrodes," *J. Electrochem. Soc.*, vol. 157, no. 3, p. A366, Feb. 2010, doi: 10.1149/1.3269995.

[62] N. Lin, Z. Jia, Z. Wang, H. Zhao, G. Ai, X. Song, Y. Bai, V. Battaglia, C. Sun, J. Qiao, K. Wu, and G. Liu, "Understanding the crack formation of graphite particles in cycled commercial lithium-ion batteries by focused ion beam - scanning electron microscopy," *Journal of Power Sources*, vol. 365, pp. 235–239, Oct. 2017, doi: 10.1016/j.jpowsour.2017.08.045.

[63] K. Dai, Z. Wang, G. Ai, H. Zhao, W. Yuan, X. Song, V. Battaglia, C. Sun, K. Wu, and G. Liu, "The transformation of graphite electrode materials in lithium-ion batteries after cycling," *Journal of Power Sources*, vol. 298, pp. 349–354, Dec. 2015, doi: 10.1016/j.jpowsour.2015.08.055.

[64] F. Sun, H. Markötter, K. Dong, I. Manke, A. Hilger, N. Kardjilov, and J. Banhart, "Investigation of failure mechanisms in silicon based half cells during the first cycle by micro X-ray tomography and radiography," *Journal of Power Sources*, vol. 321, pp. 174–184, Jul. 2016, doi: 10.1016/j.jpowsour.2016.04.126.

[65] H. Wu and Y. Cui, "Designing nanostructured Si anodes for high energy lithium ion batteries," *Nano Today*, vol. 7, no. 5, pp. 414–429, Oct. 2012, doi: 10.1016/j.nantod.2012.08.004.

[66] H. Wu, G. Zheng, N. Liu, T. J. Carney, Y. Yang, and Y. Cui, “Engineering Empty Space between Si Nanoparticles for Lithium-Ion Battery Anodes,” *Nano Lett.*, vol. 12, no. 2, pp. 904–909, Feb. 2012, doi: 10.1021/nl203967r.

[67] C. R. Birkl, M. R. Roberts, E. McTurk, P. G. Bruce, and D. A. Howey, “Degradation diagnostics for lithium ion cells,” *Journal of Power Sources*, vol. 341, pp. 373–386, Feb. 2017, doi: 10.1016/j.jpowsour.2016.12.011.

[68] M. Dubarry, C. Truchot, and B. Y. Liaw, “Cell degradation in commercial LiFePO4 cells with high-power and high-energy designs,” *Journal of Power Sources*, vol. 258, pp. 408–419, Jul. 2014, doi: 10.1016/j.jpowsour.2014.02.052.

[69] K. Higa, H. Zhao, D. Y. Parkinson, H. Barnard, M. Ling, G. Liu, and V. Srinivasan, “Electrode Slurry Particle Density Mapping Using X-ray Radiography,” *J. Electrochem. Soc.*, vol. 164, no. 2, p. A380, Jan. 2017, doi: 10.1149/2.1171702jes.

[70] G. Lenze, H. Bockholt, C. Schilcher, L. Froböse, D. Jansen, U. Krewer, and A. Kwade, “Impacts of Variations in Manufacturing Parameters on Performance of Lithium-Ion-Batteries,” *J. Electrochem. Soc.*, vol. 165, no. 2, pp. A314–A322, Jan. 2018, doi: p.

[71] H. Dreger, W. Haselrieder, and A. Kwade, “Influence of dispersing by extrusion and calendering on the performance of lithium-ion battery electrodes,” *Journal of Energy Storage*, vol. 21, pp. 231–240, Feb. 2019, doi: 10.1016/j.est.2018.11.028.

[72] B. Kenney, K. Darcovich, D. D. MacNeil, and I. J. Davidson, “Modelling the impact of variations in electrode manufacturing on lithium-ion battery modules,” *Journal of Power Sources*, vol. 213, pp. 391–401, Sep. 2012, doi: 10.1016/j.jpowsour.2012.03.065.

[73] O. Rynne, M. Dubarry, C. Molson, E. Nicolas, D. Lepage, A. Prébé, D. Aymé-Perrot, D. Rochefort, and M. Dollé, “Exploiting Materials to Their Full Potential, a Li-Ion Battery Electrode Formulation Optimization Study,” *ACS Appl. Energy Mater.*, vol. 3, no. 3, pp. 2935–2948, Mar. 2020, doi: 10.1021/acsaem.0c00015.

[74] L. Mauler, F. Duffner, and J. Leker, “Economies of scale in battery cell manufacturing: The impact of material and process innovations,” *Applied Energy*, vol. 286, p. 116499, Mar. 2021, doi: 10.1016/j.apenergy.2021.116499.

[75] W. Haselrieder, S. Ivanov, D. K. Christen, H. Bockholt, and A. Kwade, "Impact of the Calendering Process on the Interfacial Structure and the Related Electrochemical Performance of Secondary Lithium-Ion Batteries," *ECS Transactions*, vol. 50, no. 26, pp. 59–70, Apr. 2013, doi: 10.1149/05026.0059ecst.

[76] A. C. Ngandjong, T. Lombardo, E. N. Primo, M. Chouchane, A. Shodiev, O. Arcelus, and A. A. Franco, "Investigating electrode calendering and its impact on electrochemical performance by means of a new discrete element method model: Towards a digital twin of Li-Ion battery manufacturing," *Journal of Power Sources*, vol. 485, p. 229320, Feb. 2021, doi: 10.1016/j.jpowsour.2020.229320.

[77] H. Kang, C. Lim, T. Li, Y. Fu, B. Yan, N. Houston, V. De Andrade, F. De Carlo, and L. Zhu, "Geometric and Electrochemical Characteristics of LiNi1/3Mn1/3Co1/3O2 Electrode with Different Calendering Conditions," *Electrochimica Acta*, vol. 232, pp. 431–438, Apr. 2017, doi: 10.1016/j.electacta.2017.02.151.

[78] D. Schmidt, M. Kamlah, and V. Knoblauch, "Highly densified NCM-cathodes for high energy Li-ion batteries: Microstructural evolution during densification and its influence on the performance of the electrodes," *Journal of Energy Storage*, vol. 17, pp. 213–223, Jun. 2018, doi: 10.1016/j.est.2018.03.002.

[79] S. Santhanagopalan and R. E. White, "Quantifying Cell-to-Cell Variations in Lithium Ion Batteries," *International Journal of Electrochemistry*, vol. 2012, p. e395838, Jan. 2012, doi: 10.1155/2012/395838.

[80] D. Shin, M. Poncino, E. Macii, and N. Chang, "A Statistical Model-Based Cell-to-Cell Variability Management of Li-ion Battery Pack," *IEEE Transactions on Computer-Aided Design of Integrated Circuits and Systems*, vol. 34, no. 2, pp. 252–265, Feb. 2015, doi: 10.1109/TCAD.2014.2384506.

[81] A. Rucci, A. C. Ngandjong, E. N. Primo, M. Maiza, and A. A. Franco, "Tracking variabilities in the simulation of Lithium Ion Battery electrode fabrication and its impact on electrochemical performance," *Electrochimica Acta*, vol. 312, pp. 168–178, Jul. 2019, doi: 10.1016/j.electacta.2019.04.110.

[82] M. Duquesnoy, T. Lombardo, M. Chouchane, E. N. Primo, and A. A. Franco, "Data-driven assessment of electrode calendering process by combining experimental results, in silico mesostructures generation and machine

learning," *Journal of Power Sources*, vol. 480, p. 229103, Dec. 2020, doi: 10.1016/j.jpowsour.2020.229103.

[83] R. Leithoff, A. Fröhlich, and K. Dröder, "Investigation of the Influence of Deposition Accuracy of Electrodes on the Electrochemical Properties of Lithium-Ion Batteries," *Energy Technology*, vol. 8, no. 2, p. 1900129, 2020, doi: 10.1002/ente.201900129.

[84] W. A. Paxton, Z. Zhong, and T. Tsakalakos, "Tracking inhomogeneity in high-capacity lithium iron phosphate batteries," *Journal of Power Sources*, vol. 275, pp. 429–434, Feb. 2015, doi: 10.1016/j.jpowsour.2014.11.035.

[85] R. F. Ziesche, T. Arlt, D. P. Finegan, T. M. M. Heenan, A. Tengattini, D. Baum, N. Kardjilov, H. Markötter, I. Manke, W. Kockelmann, D. J. L. Brett, and P. R. Shearing, "4D imaging of lithium-batteries using correlative neutron and X-ray tomography with a virtual unrolling technique," *Nature Communications*, vol. 11, no. 1, pp. 1–11, Feb. 2020, doi: 10.1038/s41467-019-13943-3.

[86] T. Baumhöfer, M. Brühl, S. Rothgang, and D. U. Sauer, "Production caused variation in capacity aging trend and correlation to initial cell performance," *Journal of Power Sources*, vol. 247, pp. 332–338, Feb. 2014, doi: 10.1016/j.jpowsour.2013.08.108.

[87] S. Miyatake, Y. Susuki, T. Hikihara, S. Itoh, and K. Tanaka, "Discharge characteristics of multicell lithium-ion battery with nonuniform cells," *Journal of Power Sources*, vol. 241, pp. 736–743, Nov. 2013, doi: 10.1016/j.jpowsour.2013.05.179.

[88] R. Gogoana, M. B. Pinson, M. Z. Bazant, and S. E. Sarma, "Internal resistance matching for parallel-connected lithium-ion cells and impacts on battery pack cycle life," *Journal of Power Sources*, vol. 252, pp. 8–13, Apr. 2014, doi: 10.1016/j.jpowsour.2013.11.101.

[89] M. Dubarry, C. Truchot, M. Cugnet, B. Y. Liaw, K. Gering, S. Sazhin, D. Jamison, and C. Michelbacher, "Evaluation of commercial lithium-ion cells based on composite positive electrode for plug-in hybrid electric vehicle applications. Part I: Initial characterizations," *Journal of Power Sources*, vol. 196, no. 23, pp. 10328–10335, Dec. 2011, doi: 10.1016/j.jpowsour.2011.08.077.

[90] S. Paul, C. Diegelmann, H. Kabza, and W. Tillmetz, "Analysis of ageing inhomogeneities in lithium-ion battery systems," *Journal of Power Sources*, vol. 239, pp. 642–650, Oct. 2013, doi: 10.1016/j.jpowsour.2013.01.068.

[91] K. Rumpf, M. Naumann, and A. Jossen, “Experimental investigation of parametric cell-to-cell variation and correlation based on 1100 commercial lithium-ion cells,” *Journal of Energy Storage*, vol. 14, pp. 224–243, Dec. 2017, doi: 10.1016/j.est.2017.09.010.

[92] F. An, L. Chen, J. Huang, J. Zhang, and P. Li, “Rate dependence of cell-to-cell variations of lithium-ion cells,” *Scientific Reports*, vol. 6, no. 1, Art. no. 1, Oct. 2016, doi: 10.1038/srep35051.

[93] M. Dubarry, N. Vuillaume, and B. Y. Liaw, “Origins and accommodation of cell variations in Li-ion battery pack modeling,” *International Journal of Energy Research*, vol. 34, no. 2, pp. 216–231, 2010, doi: https://doi.org/10.1002/er.1668.

[94] A. Devie and M. Dubarry, “Durability and Reliability of Electric Vehicle Batteries under Electric Utility Grid Operations. Part 1: Cell-to-Cell Variations and Preliminary Testing,” *Batteries*, vol. 2, no. 3, Art. no. 3, Sep. 2016, doi: 10.3390/batteries2030028.

[95] L. Xie, D. Ren, L. Wang, Z. Chen, G. Tian, K. Amine, and X. He, “A Facile Approach to High Precision Detection of Cell-to-Cell Variation for Li-ion Batteries,” *Scientific Reports*, vol. 10, no. 1, Art. no. 1, Apr. 2020, doi: 10.1038/s41598-020-64174-2.

[96] R. Carter, E. J. Klein, R. W. Atkinson, and C. T. Love, “Mechanical collapse as primary degradation mode in mandrel-free 18650 Li-ion cells operated at 0 °C,” *Journal of Power Sources*, vol. 437, p. 226820, Oct. 2019, doi: 10.1016/j.jpowsour.2019.226820.

[97] A. Pfrang, A. Kersys, A. Kriston, D. U. Sauer, C. Rahe, S. Käbitz, and E. Figgemeier, “Long-term cycling induced jelly roll deformation in commercial 18650 cells,” *Journal of Power Sources*, vol. 392, pp. 168–175, Jul. 2018, doi: 10.1016/j.jpowsour.2018.03.065.

[98] L. K. Willenberg, P. Dechent, G. Fuchs, M. Teuber, M. Eckert, M. Graff, N. Kürten, D. U. Sauer, and E. Figgemeier, “The development of jelly roll deformation in 18650 lithium-ion batteries at low state of charge,” *J. Electrochem. Soc.*, 2020, doi: 10.1149/1945-7111/aba96d.

[99] J. Cannarella and C. B. Arnold, “The Effects of Defects on Localized Plating in Lithium-Ion Batteries,” *J. Electrochem. Soc.*, vol. 162, no. 7, p. A1365, Apr. 2015, doi: 10.1149/2.1051507jes.

[100] J. Cannarella and C. B. Arnold, “Ion transport restriction in mechanically strained separator membranes,” *Journal of Power Sources*, vol. 226, pp. 149–155, Mar. 2013, doi: 10.1016/j.jpowsour.2012.10.093.

[101] M. J. Mühlbauer, D. Petz, V. Baran, O. Dolotko, M. Hofmann, R. Kostecki, and A. Senyshyn, “Inhomogeneous distribution of lithium and electrolyte in aged Li-ion cylindrical cells,” *Journal of Power Sources*, vol. 475, p. 228690, Nov. 2020, doi: 10.1016/j.jpowsour.2020.228690.

[102] D. Petz, M. J. Mühlbauer, A. Schökel, K. Achterhold, F. Pfeiffer, T. Pirling, M. Hofmann, and A. Senyshyn, “Heterogeneity of Graphite Lithiation in State-of-the-Art Cylinder-Type Li-Ion Cells,” *Batteries & Supercaps*, vol. 4, no. 2, pp. 327–335, 2021, doi: https://doi.org/10.1002/batt.202000178.

[103] M. J. Mühlbauer, O. Dolotko, M. Hofmann, H. Ehrenberg, and A. Senyshyn, “Effect of fatigue/ageing on the lithium distribution in cylinder-type Li-ion batteries,” *Journal of Power Sources*, vol. 348, pp. 145–149, Apr. 2017, doi: 10.1016/j.jpowsour.2017.02.077.

[104] M. J. Loveridge, G. Remy, N. Kourra, R. Genieser, A. Barai, M. J. Lain, Y. Guo, M. Amor-Segan, M. A. Williams, T. Amietszajew, M. Ellis, R. Bhagat, and D. Greenwood, “Looking Deeper into the Galaxy (Note 7),” *Batteries*, vol. 4, no. 1, Art. no. 1, Mar. 2018, doi: 10.3390/batteries4010003.

[105] “[Infographic] Galaxy Note7: What We Discovered.” https://news.samsung.com/global/infographic-galaxy-note7-what-we-discovered (accessed Feb. 26, 2021).

[106] D. Werner, S. Paarmann, A. Wiebelt, and T. Wetzel, “Inhomogeneous Temperature Distribution Affecting the Cyclic Aging of Li-Ion Cells. Part II: Analysis and Correlation,” *Batteries*, vol. 6, no. 1, Art. no. 1, Mar. 2020, doi: 10.3390/batteries6010012.

[107] P. J. Osswald, S. V. Erhard, A. Rheinfeld, B. Rieger, H. E. Hoster, and A. Jossen, “Temperature dependency of state of charge inhomogeneities and their equalization in cylindrical lithium-ion cells,” *Journal of Power Sources*, vol. 329, pp. 546–552, Oct. 2016, doi: 10.1016/j.jpowsour.2016.08.120.

[108] T. Grandjean, A. Barai, E. Hosseinzadeh, Y. Guo, A. McGordon, and J. Marco, “Large format lithium ion pouch cell full thermal characterisation for improved electric vehicle thermal management,” *Journal of Power Sources*, vol. 359, pp. 215–225, Aug. 2017, doi: 10.1016/j.jpowsour.2017.05.016.

[109] R. Carter, T. A. Kingston, R. W. Atkinson, M. Parmananda, M. Dubarry, C. Fear, P. P. Mukherjee, and C. T. Love, "Directionality of thermal gradients in lithium-ion batteries dictates diverging degradation modes," *Cell Reports Physical Science*, p. 100351, Feb. 2021, doi: 10.1016/j.xcrp.2021.100351.

[110] S. Paarmann, L. Cloos, J. Technau, and T. Wetzel, "Measurement of the Temperature Influence on the Current Distribution in Li-Ion Batteries," *Energy Technol.*, p. ente.202000862, Dec. 2020, doi: 10.1002/ente.202000862.

[111] A. Moretti, D. V. Carvalho, N. Ehteshami, E. Paillard, W. Porcher, D. Brun-Buisson, J.-B. Ducros, I. de Meatza, A. Eguia-Barrio, K. Trad, and S. Passerini, "A Post-Mortem Study of Stacked 16 Ah Graphite//LiFePO4 Pouch Cells Cycled at 5 °C," *Batteries*, vol. 5, no. 2, Art. no. 2, Jun. 2019, doi: 10.3390/batteries5020045.

[112] J. B. Robinson, M. Maier, G. Alster, T. Compton, D. J. L. Brett, and P. R. Shearing, "Spatially resolved ultrasound diagnostics of Li-ion battery electrodes," *Phys. Chem. Chem. Phys.*, vol. 21, no. 12, pp. 6354–6361, Mar. 2019, doi: 10.1039/C8CP07098A.

[113] B. Rowden and N. Garcia-Araez, "A review of gas evolution in lithium ion batteries," *Energy Reports*, vol. 6, pp. 10–18, May 2020, doi: 10.1016/j.egyr.2020.02.022.

[114] P. Michalowski, A. Gräfenstein, M. Knipper, T. Plaggenborg, J. Schwenzel, and J. Parisi, "Examining Inhomogeneous Degradation of Graphite/Carbon Black Composite Electrodes in Li-Ion Batteries by Lock-In Thermography," *J. Electrochem. Soc.*, vol. 164, no. 9, p. A2251, Aug. 2017, doi: 10.1149/2.0281712jes.

[115] A. Devie, M. Dubarry, and B. Y. Liaw, "Overcharge Study in Li4Ti5O12 Based Lithium-Ion Pouch Cell: I. Quantitative Diagnosis of Degradation Modes," *J. Electrochem. Soc.*, vol. 162, no. 6, p. A1033, Mar. 2015, doi: 10.1149/2.0941506jes.

[116] A. Devie, M. Dubarry, H.-P. Wu, T.-H. Wu, and B. Y. Liaw, "Overcharge Study in Li4Ti5O12 Based Lithium-Ion Pouch Cell," *J. Electrochem. Soc.*, vol. 163, no. 13, p. A2611, Sep. 2016, doi: 10.1149/2.0491613jes.

[117] A. Devie, G. Baure, and M. Dubarry, “Intrinsic Variability in the Degradation of a Batch of Commercial 18650 Lithium-Ion Cells,” *Energies*, vol. 11, no. 5, Art. no. 5, May 2018, doi: 10.3390/en11051031.

[118] W. Li, N. Sengupta, P. Dechent, D. Howey, A. Annaswamy, and D. U. Sauer, “Online capacity estimation of lithium-ion batteries with deep long short-term memory networks,” *Journal of Power Sources*, vol. 482, p. 228863, Jan. 2021, doi: 10.1016/j.jpowsour.2020.228863.

[119] C. Pastor-Fernández, T. Bruen, W. D. Widanage, M. A. Gama-Valdez, and J. Marco, “A Study of Cell-to-Cell Interactions and Degradation in Parallel Strings: Implications for the Battery Management System,” *Journal of Power Sources*, vol. 329, pp. 574–585, Oct. 2016, doi: 10.1016/j.jpowsour.2016.07.121.

[120] M. J. Brand, P. A. Schmidt, M. F. Zaeh, and A. Jossen, “Welding techniques for battery cells and resulting electrical contact resistances,” *Journal of Energy Storage*, vol. 1, pp. 7–14, Jun. 2015, doi: 10.1016/j.est.2015.04.001.

[121] J. Taylor, A. Barai, T. R. Ashwin, Y. Guo, M. Amor-Segan, and J. Marco, “An insight into the errors and uncertainty of the lithium-ion battery characterisation experiments,” *Journal of Energy Storage*, vol. 24, p. 100761, Aug. 2019, doi: 10.1016/j.est.2019.100761.

[122] T. Bruen and J. Marco, “Modelling and experimental evaluation of parallel connected lithium ion cells for an electric vehicle battery system,” *Journal of Power Sources*, vol. 310, pp. 91–101, Apr. 2016, doi: 10.1016/j.jpowsour.2016.01.001.

[123] K. Rumpf, A. Rheinfeld, M. Schindler, J. Keil, T. Schua, and A. Jossen, “Influence of Cell-to-Cell Variations on the Inhomogeneity of Lithium-Ion Battery Modules,” *J. Electrochem. Soc.*, vol. 165, no. 11, pp. A2587–A2607, Jan. 2018, doi: 10.1149/2.0111811jes.

[124] L. Wang, Y. Cheng, and X. Zhao, “Influence of connecting plate resistance upon LiFePO4 battery performance,” *Applied Energy*, vol. 147, pp. 353–360, Jun. 2015, doi: 10.1016/j.apenergy.2015.03.016.

[125] G. J. Offer, V. Yufit, D. A. Howey, B. Wu, and N. P. Brandon, “Module design and fault diagnosis in electric vehicle batteries,” *Journal of Power Sources*, vol. 206, pp. 383–392, May 2012, doi: 10.1016/j.jpowsour.2012.01.087.

[126] M. Naguib, P. Kollmeyer, and A. Emadi, “Lithium-Ion Battery Pack Robust State of Charge Estimation, Cell Inconsistency, and Balancing: Review,” *IEEE Access*, vol. 9, pp. 50570–50582, 2021, doi: 10.1109/ACCESS.2021.3068776.

[127] M. Dubarry, N. Vuillaume, and B. Y. Liaw, “From single cell model to battery pack simulation for Li-ion batteries,” *Journal of Power Sources*, vol. 186, no. 2, pp. 500–507, Jan. 2009, doi: 10.1016/j.jpowsour.2008.10.051.

[128] M. Dubarry, C. Pastor-Fernández, G. Baure, T. F. Yu, W. D. Widanage, and J. Marco, “Battery energy storage system modeling: Investigation of intrinsic cell-to-cell variations,” *Journal of Energy Storage*, vol. 23, pp. 19–28, Jun. 2019, doi: 10.1016/j.est.2019.02.016.

[129] F. Feng, X. Hu, L. Hu, F. Hu, Y. Li, and L. Zhang, “Propagation mechanisms and diagnosis of parameter inconsistency within Li-Ion battery packs,” *Renewable and Sustainable Energy Reviews*, vol. 112, pp. 102–113, Sep. 2019, doi: 10.1016/j.rser.2019.05.042.

[130] X. Liu, W. Ai, M. Naylor Marlow, Y. Patel, and B. Wu, “The effect of cell-to-cell variations and thermal gradients on the performance and degradation of lithium-ion battery packs,” *Applied Energy*, vol. 248, pp. 489–499, Aug. 2019, doi: 10.1016/j.apenergy.2019.04.108.

[131] S. Neupert and J. Kowal, “Inhomogeneities in Battery Packs,” *World Electric Vehicle Journal*, vol. 9, no. 2, Art. no. 2, Aug. 2018, doi: 10.3390/wevj9020020.

[132] B. Wu, V. Yufit, M. Marinescu, G. J. Offer, R. F. Martinez-Botas, and N. P. Brandon, “Coupled thermal–electrochemical modelling of uneven heat generation in lithium-ion battery packs,” *Journal of Power Sources*, vol. 243, pp. 544–554, Dec. 2013, doi: 10.1016/j.jpowsour.2013.05.164.

[133] M. Dubarry, A. Devie, K. Stein, M. Tun, M. Matsuura, and R. Rocheleau, “Battery Energy Storage System battery durability and reliability under electric utility grid operations: Analysis of 3 years of real usage,” *Journal of Power Sources*, vol. 338, pp. 65–73, Jan. 2017, doi: 10.1016/j.jpowsour.2016.11.034.

[134] N. Yang, X. Zhang, B. Shang, and G. Li, “Unbalanced discharging and aging due to temperature differences among the cells in a lithium-ion battery pack with parallel combination,” *Journal of Power Sources*, vol. 306, pp. 733–741, Feb. 2016, doi: 10.1016/j.jpowsour.2015.12.079.

[135] K.-C. Chiu, C.-H. Lin, S.-F. Yeh, Y.-H. Lin, C.-S. Huang, and K.-C. Chen, "Cycle life analysis of series connected lithium-ion batteries with temperature difference," *Journal of Power Sources*, vol. 263, pp. 75–84, Oct. 2014, doi: 10.1016/j.jpowsour.2014.04.034.

[136] F. An, J. Huang, C. Wang, Z. Li, J. Zhang, S. Wang, and P. Li, "Cell sorting for parallel lithium-ion battery systems: Evaluation based on an electric circuit model," *Journal of Energy Storage*, vol. 6, pp. 195–203, May 2016, doi: 10.1016/j.est.2016.04.007.

[137] C. Lyu, Y. Song, L. Wang, J. Li, B. Zhang, and E. Liu, "A new method for lithium-ion battery uniformity sorting based on internal criteria," *Journal of Energy Storage*, vol. 25, p. 100885, Oct. 2019, doi: 10.1016/j.est.2019.100885.

[138] T. Wang, K. J. Tseng, J. Zhao, and Z. Wei, "Thermal investigation of lithium-ion battery module with different cell arrangement structures and forced air-cooling strategies," *Applied Energy*, vol. 134, pp. 229–238, Dec. 2014, doi: 10.1016/j.apenergy.2014.08.013.

[139] K. L. Gering, S. V. Sazhin, D. K. Jamison, C. J. Michelbacher, B. Y. Liaw, M. Dubarry, and M. Cugnet, "Investigation of path dependence in commercial lithium-ion cells chosen for plug-in hybrid vehicle duty cycle protocols," *Journal of Power Sources*, vol. 196, no. 7, pp. 3395–3403, Apr. 2011, doi: 10.1016/j.jpowsour.2010.05.058.

[140] J. Keil, N. Paul, V. Baran, P. Keil, R. Gilles, and A. Jossen, "Linear and Nonlinear Aging of Lithium-Ion Cells Investigated by Electrochemical Analysis and In-Situ Neutron Diffraction," *J. Electrochem. Soc.*, vol. 166, no. 16, p. A3908, Nov. 2019, doi: 10.1149/2.1271915jes.

[141] T. Raj, A. A. Wang, C. W. Monroe, and D. A. Howey, "Investigation of Path-Dependent Degradation in Lithium-Ion Batteries**," *Batteries & Supercaps*, vol. 3, no. 12, pp. 1377–1385, 2020, doi: https://doi.org/10.1002/batt.202000160.

[142] M. Simolka, J.-F. Heger, H. Kaess, I. Biswas, and K. A. Friedrich, "Influence of cycling profile, depth of discharge and temperature on commercial LFP/C cell ageing: post-mortem material analysis of structure, morphology and chemical composition," *J Appl Electrochem*, vol. 50, no. 11, pp. 1101–1117, Nov. 2020, doi: 10.1007/s10800-020-01465-6.

[143] D. Anseán, M. Dubarry, A. Devie, B. Y. Liaw, V. M. García, J. C. Viera, and M. González, "Operando lithium plating quantification and early

detection of a commercial LiFePO4 cell cycled under dynamic driving schedule," *Journal of Power Sources*, vol. 356, pp. 36–46, Jul. 2017, doi: 10.1016/j.jpowsour.2017.04.072.

[144] E. Martinez-Laserna, E. Sarasketa-Zabala, D.- Stroe, M. Swierczynski, A. Warnecke, J. M. Timmermans, S. Goutam, and P. Rodriguez, "Evaluation of lithium-ion battery second life performance and degradation," in *2016 IEEE Energy Conversion Congress and Exposition (ECCE)*, Sep. 2016, pp. 1–7. doi: 10.1109/ECCE.2016.7855090.

[145] E. Hossain, D. Murtaugh, J. Mody, H. M. R. Faruque, M. S. H. Sunny, and N. Mohammad, "A Comprehensive Review on Second-Life Batteries: Current State, Manufacturing Considerations, Applications, Impacts, Barriers Potential Solutions, Business Strategies, and Policies," *IEEE Access*, vol. 7, pp. 73215–73252, 2019, doi: 10.1109/ACCESS.2019.2917859.

[146] M. P. B. Glazer, J. S. Okasinski, J. D. Almer, and Y. Ren, "High-energy x-ray scattering studies of battery materials," *MRS Bulletin*, vol. 41, no. 6, pp. 460–465, Jun. 2016, doi: 10.1557/mrs.2016.96.

[147] S. Müller, P. Pietsch, B.-E. Brandt, P. Baade, V. D. Andrade, F. D. Carlo, and V. Wood, "Quantification and modeling of mechanical degradation in lithium-ion batteries based on nanoscale imaging," *Nature Communications*, vol. 9, no. 1, p. 2340, Jun. 2018, doi: 10.1038/s41467-018-04477-1.

[148] W. A. Paxton, Z. Zhong, and T. Tsakalakos, "Tracking inhomogeneity in high-capacity lithium iron phosphate batteries," *Journal of Power Sources*, vol. 275, pp. 429–434, Feb. 2015, doi: 10.1016/j.jpowsour.2014.11.035.

[149] D. Petz, M. J. Mühlbauer, V. Baran, M. Frost, A. Schökel, C. Paulmann, Y. Chen, D. Garcés, and A. Senyshyn, "Lithium heterogeneities in cylinder-type Li-ion batteries – fatigue induced by cycling," *Journal of Power Sources*, vol. 448, p. 227466, Feb. 2020, doi: 10.1016/j.jpowsour.2019.227466.

[150] L. Cai, K. An, Z. Feng, C. Liang, and S. J. Harris, "In-situ observation of inhomogeneous degradation in large format Li-ion cells by neutron diffraction," *Journal of Power Sources*, vol. 236, pp. 163–168, Aug. 2013, doi: 10.1016/j.jpowsour.2013.02.066.

[151] A. Senyshyn, M. J. Mühlbauer, O. Dolotko, M. Hofmann, and H. Ehrenberg, “Homogeneity of lithium distribution in cylinder-type Li-ion batteries,” *Scientific Reports*, vol. 5, p. 18380, Dec. 2015, doi: 10.1038/srep18380.

[152] N. Paul, J. Wandt, S. Seidlmayer, S. Schebesta, M. J. Mühlbauer, O. Dolotko, H. A. Gasteiger, and R. Gilles, “Aging behavior of lithium iron phosphate based 18650-type cells studied by in situ neutron diffraction,” *Journal of Power Sources*, vol. 345, pp. 85–96, Mar. 2017, doi: 10.1016/j.jpowsour.2017.01.134.

[153] N. Paul, J. Keil, F. M. Kindermann, S. Schebesta, O. Dolotko, M. J. Mühlbauer, L. Kraft, S. V. Erhard, A. Jossen, and R. Gilles, “Aging in 18650-type Li-ion cells examined with neutron diffraction, electrochemical analysis and physico-chemical modeling,” *Journal of Energy Storage*, vol. 17, pp. 383–394, Jun. 2018, doi: 10.1016/j.est.2018.03.016.

[154] V. Zinth, C. von Lüders, J. Wilhelm, S. V. Erhard, M. Hofmann, S. Seidlmayer, J. Rebelo-Kornmeier, W. Gan, A. Jossen, and R. Gilles, “Inhomogeneity and relaxation phenomena in the graphite anode of a lithium-ion battery probed by in situ neutron diffraction,” *Journal of Power Sources*, vol. 361, pp. 54–60, Sep. 2017, doi: 10.1016/j.jpowsour.2017.06.060.

[155] T. Waldmann, A. Iturrondobeitia, M. Kasper, N. Ghanbari, F. Aguesse, E. Bekaert, L. Daniel, S. Genies, I. J. Gordon, M. W. Löble, E. D. Vito, and M. Wohlfahrt-Mehrens, “Review—Post-Mortem Analysis of Aged Lithium-Ion Batteries: Disassembly Methodology and Physico-Chemical Analysis Techniques,” *J. Electrochem. Soc.*, vol. 163, no. 10, pp. A2149–A2164, Jan. 2016, doi: 10.1149/2.1211609jes.

[156] J. Lu, T. Wu, and K. Amine, “State-of-the-art characterization techniques for advanced lithium-ion batteries,” *Nature Energy*, vol. 2, no. 3, Art. no. 3, Mar. 2017, doi: 10.1038/nenergy.2017.11.

[157] P. P. R. M. L. Harks, F. M. Mulder, and P. H. L. Notten, “In situ methods for Li-ion battery research: A review of recent developments,” *Journal of Power Sources*, vol. 288, pp. 92–105, Aug. 2015, doi: 10.1016/j.jpowsour.2015.04.084.

[158] J. Fleming, T. Amietszajew, J. Charmet, A. J. Roberts, D. Greenwood, and R. Bhagat, “The design and impact of in-situ and operando thermal

sensing for smart energy storage," *Journal of Energy Storage*, vol. 22, pp. 36–43, 2019, doi: 10.1016/j.est.2019.01.026.

[159] E. McTurk, C. R. Birkl, M. R. Roberts, D. A. Howey, and P. G. Bruce, "Minimally Invasive Insertion of Reference Electrodes into Commercial Lithium-Ion Pouch Cells," *ECS Electrochem. Lett.*, vol. 4, no. 12, p. A145, Jan. 2015, doi: 10.1149/2.0081512eel.

[160] H. Wang and J. F. Whitacre, "Inhomogeneous aging of cathode materials in commercial 18650 lithium ion battery cells," *Journal of Energy Storage*, vol. 35, p. 102244, Mar. 2021, doi: 10.1016/j.est.2021.102244.

[161] A. J. Warnecke, "Degradation Mechanisms in NMC-Based Lithium-Ion Batteries," PhD thesis, RWTH Aachen University, Aachen, Germany, 2017. doi: 10.18154/RWTH-2017-09646.

[162] B. Gyenes, D. A. Stevens, V. L. Chevrier, and J. R. Dahn, "Understanding Anomalous Behavior in Coulombic Efficiency Measurements on Li-Ion Batteries," *J. Electrochem. Soc.*, vol. 162, no. 3, pp. A278–A283, Jan. 2015, doi: 10.1149/2.0191503jes.

[163] D. Juarez-Robles, J. A. Jeevarajan, and P. P. Mukherjee, "Degradation-Safety Analytics in Lithium-Ion Cells: Part I. Aging under Charge/Discharge Cycling," *J. Electrochem. Soc.*, vol. 167, no. 16, p. 160510, Nov. 2020, doi: 10.1149/1945-7111/abc8c0.

[164] F. B. Spingler, M. Naumann, and A. Jossen, "Capacity Recovery Effect in Commercial LiFePO4 / Graphite Cells," *J. Electrochem. Soc.*, vol. 167, no. 4, p. 040526, Mar. 2020, doi: 10.1149/1945-7111/ab7900.

[165] J. C. Burns, D. A. Stevens, and J. R. Dahn, "In-Situ Detection of Lithium Plating Using High Precision Coulometry," *J. Electrochem. Soc.*, vol. 162, no. 6, pp. A959–A964, Jan. 2015, doi: 10.1149/2.0621506jes.

[166] S. Käbitz, "Untersuchung der Alterung von Lithium-Ionen-Batterien mittels Elektroanalytik und elektrochemischer Impedanzspektroskopie," PhD thesis, RWTH Aachen University, Aachen, Germany, 2016.

[167] M. Lewerenz, A. Warnecke, and D. U. Sauer, "Post-mortem analysis on LiFePO4|Graphite cells describing the evolution & composition of covering layer on anode and their impact on cell performance," *Journal of Power Sources*, vol. 369, pp. 122–132, Nov. 2017, doi: 10.1016/j.jpowsour.2017.10.003.

[168] X. Fleury, M. H. Noh, S. Geniès, P. X. Thivel, C. Lefrou, and Y. Bultel, “Fast-charging of Lithium Iron Phosphate battery with ohmic-drop compensation method: Ageing study,” *Journal of Energy Storage*, vol. 16, pp. 21–36, Apr. 2018, doi: 10.1016/j.est.2017.12.015.

[169] A. Pfrang, A. Kersys, A. Kriston, D. U. Sauer, C. Rahe, S. Käbitz, and E. Figgemeier, “Geometrical Inhomogeneities as Cause of Mechanical Failure in Commercial 18650 Lithium Ion Cells,” *J. Electrochem. Soc.*, vol. 166, no. 15, pp. A3745–A3752, 2019, doi: 10.1149/2.0551914jes.

[170] D. Burow, K. Sergeeva, S. Calles, K. Schorb, A. Börger, C. Roth, and P. Heitjans, “Inhomogeneous degradation of graphite anodes in automotive lithium ion batteries under low-temperature pulse cycling conditions,” *Journal of Power Sources*, vol. 307, pp. 806–814, Mar. 2016, doi: 10.1016/j.jpowsour.2016.01.033.

[171] A. Pfrang, A. Kersys, A. Kriston, D. U. Sauer, C. Rahe, S. Käbitz, and E. Figgemeier, “Long-term cycling induced jelly roll deformation in commercial 18650 cells,” *Journal of Power Sources*, vol. 392, pp. 168–175, Jul. 2018, doi: 10.1016/j.jpowsour.2018.03.065.

[172] C. Rahe, S. T. Kelly, M. N. Rad, D. U. Sauer, J. Mayer, and E. Figgemeier, “Nanoscale X-ray imaging of ageing in automotive lithium ion battery cells,” *Journal of Power Sources*, vol. 433, p. 126631, Sep. 2019, doi: 10.1016/j.jpowsour.2019.05.039.

[173] Y. Yang, R. Xu, K. Zhang, S.-J. Lee, L. Mu, P. Liu, C. K. Waters, S. Spence, Z. Xu, C. Wei, D. J. Kautz, Q. Yuan, Y. Dong, Y.-S. Yu, X. Xiao, H.-K. Lee, P. Pianetta, P. Cloetens, J.-S. Lee, K. Zhao, F. Lin, and Y. Liu, “Quantification of Heterogeneous Degradation in Li-Ion Batteries,” *Advanced Energy Materials*, vol. 9, no. 25, p. 1900674, 2019, doi: 10.1002/aenm.201900674.

[174] L. Li and J. Hou, “Capacity detection of electric vehicle lithium-ion batteries based on X-ray computed tomography,” *RSC Adv.*, vol. 8, no. 45, pp. 25325–25333, Jul. 2018, doi: 10.1039/C8RA04516J.

[175] A. J. Ilott, M. Mohammadi, C. M. Schauerman, M. J. Ganter, and A. Jerschow, “Rechargeable lithium-ion cell state of charge and defect detection by in-situ inside-out magnetic resonance imaging,” *Nature Communications*, vol. 9, no. 1, Art. no. 1, May 2018, doi: 10.1038/s41467-018-04192-x.

[176] S. A. Krachkovskiy, J. M. Foster, J. D. Bazak, B. J. Balcom, and G. R. Goward, “Operando Mapping of Li Concentration Profiles and Phase

Transformations in Graphite Electrodes by Magnetic Resonance Imaging and Nuclear Magnetic Resonance Spectroscopy," *J. Phys. Chem. C*, vol. 122, no. 38, pp. 21784–21791, Sep. 2018, doi: 10.1021/acs.jpcc.8b06563.

[177] S. Wiemers-Meyer, M. Winter, and S. Nowak, "Mechanistic insights into lithium ion battery electrolyte degradation – a quantitative NMR study," *Phys. Chem. Chem. Phys.*, vol. 18, no. 38, pp. 26595–26601, Sep. 2016, doi: 10.1039/C6CP05276B.

[178] L. P. Bauermann, L. V. Mesquita, C. Bischoff, M. Drews, O. Fitz, A. Heuer, and D. Biro, "Scanning acoustic microscopy as a non-destructive imaging tool to localize defects inside battery cells," *Journal of Power Sources Advances*, vol. 6, p. 100035, Dec. 2020, doi: 10.1016/j.powera.2020.100035.

[179] M. Dubarry and G. Baure, "Perspective on Commercial Li-ion Battery Testing, Best Practices for Simple and Effective Protocols," *Electronics*, vol. 9, no. 1, p. 152, Jan. 2020, doi: 10.3390/electronics9010152.

[180] S. J. Harris, D. J. Harris, and C. Li, "Failure statistics for commercial lithium ion batteries: A study of 24 pouch cells," *Journal of Power Sources*, vol. 342, pp. 589–597, Feb. 2017, doi: 10.1016/j.jpowsour.2016.12.083.

[181] T. Baumhöfer, *Statistische Betrachtung experimenteller Alterungsuntersuchungen an Lithium-Ionen Batterien*, 1st ed. Aachen: Shaker, PhD thesis, RWTH Aachen University, 2015.

[182] A. Marongiu, F. G. W. Nußbaum, W. Waag, M. Garmendia, and D. U. Sauer, "Comprehensive study of the influence of aging on the hysteresis behavior of a lithium iron phosphate cathode-based lithium ion battery – An experimental investigation of the hysteresis," *Applied Energy*, vol. 171, pp. 629–645, Jun. 2016, doi: 10.1016/j.apenergy.2016.02.086.

[183] H. Witzenhausen, "Elektrische Batteriespeichermodelle: Modellbildung, Parameteridentifikation und Modellreduktion," PhD thesis, RWTH Aachen University, Aachen, Germany, 2017. doi: 10.18154/RWTH-2017-03437.

[184] P. Shafiei Sabet, G. Stahl, and D. U. Sauer, "Non-invasive investigation of predominant processes in the impedance spectra of high energy lithium-ion batteries with nickel–cobalt–aluminum cathodes," *Journal of Power Sources*, vol. 472, p. 228189, Oct. 2020, doi: 10.1016/j.jpowsour.2020.228189.

[185] H. Zappen, F. Ringbeck, and D. U. Sauer, “Application of Time-Resolved Multi-Sine Impedance Spectroscopy for Lithium-Ion Battery Characterization,” *Batteries*, vol. 4, no. 4, p. 64, Dec. 2018, doi: 10.3390/batteries4040064.

[186] W. Waag, S. Käbitz, and D. U. Sauer, “Experimental investigation of the lithium-ion battery impedance characteristic at various conditions and aging states and its influence on the application,” *Applied Energy*, vol. 102, pp. 885–897, Feb. 2013, doi: 10.1016/j.apenergy.2012.09.030.

[187] I. Bloom, A. N. Jansen, D. P. Abraham, J. Knuth, S. A. Jones, V. S. Battaglia, and G. L. Henriksen, “Differential voltage analyses of high-power, lithium-ion cells 1. Technique and application,” *Journal of Power Sources*, vol. 139, no. 1–2, pp. 295–303, Jan. 2005, doi: 10.1016/j.jpowsour.2004.07.021.

[188] M. Dubarry and B. Y. Liaw, “Identify capacity fading mechanism in a commercial LiFePO4 cell,” *Journal of Power Sources*, vol. 194, no. 1, pp. 541–549, Oct. 2009, doi: 10.1016/j.jpowsour.2009.05.036.

[189] M. Lewerenz, A. Marongiu, A. Warnecke, and D. U. Sauer, “Differential voltage analysis as a tool for analyzing inhomogeneous aging: A case study for LiFePO4|Graphite cylindrical cells,” *Journal of Power Sources*, vol. 368, pp. 57–67, Nov. 2017, doi: 10.1016/j.jpowsour.2017.09.059.

[190] Y. Jiang, J. Jiang, C. Zhang, W. Zhang, Y. Gao, and Q. Guo, “Recognition of battery aging variations for LiFePO4 batteries in 2nd use applications combining incremental capacity analysis and statistical approaches,” *Journal of Power Sources*, vol. 360, pp. 180–188, Aug. 2017, doi: 10.1016/j.jpowsour.2017.06.007.

[191] T. R. Tanim, M. G. Shirk, R. L. Bewley, E. J. Dufek, and B. Y. Liaw, “Fast charge implications: Pack and cell analysis and comparison,” *Journal of Power Sources*, vol. 381, pp. 56–65, Mar. 2018, doi: 10.1016/j.jpowsour.2018.01.091.

[192] L. Chang, C. Wang, C. Zhang, L. Xiao, N. Cui, H. Li, and J. Qiu, “A novel fast capacity estimation method based on current curves of parallel-connected cells for retired lithium-ion batteries in second-use applications,” *Journal of Power Sources*, vol. 459, p. 227901, May 2020, doi: 10.1016/j.jpowsour.2020.227901.

[193] A. Krupp, E. Ferg, F. Schuldt, K. Derendorf, and C. Agert, “Incremental Capacity Analysis as a State of Health Estimation Method for Lithium-Ion

Battery Modules with Series-Connected Cells," *Batteries*, vol. 7, no. 1, Art. no. 1, Mar. 2021, doi: 10.3390/batteries7010002.

[194] M. Lewerenz, A. Warnecke, and D. U. Sauer, "Introduction of capacity difference analysis (CDA) for analyzing lateral lithium-ion flow to determine the state of covering layer evolution," *Journal of Power Sources*, vol. 354, pp. 157–166, Jun. 2017, doi: 10.1016/j.jpowsour.2017.04.043.

[195] B. Gyenes, D. A. Stevens, V. L. Chevrier, and J. R. Dahn, "Understanding Anomalous Behavior in Coulombic Efficiency Measurements on Li-Ion Batteries," *J. Electrochem. Soc.*, vol. 162, no. 3, pp. A278–A283, Jan. 2015, doi: 10.1149/2.0191503jes.

[196] M. Lewerenz, G. Fuchs, L. Becker, and D. U. Sauer, "Irreversible calendar aging and quantification of the reversible capacity loss caused by anode overhang," *Journal of Energy Storage*, vol. 18, pp. 149–159, Aug. 2018, doi: 10.1016/j.est.2018.04.029.

[197] M. Lewerenz, J. Münnix, J. Schmalstieg, S. Käbitz, M. Knips, and D. U. Sauer, "Systematic aging of commercial LiFePO4|Graphite cylindrical cells including a theory explaining rise of capacity during aging," *Journal of Power Sources*, vol. 345, pp. 254–263, Mar. 2017, doi: 10.1016/j.jpowsour.2017.01.133.

[198] S. Käbitz, "Untersuchung der Alterung von Lithium-Ionen-Batterien mittels Elektroanalytik und elektrochemischer Impedanzspektroskopie," PhD thesis, RWTH Aachen University, Aachen, Germany, 2016. doi: 10.18154/RWTH-2016-12094.

[199] M. Ecker, N. Nieto, S. Käbitz, J. Schmalstieg, H. Blanke, A. Warnecke, and D. U. Sauer, "Calendar and cycle life study of Li(NiMnCo)O2-based 18650 lithium-ion batteries," *Journal of Power Sources*, vol. 248, pp. 839–851, Feb. 2014, doi: 10.1016/j.jpowsour.2013.09.143.

[200] M. Lewerenz, P. Dechent, and D. U. Sauer, "Investigation of capacity recovery during rest period at different states-of-charge after cycle life test for prismatic Li(Ni1/3Mn1/3Co1/3)O2-graphite cells," *Journal of Energy Storage*, vol. 21, pp. 680–690, Feb. 2019, doi: 10.1016/j.est.2019.01.004.

[201] B. Epding, B. Rumberg, H. Jahnke, I. Stradtmann, and A. Kwade, "Investigation of significant capacity recovery effects due to long rest periods during high current cyclic aging tests in automotive lithium ion cells

and their influence on lifetime," *Journal of Energy Storage*, vol. 22, pp. 249–256, Apr. 2019, doi: 10.1016/j.est.2019.02.015.

[202] K. A. Severson, P. M. Attia, N. Jin, N. Perkins, B. Jiang, Z. Yang, M. H. Chen, M. Aykol, P. K. Herring, D. Fraggedakis, M. Z. Bazant, S. J. Harris, W. C. Chueh, and R. D. Braatz, "Data-driven prediction of battery cycle life before capacity degradation," *Nature Energy*, vol. 4, no. 5, pp. 383–391, May 2019, doi: 10.1038/s41560-019-0356-8.

[203] P. M. Attia, A. Grover, N. Jin, K. A. Severson, T. M. Markov, Y.-H. Liao, M. H. Chen, B. Cheong, N. Perkins, Z. Yang, P. K. Herring, M. Aykol, S. J. Harris, R. D. Braatz, S. Ermon, and W. C. Chueh, "Closed-loop optimization of fast-charging protocols for batteries with machine learning," *Nature*, vol. 578, no. 7795, pp. 397–402, Feb. 2020, doi: 10.1038/s41586-020-1994-5.

[204] P. Fermín-Cueto, E. McTurk, M. Allerhand, E. Medina-Lopez, M. F. Anjos, J. Sylvester, and G. dos Reis, "Identification and machine learning prediction of knee-point and knee-onset in capacity degradation curves of lithium-ion cells," *Energy and AI*, vol. 1, p. 100006, Aug. 2020, doi: 10.1016/j.egyai.2020.100006.

[205] M. W. Woolrich, T. E. J. Behrens, C. F. Beckmann, M. Jenkinson, and S. M. Smith, "Multilevel linear modelling for FMRI group analysis using Bayesian inference," *NeuroImage*, vol. 21, no. 4, pp. 1732–1747, Apr. 2004, doi: 10.1016/j.neuroimage.2003.12.023.

[206] K. P. Murphy, *Machine learning: a probabilistic perspective*. Cambridge, MA: MIT Press, 2012.

[207] S. Theodoridis, "Chapter 13 - Bayesian Learning: Approximate Inference and Nonparametric Models," in *Machine Learning (Second Edition)*, S. Theodoridis, Ed. Academic Press, 2020, pp. 647–730. doi: 10.1016/B978-0-12-818803-3.00025-8.

[208] P. Dechent, S. Greenbank, F. Hildenbrand, S. Jbabdi, D. U. Sauer, and D. A. Howey, "Estimation of Li-ion degradation test sample sizes required to understand cell-to-cell variability," *arXiv:2107.07881 [q-bio, stat]*, Jul. 2021, Accessed: Jul. 31, 2021. [Online]. Available: http://arxiv.org/abs/2107.07881

[209] P. Dechent, A. Epp, D. Jöst, Y. Preger, P. M. Attia, W. Li, and D. U. Sauer, "ENPOLITE: Comparing Lithium-Ion Cells across Energy, Power,

Lifetime, and Temperature," *ACS Energy Lett.*, pp. 2351–2355, Jun. 2021, doi: 10.1021/acsenergylett.1c00743.

[210] J. Figgener, P. Stenzel, K.-P. Kairies, J. Linßen, D. Haberschusz, O. Wessels, G. Angenendt, M. Robinius, D. Stolten, and D. U. Sauer, "The development of stationary battery storage systems in Germany – A market review," *Journal of Energy Storage*, vol. 29, p. 101153, Jun. 2020, doi: 10.1016/j.est.2019.101153.

[211] D. V. Ragone, "Review of Battery Systems for Electrically Powered Vehicles," Feb. 1968, p. 680453. doi: 10.4271/680453.

[212] G. Sikha, P. Ramadass, B. S. Haran, R. E. White, and B. N. Popov, "Comparison of the capacity fade of Sony US 18650 cells charged with different protocols," *Journal of Power Sources*, vol. 122, no. 1, pp. 67–76, Jul. 2003, doi: 10.1016/S0378-7753(03)00027-2.

[213] S. Käbitz, J. B. Gerschler, M. Ecker, Y. Yurdagel, B. Emmermacher, D. Andri, T. Mitsch, and D. U. Sauer, "Cycle and calendar life study of a graphite|LiNi1/3Mn1/3Co1/3O2 Li-ion high energy system. Part A: Full cell characterization," *Journal of Power Sources*, vol. 239, pp. 572–583, Oct. 2013, doi: 10.1016/j.jpowsour.2013.03.045.

[214] M. Ecker, J. B. Gerschler, J. Vogel, S. Käbitz, F. Hust, P. Dechent, and D. U. Sauer, "Development of a lifetime prediction model for lithium-ion batteries based on extended accelerated aging test data," *Journal of Power Sources*, vol. 215, pp. 248–257, Oct. 2012, doi: 10.1016/j.jpowsour.2012.05.012.

[215] M. Dubarry, C. Truchot, and B. Y. Liaw, "Cell degradation in commercial LiFePO4 cells with high-power and high-energy designs," *Journal of Power Sources*, vol. 258, pp. 408–419, Jul. 2014, doi: 10.1016/j.jpowsour.2014.02.052.

[216] M. Dubarry, N. Qin, and P. Brooker, "Calendar aging of commercial Li-ion cells of different chemistries – A review," *Current Opinion in Electrochemistry*, vol. 9, pp. 106–113, Jun. 2018, doi: 10.1016/j.coelec.2018.05.023.

[217] Y. Preger, H. M. Barkholtz, A. Fresquez, D. L. Campbell, B. W. Juba, J. Romàn-Kustas, S. R. Ferreira, and B. R. Chalamala, "Degradation of Commercial Lithium-ion Cells as a Function of Chemistry and Cycling Conditions," *J. Electrochem. Soc.*, 2020, doi: 10.1149/1945-7111/abae37.

[218] M. Dubarry, G. Baure, and A. Devie, “Durability and Reliability of EV Batteries under Electric Utility Grid Operations: Path Dependence of Battery Degradation,” *J. Electrochem. Soc.*, vol. 165, no. 5, pp. A773–A783, Jan. 2018, doi: 10.1149/2.0421805jes.

[219] P. Albertus, S. Babinec, S. Litzelman, and A. Newman, “Status and challenges in enabling the lithium metal electrode for high-energy and low-cost rechargeable batteries,” *Nature Energy*, vol. 3, no. 1, Art. no. 1, Jan. 2018, doi: 10.1038/s41560-017-0047-2.

[220] T. Baumhöfer, M. Brühl, S. Rothgang, and D. U. Sauer, “Production caused variation in capacity aging trend and correlation to initial cell performance,” *Journal of Power Sources*, vol. 247, pp. 332–338, Feb. 2014, doi: 10.1016/j.jpowsour.2013.08.108.

[221] I. Schoeneberger, P. Dechent, F. Rücker, S. Jakobowski, and D. U. Sauer, “Improving Aging Prediction for Electric Vehicle Operation with Combined Electrical, Thermal and Aging Model for Lithium-Ion Battery Packs Using Quantitative Cell Data,” *Meet. Abstr.*, vol. MA2019-04, no. 2, p. 104, Jun. 2019, doi: 10.1149/MA2019-04/2/104.

[222] S. Liu, M. Winter, M. Lewerenz, J. Becker, D. U. Sauer, Z. Ma, and J. Jiang, “Analysis of cyclic aging performance of commercial Li4Ti5O12-based batteries at room temperature,” *Energy*, vol. 173, pp. 1041–1053, Apr. 2019, doi: 10.1016/j.energy.2019.02.150.

[223] J. Schmalstieg, S. Käbitz, M. Ecker, and D. U. Sauer, “A holistic aging model for Li(NiMnCo)O2 based 18650 lithium-ion batteries,” *Journal of Power Sources*, vol. 257, pp. 325–334, Jul. 2014, doi: 10.1016/j.jpowsour.2014.02.012.

[224] M. Ecker, N. Nieto, S. Käbitz, J. Schmalstieg, H. Blanke, A. Warnecke, and D. U. Sauer, “Calendar and cycle life study of Li(NiMnCo)O2-based 18650 lithium-ion batteries,” *Journal of Power Sources*, vol. 248, pp. 839–851, Feb. 2014, doi: 10.1016/j.jpowsour.2013.09.143.

[225] T. Nemeth, P. Schröer, M. Kuipers, and D. U. Sauer, “Lithium titanate oxide battery cells for high-power automotive applications – Electro-thermal properties, aging behavior and cost considerations,” *Journal of Energy Storage*, vol. 31, p. 101656, Oct. 2020, doi: 10.1016/j.est.2020.101656.

[226] P. Schröer, E. Khoshbakht, T. Nemeth, M. Kuipers, H. Zappen, and D. U. Sauer, “Adaptive modeling in the frequency and time domain of high-power lithium titanate oxide cells in battery management systems,” *Journal*

of Energy Storage, vol. 32, p. 101966, Dec. 2020, doi: 10.1016/j.est.2020.101966.

[227] A. Marongiu, M. Roscher, and D. U. Sauer, "Influence of the vehicle-to-grid strategy on the aging behavior of lithium battery electric vehicles," *Applied Energy*, vol. 137, pp. 899–912, Jan. 2015, doi: 10.1016/j.apenergy.2014.06.063.

[228] A. Marongiu, F. G. W. Nußbaum, W. Waag, M. Garmendia, and D. U. Sauer, "Comprehensive study of the influence of aging on the hysteresis behavior of a lithium iron phosphate cathode-based lithium ion battery – An experimental investigation of the hysteresis," *Applied Energy*, vol. 171, pp. 629–645, Jun. 2016, doi: 10.1016/j.apenergy.2016.02.086.

[229] S. Lehner, *Reliability Assessment of Lithium-Ion Battery Systems with Special Emphasis on Cell Performance Distribution*, 1st ed. Shaker, PhD thesis, RWTH Aachen University, 2017.

[230] M. Naumann, F. B. Spingler, and A. Jossen, "Analysis and modeling of cycle aging of a commercial LiFePO4/graphite cell," *Journal of Power Sources*, vol. 451, p. 227666, Mar. 2020, doi: 10.1016/j.jpowsour.2019.227666.

[231] F. B. Spingler, M. Naumann, and A. Jossen, "Capacity Recovery Effect in Commercial LiFePO4 / Graphite Cells," *J. Electrochem. Soc.*, vol. 167, no. 4, p. 040526, Mar. 2020, doi: 10.1149/1945-7111/ab7900.

[232] M. Naumann, M. Schimpe, P. Keil, H. C. Hesse, and A. Jossen, "Analysis and modeling of calendar aging of a commercial LiFePO4/graphite cell," *Journal of Energy Storage*, vol. 17, pp. 153–169, Jun. 2018, doi: 10.1016/j.est.2018.01.019.

[233] J. E. Harlow, X. Ma, J. Li, E. Logan, Y. Liu, N. Zhang, L. Ma, S. L. Glazier, M. M. E. Cormier, M. Genovese, S. Buteau, A. Cameron, J. E. Stark, and J. R. Dahn, "A Wide Range of Testing Results on an Excellent Lithium-Ion Cell Chemistry to be used as Benchmarks for New Battery Technologies," *J. Electrochem. Soc.*, vol. 166, no. 13, p. A3031, Sep. 2019, doi: 10.1149/2.0981913jes.

[234] J. Schmitt, A. Maheshwari, M. Heck, S. Lux, and M. Vetter, "Impedance change and capacity fade of lithium nickel manganese cobalt oxide-based batteries during calendar aging," *Journal of Power Sources*, vol. 353, pp. 183–194, Jun. 2017, doi: 10.1016/j.jpowsour.2017.03.090.

[235] M. Schimpe, M. E. von Kuepach, M. Naumann, H. C. Hesse, K. Smith, and A. Jossen, "Comprehensive Modeling of Temperature-Dependent Degradation Mechanisms in Lithium Iron Phosphate Batteries," *J. Electrochem. Soc.*, vol. 165, no. 2, p. A181, Jan. 2018, doi: 10.1149/2.1181714jes.

[236] P. Keil, S. Schuster, J. Wilhelm, J. Travi, A. Hauser, R. Karl, and A. Jossen, "Calendar Aging of Lithium-Ion Batteries: I. Impact of the Graphite Anode on Capacity Fade," *Journal of The Electrochemical Society*, vol. 163, pp. A1872–A1880, Jan. 2016, doi: 10.1149/2.0411609jes.

[237] P. Keil and A. Jossen, "Calendar Aging of NCA Lithium-Ion Batteries Investigated by Differential Voltage Analysis and Coulomb Tracking," *J. Electrochem. Soc.*, vol. 164, no. 1, p. A6066, Oct. 2016, doi: 10.1149/2.0091701jes.

[238] A. Devie, G. Baure, and M. Dubarry, "Intrinsic Variability in the Degradation of a Batch of Commercial 18650 Lithium-Ion Cells," *Energies*, vol. 11, no. 5, p. 1031, Apr. 2018, doi: 10.3390/en11051031.

[239] Y. Wu, P. Keil, S. F. Schuster, and A. Jossen, "Impact of Temperature and Discharge Rate on the Aging of a LiCoO2/LiNi0.8Co0.15Al0.05O2 Lithium-Ion Pouch Cell," *J. Electrochem. Soc.*, vol. 164, no. 7, pp. A1438–A1445, Jan. 2017, doi: 10.1149/2.0401707jes.

[240] D. Anseán, M. Dubarry, A. Devie, B. Y. Liaw, V. M. García, J. C. Viera, and M. González, "Fast charging technique for high power LiFePO4 batteries: A mechanistic analysis of aging," *Journal of Power Sources*, vol. 321, pp. 201–209, Jul. 2016, doi: 10.1016/j.jpowsour.2016.04.140.

[241] I. Zilberman, J. Sturm, and A. Jossen, "Reversible self-discharge and calendar aging of 18650 nickel-rich, silicon-graphite lithium-ion cells," *Journal of Power Sources*, vol. 425, pp. 217–226, Jun. 2019, doi: 10.1016/j.jpowsour.2019.03.109.

[242] D. D. MacNeil, Z. Lu, Z. Chen, and J. R. Dahn, "A comparison of the electrode/electrolyte reaction at elevated temperatures for various Li-ion battery cathodes," *Journal of Power Sources*, vol. 108, no. 1, pp. 8–14, Jun. 2002, doi: 10.1016/S0378-7753(01)01013-8.

[243] X.-G. Yang, T. Liu, and C.-Y. Wang, "Thermally modulated lithium iron phosphate batteries for mass-market electric vehicles," *Nat Energy*, vol. 6, no. 2, pp. 176–185, Feb. 2021, doi: 10.1038/s41560-020-00757-7.

[244] P. Kuntz, O. Raccurt, P. Azaïs, K. Richter, T. Waldmann, M. Wohlfahrt-Mehrens, M. Bardet, A. Buzlukov, and S. Genies, “Identification of Degradation Mechanisms by Post-Mortem Analysis for High Power and High Energy Commercial Li-Ion Cells after Electric Vehicle Aging,” *Batteries*, vol. 7, no. 3, Art. no. 3, Sep. 2021, doi: 10.3390/batteries7030048.

[245] J. Zhu, M. Knapp, D. R. Sørensen, M. Heere, M. S. D. Darma, M. Müller, L. Mereacre, H. Dai, A. Senyshyn, X. Wei, and H. Ehrenberg, “Investigation of capacity fade for 18650-type lithium-ion batteries cycled in different state of charge (SoC) ranges,” *Journal of Power Sources*, vol. 489, p. 229422, Mar. 2021, doi: 10.1016/j.jpowsour.2020.229422.

[246] B. Rumberg, K. Schwarzkopf, B. Epding, I. Stradtmann, and A. Kwade, “Understanding the different aging trends of usable capacity and mobile Li capacity in Li-ion cells,” *Journal of Energy Storage*, vol. 22, pp. 336–344, Apr. 2019, doi: 10.1016/j.est.2019.02.029.

[247] S. F. Schuster, M. J. Brand, C. Campestrini, M. Gleissenberger, and A. Jossen, “Correlation between capacity and impedance of lithium-ion cells during calendar and cycle life,” *Journal of Power Sources*, vol. 305, pp. 191–199, Feb. 2016, doi: 10.1016/j.jpowsour.2015.11.096.

[248] A. Epp, “Technische & Wirtschaftliche Bewertung von Interzellstreuungen in Modellierten Batteriepacks,” Bachelor thesis, RWTH Aachen University, Aachen, Germany, 2018.

[249] E. Barbers, “Multiskalen-Alterungssimulation und datengetriebene automatisierte Vermessung von Lithium-Ionen-Batterien,” Master thesis, RWTH Aachen University, Aachen, Germany, 2021.

[250] J. Newman and W. Tiedemann, “Porous-electrode theory with battery applications,” *AIChE Journal*, vol. 21, no. 1, pp. 25–41, Jan. 1975, doi: 10.1002/aic.690210103.

[251] V. Ramadesigan, P. W. C. Northrop, S. De, S. Santhanagopalan, R. D. Braatz, and V. R. Subramanian, “Modeling and Simulation of Lithium-Ion Batteries from a Systems Engineering Perspective,” *J. Electrochem. Soc.*, vol. 159, no. 3, pp. R31–R45, Jan. 2012, doi: 10.1149/2.018203jes.

[252] A. A. Franco, “Multiscale modelling and numerical simulation of rechargeable lithium ion batteries: concepts, methods and challenges,” *RSC Adv.*, vol. 3, no. 32, pp. 13027–13058, Jul. 2013, doi: 10.1039/C3RA23502E.

[253] F. E. Hust, “Physico-chemically motivated parameterization and modelling of real-time capable lithium-ion battery models : a case study on the tesla model s battery,” PhD thesis, RWTH Aachen University, Aachen, Germany, 2019. doi: 10.18154/RWTH-2019-00249.

[254] M. Fleckenstein, S. Fischer, O. Bohlen, and B. Bäker, “Thermal Impedance Spectroscopy - A method for the thermal characterization of high power battery cells,” *Journal of Power Sources*, vol. 223, pp. 259–267, Feb. 2013, doi: 10.1016/j.jpowsour.2012.07.144.

[255] H. Maleki, H. Wang, W. Porter, and J. Hallmark, “Li-Ion polymer cells thermal property changes as a function of cycle-life,” *Journal of Power Sources*, vol. 263, pp. 223–230, Oct. 2014, doi: 10.1016/j.jpowsour.2014.04.033.

[256] C. R. Birkl, M. R. Roberts, E. McTurk, P. G. Bruce, and D. A. Howey, “Degradation diagnostics for lithium ion cells,” *Journal of Power Sources*, vol. 341, pp. 373–386, Feb. 2017, doi: 10.1016/j.jpowsour.2016.12.011.

[257] J. M. Reniers, G. Mulder, and D. A. Howey, “Review and Performance Comparison of Mechanical-Chemical Degradation Models for Lithium-Ion Batteries,” *J. Electrochem. Soc.*, vol. 166, no. 14, pp. A3189–A3200, Jan. 2019, doi: 10.1149/2.0281914jes.

[258] M. Dubarry, C. Truchot, and B. Y. Liaw, “Synthesize battery degradation modes via a diagnostic and prognostic model,” *Journal of Power Sources*, vol. 219, pp. 204–216, Dec. 2012, doi: 10.1016/j.jpowsour.2012.07.016.

[259] J. Schmalstieg, S. Käbitz, M. Ecker, and D. U. Sauer, “A holistic aging model for Li(NiMnCo)O2 based 18650 lithium-ion batteries,” *Journal of Power Sources*, vol. 257, pp. 325–334, Jul. 2014, doi: 10.1016/j.jpowsour.2014.02.012.

[260] H. M. Dahn, A. J. Smith, J. C. Burns, D. A. Stevens, and J. R. Dahn, “User-Friendly Differential Voltage Analysis Freeware for the Analysis of Degradation Mechanisms in Li-Ion Batteries,” *J. Electrochem. Soc.*, vol. 159, no. 9, pp. A1405–A1409, Jan. 2012, doi: 10.1149/2.013209jes.

[261] M. Dubarry and D. Beck, “Big data training data for artificial intelligence-based Li-ion diagnosis and prognosis,” *Journal of Power Sources*, vol. 479, p. 228806, Dec. 2020, doi: 10.1016/j.jpowsour.2020.228806.

[262] T. Müller-Gronbach, E. Novak, and K. Ritter, *Monte Carlo-Algorithmen*. Berlin Heidelberg: Springer-Verlag, 2012. Accessed: Apr. 26, 2019. [Online]. Available: https://www.springer.com/de/book/9783540891406

[263] J. N. Becker, "Flexible Dimensionierung und Optimierung hybrider Lithium-Ionenbatteriespeichersysteme mit verschiedenen Auslegungszielen," PhD thesis, RWTH Aachen University, Aachen, Germany, 2017. doi: 10.18154/RWTH-2017-09278.

[264] T. Nemeth, A. Bubert, J. N. Becker, R. W. D. Doncker, and D. U. Sauer, "A Simulation Platform for Optimization of Electric Vehicles With Modular Drivetrain Topologies," *IEEE Transactions on Transportation Electrification*, vol. 4, no. 4, pp. 888–900, Dec. 2018, doi: 10.1109/TTE.2018.2869371.

[265] J. Becker, T. Nemeth, R. Wegmann, and D. U. Sauer, "Dimensioning and Optimization of Hybrid Li-Ion Battery Systems for EVs," *World Electric Vehicle Journal*, vol. 9, no. 2, p. 19, Jun. 2018, doi: 10.3390/wevj9020019.

[266] M. Dubarry, G. Baure, C. Pastor-Fernández, T. F. Yu, W. D. Widanage, and J. Marco, "Battery energy storage system modeling: A combined comprehensive approach," *Journal of Energy Storage*, vol. 21, pp. 172–185, Feb. 2019, doi: 10.1016/j.est.2018.11.012.

10 Licenses

Figure 1.2 by Kavlak et al. [6], reprinted with permission of Elsevier.
Figure 2.2 by M. Roser [24], licensed under CC-BY-4.0
Figure 3.4 by Myall et al. [31], licensed under CC-BY-4.0
Figure 3.5 by Müller et al. [54], licensed under CC-BY-4.0
Figure 3.6 by Mauler et al. [74], licensed under CC-BY-4.0
Figure 3.7 by Loveridge et al. [104], licensed under CC-BY-4.0
Figure 3.8 by Paxton et al. [48] Reproduced with permission from Elsevier, Copyright 2015 and by Müller et al. [147], licensed under CC-BY-4.0
Figure 3.9 by Petz et al. [149] Reproduced with permission from Elsevier, Copyright 2020.
Figure 3.10 by Sieg et al. [50] Reproduced and modified with permission from Elsevier, Copyright 2020.
Figure 3.11 by Käbitz [166] , licensed under CC-BY-4.0
Figure 3.13 modified from Waldmann et al. [155], licensed under CC-BY-4.0
Figure 6.4 by Birkl et al. [256], licensed under CC-BY-4.0
Figure 6.7 by Ecker et al. [199], reprinted with permission of Elsevier.
Figure 6.9 by Dahn et al. [260], reprinted with permission from IOP Publishing.

For CC-BY-4.0 see www.creativecommons.org/licenses/by/4.0

11 Own Publications

Journal Articles

1. **P. Dechent***, A. Epp*, D. Joest, Y. Preger, P.M. Attia, W. Li, D.U. Sauer, "ENPOLITE: Comparing Lithium-Ion Cells across Energy, Power, Lifetime, and Temperature" ACS Energy Lett., pp. 2351–2355, Jun. 2021, doi: 10.1021/acsenergylett.1c00743. **equal contribution*
2. **P. Dechent***, S. Greenbank*, F. Hildenbrand, S. Jbabdi, D.U. Sauer, D. A. Howey "Statistical analysis of sample sizes required for Li-ion cell degradation testing", 2021 Batteries & Supercaps, Wiley doi: 10.1002/batt.202100148 **equal contribution*
3. L. Ward, S. Babinec, E.J. Dufek, D.A. Howey, V. Viswanathan, M. Aykol, D.A.C. Beck, B. Blaiszik, B.R. Chen, G. Crabtree, V. De Angelis, **P. Dechent**, M. Dubarry, E.E. Eggleton, D.P. Finegan, I. Foster, C. Gopal, P.K. Herring, V.W. Hu, N.H. Paulson, Y. Preger, D.U. Sauer, K. Smith, S.W. Snyder, S. Sripad, T.R. Tanim, L. Teo "Principles of a Battery Data Genome" Joule 2022 Elsevier, *in print*
4. D. Beck*, **P. Dechent***, M. Junker, D.U. Sauer, M. Dubarry, "Inhomogeneities and Cell-to-cell Variations in Lithium-ion Batteries, a review", Energies, vol. 14, no. 11, Art. no. 11, Jan. 2021, doi: 10.3390/en14113276 **equal contribution*
5. T. Frambach, R. Liedtke, **P. Dechent**, D. U. Sauer and E. Figgemeier, „A review on aging-aware system simulation for plug-in hybrids", IEEE Transactions on Transportation Electrification, 2021, pp. 1–1, 2021, doi: 10.1109/TTE.2021.3104105.
6. W. Li, N. Sengupta, **P. Dechent,** D. Howey, A. Annaswamy, and D. U. Sauer, "One-shot battery degradation trajectory prediction with deep learning," Journal of Power Sources, vol. 482, p. 228863, Jan. 2021, doi: 10.1016/j.jpowsour.2020.228863.
7. W. Li, N. Sengupta, **P. Dechent,** D. Howey, A. Annaswamy, and D. U. Sauer, "Online capacity estimation of lithium-ion batteries with deep long short-term memory networks," Journal of Power Sources, vol. 482, p. 228863, Jan. 2021, doi: 10.1016/j.jpowsour.2020.228863.

8. L.K. Willenberg, **P. Dechent**, G. Fuchs, M. Teuber, M. Eckert, M. Graff, N. Kürten, D.U. Sauer, E. Figgemeier, "The development of jelly roll deformation in 18650 lithium-ion batteries at low state of charge," J. Electrochem. Soc., 2020, doi: 10.1149/1945-7111/aba96d.
9. L. K. Willenberg, **P. Dechent**, G. Fuchs, D. U. Sauer, and E. Figgemeier, "High-Precision Monitoring of Volume Change of Commercial Lithium-Ion Batteries by Using Strain Gauges," Sustainability, vol. 12, no. 2, p. 557, Jan. 2020.
10. M. Johnen, S. Pitzen, U. Kamps, M. Kateri, **P. Dechent**, and D. U. Sauer, "Modeling long-term capacity degradation of lithium-ion batteries," Journal of Energy Storage, p. 102011, Dec. 2020, doi: 10.1016/j.est.2020.102011.
11. M. Lewerenz, **P. Dechent**, and D. U. Sauer, "Investigation of capacity recovery during rest period at different states-of-charge after cycle life test for prismatic Li(Ni1/3Mn1/3Co1/3)O2-graphite cells," Journal of Energy Storage, vol. 21, pp. 680–690, Feb. 2019, doi: 10.1016/j.est.2019.01.004.
12. M. Ecker, T. K. D. Tran, **P. Dechent**, S. Käbitz, A. Warnecke, and D. U. Sauer, "Parameterization of a Physico-Chemical Model of a Lithium-Ion Battery I. Determination of Parameters," J. Electrochem. Soc., vol. 162, no. 9, pp. A1836–A1848, Jan. 2015, doi: 10.1149/2.0551509jes.
13. M. Ecker, J.B. Gerschler, J. Vogel, S. Käbitz, F. Hust, **P. Dechent**, D.U. Sauer, "Development of a lifetime prediction model for lithium-ion batteries based on extended accelerated ageing test data," Journal of Power Sources, vol. 215, pp. 248–257, Oct. 2012, doi: 10.1016/j.jpowsour.2012.05.012.

Conference Proceedings

1. **P. Dechent**, A. Epp, D. Joest, Y. Preger, P.M. Attia, W. Li, D.U. Sauer, “ENPOLITE: Comparing Lithium-Ion Cells across Energy, Power, Lifetime, and Temperature”, invited to Online Battery Modeling Seminar, March 2021 DOI:10.1021/acsenergylett.0c01304
2. **P. Dechent**, L. K. Willenberg, G. Fuchs, D. U. Sauer, and E. Figgemeier ”Ageing behavior and volume expansion of commercial lithium-ion batteries containing silicon” E-MOTIVE 12, Online, 2020
3. **P. Dechent**, L.K. Willenberg, M. Lewerenz, D.U. Sauer, “Limits of accelerated life tests, reversible capacity loss, and the impact of test design” Batteries Gordon Research Conference, Ventura, California, USA, 2020
4. **P. Dechent**, I. Schoeneberger, F.E. Hust, D.U. Sauer “Quantifying failure-rates in lithium-ion batteries with stochastic simulation” E-MOTIVE 11, Schweinfurt, Germany, 2020
5. **P. Dechent**, I. Schoeneberger, F.E. Hust, D.U. Sauer “From Variability and Ageing Rate Spread to Quantification of Failure Rates in Lithium-Ion Packs “, ECEE 2019, Glasgow, Scotland, UK, 2019
6. M. Lewerenz, **P. Dechent**, C. Endisch, D. U. Sauer “Investigation of Capacity and Homogeneity Recovery of Commercial Cells after Cycle Life Tests” 235th ECS Meeting, Dallas, Texas, US, 2019
7. I. Schoeneberger, **P. Dechent**, F. Rücker, S. Jakobowski and D.U. Sauer “Improving Ageing Prediction for Electric Vehicle Operation with Combined Electrical, Thermal and Ageing Model for Lithium-Ion Battery Packs Using Quantitative Cell Data“, ECEE 2019, Glasgow, Scotland, UK, 2019
8. **P. Dechent**, M. Kuipers, D.U. Sauer, “Implication of properties of new cell technologies on system applications” Batteries Gordon Research Conference, Ventura, California, USA, 2018
9. **P. Dechent**, D.U. Sauer, “Impact of Single Cell Faults in Parallel Connections,” POSTER 2016, Prague, Czech Republic, 2016
10. M. Ecker, J. B. Gerschler, J. Vogel, S. Käbitz, F. Hust, **P. Dechent**, D. U. Sauer “Analyzing Calendar Ageing Data towards a Lifetime

Prediction Model for Lithium-Ion Batteries“, EVS26, Los Angeles, California, USA, 2012

Invited Talks

1. University of Michigan, Ann Arbor, December 2020
2. Dalhousie University, Halifax Canada, September 2020
3. Oxford University, Oxford UK, September 2019

Supervised student thesis

The developed procedures and methods as well as the results of this work are partly based on the following student research projects, which I supervised during my work as a research assistant at ISEA. The corresponding content is not explicitly mentioned.

Master Theses

1. Julian Tenhagen: Untersuchung von Inhomogenitäten in Lithium-Ionen-Zellen und deren Auswirkung auf Batteriepacks, 2018, RWTH Aachen
2. Alexander Epp: Big-Data-Analyse technologieübergreifender Lebensdauerdaten von Lithium-Ionen Batterien, 2020, RWTH Aachen
3. Elias Barbers: Multiskalen-Alterungssimulation und datengetriebene automatisierte Vermessung von Lithium-Ionen Batterien, 2021, RWTH Aachen

Bachelor Theses

1. Marcel Eckert: Batteriemodellierung für hohe Lade- und Entladeraten zur Ermittlung effizienter Betriebsstrategien, 2017, RWTH Aachen
2. Alexander Epp: Technische & Wirtschaftliche Bewertung von Interzellstreuungen in Modellierten Batteriepacks, 2018, RWTH Aachen

3. Philipp Richard: Entwicklung einer Hochstromkontaktierung zur Vermessung von prismatischen Hochleistungsbatterien, 2018, RWTH Aachen

Project Theses

1. Mark Richter, Vergleich verschiedener Prototypverfahren für Batteriepacks auf Kunststoffbasis, 2017, RWTH Aachen

The work was also supported by the work of the following students:

1. Jan Biederbeck
2. Julian Tenhagen
3. Marcel Eckert
4. Alexander Epp
5. Elias Barbers
6. Sarah Leibeling
7. Miriam Wittbusch

ABISEA Band 1
Eßer, Albert
Berührungslose, kombinierte Energie- und Informationsübertragung für bewegliche Systeme
1. Aufl. 1992, 129 S.
ISBN 3-86073-046-0

ABISEA Band 2
Vogel, Ulrich
Entwurf und Beurteilung von Verfahren zur Hochausnutzung des Rad-Schiene-Kraftschlusses durch Triebfahrzeuge
1. Aufl. 1992, 131 S.
ISBN 3-86073-060-6

ABISEA Band 3
Reckhorn, Thomas
Stromeinprägendes Antriebssystem mit fremderregter Synchronmaschine
1. Aufl. 1992, 128 S.
ISBN 3-86073-061-4

ABISEA Band 4
Ackva, Ansgar
Spannungseinprägendes Antriebssystem mit Synchronmaschine und direkter Stromregelung
1. Aufl. 1992, 137 S.
ISBN 3-86073-062-2

ABISEA Band 5
Mertens, Axel
Analyse des Oberschwingungsverhaltens von taktsynchronen Delta - Modulationsverfahren zur Steuerung von Pulsstromrichtern bei hoher Taktzahl
1. Aufl. 1992, 178 S.
ISBN 3-86073-069-X

ABISEA Band 6
Geuer, Wolfgang
Untersuchungen über das Alterungsverhalten von Blei-Akkumulatoren
1. Aufl. 1993, 97 S.
ISBN 3-86073-097-5

ABISEA Band 7
Langheim, Jochen
Einzelradantrieb für Elektrostraßenfahrzeuge
1. Aufl. 1993, 213 S.
ISBN 3-86073-123-8
(vergriffen)

ABISEA Band 8
Fetz, Joachim
Fehlertolerante Regelung eines Asynchron-Doppelantriebes für ein Elektrospeicherfahrzeug
1. Aufl. 1993, 136 S.
ISBN 3-86073-124-6
(vergriffen)

ABISEA Band 9
Schülting, Ludger
Optimierte Auslegung induktiver Bauelemente für den Mittelfrequenzbereich
1. Aufl. 1993, 126 S.
ISBN 3-86073-174-2
(vergriffen)

ABISEA Band 10
Skudelny, H.-Ch.
Stromrichtertechnik
4. Aufl. 1997, 259 S.
ISBN 3-86073-189-0

ABISEA Band 11
Skudelny, H.-Ch.
Elektrische Antriebe
3. Aufl. 1997, 124 S.
ISBN 3-86073-231-5

ABISEA Band 12
Schöpe, Friedhelm
Batterie-Management für Nickel-Cadmium Akkumulatoren
1. Aufl. 1994, 148 S.
ISBN 3-86073-232-3
(vergriffen)

ABISEA Band 13
v. d. Weem, Jürgen
Schmalbandige aktive Filter für Schienentriebfahrzeuge am Gleichspannungsfahrdraht
1. Aufl. 1995, 126 S.
ISBN 3-86073-233-1

ABISEA Band 14
Backhaus, Klaus
Spannungseinprägendes Direktantriebssystem mit schnelllaufender geschalteter Reluktanzmaschine
1. Aufl. 1995, 146 S.
ISBN 3-86073-234-X
(vergriffen)

ABISEA Band 15
Reinold, Harry
Optimierung dreiphasiger Pulsdauermodulationsverfahren
1. Aufl. 1996, 107 S.
ISBN 3-86073-235-8

ABISEA Band 16
Köpken, Hans-Georg
Regelverfahren für Parallelschwingkreisumrichter
1. Aufl. 1996, 125 S.
ISBN 3-86073-236-6

ABISEA Band 17
Mauracher, Peter
Modellbildung und Verbundoptimierung bei Elektrostraßenfahrzeugen
1. Aufl. 1996, 192 S.
ISBN 3-86073-237-4

ABISEA Band 18
Protiwa, Franz-Ferdinand
Vergleich dreiphasiger Resonanz-Wechselrichter in Simulation und Messung
1. Aufl. 1997, 178 S.
ISBN 3-86073-238-2

ABISEA Band 19
Brockmeyer, Ansgar
Dimensionierungswerkzeug für magnetische Bauelemente in Stromrichteranwendungen
1. Aufl. 1997, 175 S.
ISBN 3-86073-239-0

ABISEA Band 20
Apeldoorn, Oscar
Simulationsgestützte Bewertung von Steuerverfahren für netzgeführte Stromrichter mit verringerter Netzrückwirkung
1. Aufl. 1997, 134 S.
ISBN 3-86073-680-9

ABISEA Band 21
Lohner, Andreas
Batteriemanagement für verschlossene Blei-Batterien am Beispiel von Unterbrechungsfreien Stromversorgungen
1. Aufl. 1998, 126 S.
ISBN 3-86073-681-7

ABISEA Band 22
Reinert, Jürgen
Optimierung der Betriebseigenschaften von Antrieben mit geschalteter Reluktanzmaschine
1. Aufl. 1998, 153 S.
ISBN 3-86073-682-5

ABISEA Band 23
Nagel, Andreas
Leitungsgebundene Störungen in der Leistungselektronik: Entstehung, Ausbreitung und Filterung
1. Aufl. 1999, 140 S.
ISBN 3-86073-683-3

ABISEA Band 24
Menne, Marcus
Drehschwingungen im Antriebsstrang von Elektrostraßenfahrzeugen - Analyse und aktive Dämpfung
1. Aufl. 2001, 169 S.
ISBN 3-86073-684-1

ABISEA Band 25
von Bloh, Jochen
Multilevel-Umrichter zum Einsatz in Mittelspannungs-Gleichspannungs-Übertragungen
1. Aufl. 2001, 137 S.
ISBN 3-86073-685-X

ABISEA Band 26
Karden, Eckhard
Using low-frequency impedance spectroscopy for characterization, monitoring, and modeling of industrial batteries
1. Aufl. 2002, 137 S.
ISBN 3-8265-9766-4

ABISEA Band 27
Karipidis, Claus-Ulrich
A Versatile DSP/ FPGA Structure optimized for Rapid Prototyping and Digital Real-Time Simulation of Power Electronic and Electrical Drive Systems
1. Aufl. 2001, 164 S.
ISBN 3-8265-9738-9

ABISEA Band 28
Kahlen, Klemens
Regelungsstrategien für permanentmagnetische Direktantriebe mit mehreren Freiheitsgraden
1. Aufl. 2002, 154 S.
ISBN 3-8322-1222-1

ABISEA Band 29
Inderka, Robert B.
Direkte Drehmomentregelung Geschalteter Reluktanzantriebe
1. Aufl. 2003, 182 S.
ISBN 3-8322-1175-6

ABISEA Band 30
Schröder, Stefan
Circuit-Simulation Models of High-Power Devices Based on Semiconductor Physics
1. Aufl. 2003, 123 S.
ISBN 3-8322-1250-7

ABISEA Band 31
Buller, Stephan
Impedance-Based Simulation Models for Energy Storage Devices in Advanced Automotive Power Systems
1. Aufl. 2003, 138 S.
ISBN 3-8322-1225-6

ABISEA Band 32
Schönknecht, Andreas
Topologien und Regelungsstrategien für das induktive Erwärmen mit hohen Frequenz-Leistungsprodukten
1. Aufl. 2004, 157 S.
ISBN 3-8322-2408-4

ABISEA Band 33
Tolle, Tobias
Konvertertopologien für ein aufwandsarmes, zweistufiges Schaltnetzteil zum Laden von Batterien aus dem Netz
1. Aufl. 2004, 148 S.
ISBN 3-8322-2676-1

ABISEA Band 34
Götting, Gunther
Dynamische Antriebsregelung von Elektrostraßenfahrzeugen unter Berücksichtigung eines schwingungsfähigen Antriebsstrangs
1. Aufl. 2004, 157 S.
ISBN 3-8322-2804-7

ABISEA Band 35
Dieckerhoff, Sibylle
Transformatorlose Stromrichterschaltungen für Bahnfahrzeuge am 16 2/3Hz Netz
1. Aufl. 2004, 147 S.
ISBN 3-8322-3094-7

ABISEA Band 36
Hu, Jing
Bewertung von DC-DC-Topologien und Optimierung eines DC-DC-Leistungsmoduls für das 42-V-Kfz-Bordnetz
1. Aufl. 2004, 148 S.
ISBN 3-8322-3201-X

ABISEA Band 37
Detjen, Dirk-Oliver
Characterization and Modeling of Si-Si Bonded Hydrophobie Interfaces for Novel High-Power BIMOS Devices
1. Aufl. 2004, 135 S.
ISBN 3-8322-2963-9

ABISEA Band 38
Walter, Jörg
Simulationsbasierte Zuverlässigkeitsanalyse in der modernen Leistungselektronik
1. Aufl. 2004, 121 S.
ISBN 3-8322-3481-0

ABISEA Band 39
Schwarzer, Ulrich
IGBT versus GCT in der Mittelspannungsanwendung - ein experimenteller und simulativer Vergleich
1. Aufl. 2005, 170 S.
ISBN 3-8322-4489-1

ABISEA Band 40
Bartram, Markus
IGBT-Umrichtersysteme für Windkraftanlagen: Analyse der Zyklenbelastung, Modellbildung, Optimierung und Lebensdauervorhersage
1. Aufl. 2006, 185 S.
ISBN 3-8322-5039-5

ABISEA Band 41
Ponnaluri, Srinivas
Generalized Design, Analysis and Control of Grid side converters with integrated UPS or Islanding functionality
1. Aufl. 2006, 163 S.
ISBN 3-8322-5281-9

ABISEA Band 42
Jacobs, Joseph
Multi-Phase Series Resonant DC-to-DC Converters
1. Aufl. 2006, 185 S.
ISBN 3-8322-5532-X

ABISEA Band 43
Linzen, Dirk
Impedance-Based Loss Calculation and Thermal Modeling of Electrochemical Energy Storage Devices for Design Considerations of Automotive Power Systems
1. Aufl. 2006, 185 S.
ISBN 3-8322-5706-3

ABISEA Band 44
Fiedler, Jens
Design of Low-Noise Switched Reluctance Drives
1. Aufl. 2007, 176 S.
ISBN 978-3-8322-5864-1

ABISEA Band 45
Fuengwarodsakul, Nisai
Predictive PWM-based Direct Instantaneous Torque Control for Switched Reluctance Machines
1. Aufl. 2007, 141 S.
ISBN 978-3-8322-6210-5

ABISEA Band 46
Meyer, Christoph
Key Components for Future Offshore DC Grids
1. Aufl. 2007, 187 S.
ISBN 978-3-8322-6571-7

ABISEA Band 47
Fujii, Kansuke
Characterization and Optimization of Soft-Switched Multi-Level Converters for STATCOMs
1. Aufl. 2008, 199 S.
ISBN 978-3-8322-6981-4

ABISEA Band 48
Carstensen, Christian
Eddy Currents in Windings of Switched Reluctance Machines
1. Aufl. 2008, 179 S.
ISBN 978-3-8322-7118-3

ABISEA Band 49
Bohlen, Oliver
Impedance-based battery monitoring
1. Aufl. 2008, 190 S.
ISBN 978-3-8322-7606-5

ABISEA Band 50
Thele, Marc
A contribution to the modelling of the charge acceptance of lead-acid batteries - using frequency and time domain based concepts
1. Aufl. 2008, 165 S.
ISBN 978-3-8322-7659-1

ABISEA Band 51
König, Andreas
High Temperature DC-to-DC Converters for Downhole Applications
1. Aufl. 2009, 154 S.
ISBN 978-3-8322-8489-3

ABISEA Band 52
Dick, Christian Peter
Multi-Resonant Converters as Photovoltaic Module-Integrated Maximum Power Point Tracker
1. Aufl. 2010, 182 S.
ISBN 978-3-8322-9199-0

ABISEA Band 53
Kowal, Julia
Spatially resolved impedance of nonlinear inhomogeneous devices: using the example of lead-acid batteries
1. Aufl. 2010, 203 S.
ISBN 978-3-8322-9483-0

ABISEA Band 54
Roscher, Michael Andreas
Zustandserkennung von LiFeP04-Batterien für Hybrid- und Elektrofahrzeuge
1. Aufl. 2011, 186 S.
ISBN 978-3-8322-9738-1

ABISEA Band 55
Hirschmann, Dirk
Highly Dynamic Piezoelectric Positioning
1. Aufl. 2011, 146 S.
ISBN 978-3-8322-9746-6

ABISEA Band 56
Rigbers, Klaus
Highly Efficient Inverter Architectures for Three-Phase Grid Connection of Photovoltaic Generators
1. Aufl. 2011, 244 S.
ISBN 978-3-8322-9816-9

ABISEA Band 57
Kasper, Knut
Analysis and Control of the Acoustic Behavior of Switched Reluctance Drives
1. Aufl. 2011, 205 S.
ISBN 978-3-8322-9869-2

ABISEA Band 58
Köllensperger, Peter
The Internally Commutated Thyristor - Concept, Design and Application
1. Aufl. 2011, 214 S.
ISBN 978-3-8322-9909-5

ABISEA Band 59
Schoenen, Timo
Einsatz eines DC/DC-Wandlers zur Spannungsanpassung zwischen Antrieb und Energiespeicher in Elektro-und Hybridfahrzeugen
1. Aufl. 2011, 128 S.
ISBN 978-3-8440-0622-3

ABISEA Band 60
Hennen, Martin
Switched Reluctance Direct Drive with Integrated Distributed Inverter
1. Aufl. 2012, 141 S.
ISBN 978-3-8440-0731-2

ABISEA Band 61
van Treek, Daniel
Position Sensorless Torque Control of Switched Reluctance Machines
1. Aufl. 2012, 144 S.
ISBN 978-3-8440-1014-5

ABISEA Band 62
Bragard, Michael
The Integrated Emitter Turn-Off Thyristor. An Innovative MOS-Gated High-Power Device
1. Aufl. 2012, 164 S.
ISBN 978-3-8440-1152-4

ABISEA Band 63
Gerschler, Jochen B.
Ortsaufgelöste Modellbildung von Lithium-Ionen-Systemen unter spezieller Berücksichtigung der Batteriealterung
1. Aufl. 2012, 334 S.
ISBN 978-3-8440-1307-8

ABISEA Band 64
Neuhaus, Christoph R.
Schaltstrategien für Geschaltete Reluktanzantriebe mit kleinem Zwischenkreis
1. Aufl. 2012, 133 S.
ISBN 978-3-8440-1487-7

ABISEA Band 65
Butschen, Thomas
Dual-ICT- A Clever Way to Unite Conduction and Switching Optimized Properties in a Single Wafer
1. Aufl. 2012, 168 S.
ISBN 978-3-8440-1771-7

ABISEA Band 66
Plum, Thomas
Design and Realization of High-Power MOS Turn-Off Thyristors
1. Aufl. 2013, 113 S.
ISBN 978-3-8440-1884-4

ABISEA Band 67
Kiel, Martin
Impedanzspektroskopie an Batterien unter besonderer Berücksichtigung von Batteriesensoren für den Feldeinsatz
1. Aufl. 2013, 226 S.
ISBN 978-3-8440-1973-5

ABISEA Band 68
Brauer, Helge
Schnelldrehender Geschalteter Reluktanzantrieb mit extremem Längendurchmesserverhältnis
1. Aufl. 2013, 192 S.
ISBN 978-3-8440-2345-9

ABISEA Band 69
Thomas, Stephan
A Medium-Voltage Multi-Level DC/DC Converter with High Voltage Transformation Ratio
1. Aufl. 2014, 226 S.
ISBN 978-3-8440-2605-4

ABISEA Band 70
Richter, Sebastian
Digitale Regelung von PWM Wechselrichtern mit niedrigen Trägerfrequenzen
1. Aufl. 2014, 126 S.
ISBN 978-3-8440-2641-2

ABISEA Band 71
Bösing, Matthias
Acoustic Modeling of Electrical Drives - Noise and Vibration Synthesis based on Force Response Superposition
1. Aufl. 2014, 188 S.
ISBN 978-3-8440-2752-5

ABISEA Band 72
Waag, Wladislaw
Adaptive algorithms for monitoring of lithium-ion batteries in electric vehicles
1. Aufl. 2014, 232 S.
ISBN 978-3-8440-2976-5

ABISEA Band 73
Sanders, Tilman
Spatially Resolved Electrical In-Situ Measurement Techniques for Fuel Cells
1. Aufl. 2014, 126 S.
ISBN 978-3-8440-3121-8

ABISEA Band 74
Baumhöfer, Thorsten
Statistische Betrachtung experimenteller Alterungsuntersuchungen an Lithium-Ionen Batterien
1. Aufl. 2015, 157 S.
ISBN 978-3-8440-3423-3

ABISEA Band 75
Andre, Dave
Systematic Characterization of Ageing Factors for High-Energy Lithium-Ion Cells and Approaches for Lifetime Modelling Regarding an Optimized Operating Strategy in Automotive Applications
1. Aufl. 2015, 196 S.
ISBN 978-3-8440-3587-2

ABISEA Band 76
Merei, Ghada
Optimization of off-grid hybrid PV-wind-diesel power supplies with multi-technology battery systems taking into account battery aging
1. Aufl. 2015, 184 S.
ISBN 978-3-8440-4148-4

ABISEA Band 77
Schulte, Dominik
Modellierung und experimentelle Validierung der Alterung von Blei-Säure Batterien durch inhomogene Stromverteilung und Säureschichtung
1. Aufl. 2016, 165 S.
ISBN 978-3-8440-4216-0

ABISEA Band 78
Schenk, Mareike
Simulative Untersuchung der Wicklungsverluste in Geschalteten Reluktanzmaschinen
1. Aufl. 2016, 126 S.
ISBN 978-3-8440-4282-5

ABISEA Band 79
Wang, Yu
Development of Dynamic Models with Spatial Resolution for Electrochemical Energy Converters as Basis for Control and Management Strategies
1. Aufl. 2016, 188 S.
ISBN 978-3-8440-4303-7

ABISEA Band 80
Ecker, Madeleine
Lithium Plating in Lithium-Ion Batteries:
An Experimental and Simulation Approach
1. Aufl. 2016, 154 S.
ISBN 978-3-8440-4525-3

ABISEA Band 81
Zhou, Wei
Modellbasierte Auslegungsmethode von Temperierungssystemen für Hochvolt-Batterien in Personenkraftfahrzeugen
1. Aufl. 2016, 175 S.
ISBN 978-3-8440-4589-5

ABISEA Band 82
Lunz, Benedikt
Deutschlands Stromversorgung im Jahr 2050
Ein szenariobasiertes Verfahren zur vergleichenden Bewertung von Systemvarianten und Flexibilitätsoptionen
1. Aufl. 2016, 187 S.
ISBN 978-3-8440-4627-4

ABISEA Band 83
Hofmann, Andreas G.
Direct Instantaneous Force Control: Key to Low-Noise Switched Reluctance Traction Drives
1. Aufl. 2016, 228 S.
ISBN 978-3-8440-4715-8

ABISEA Band 84
Budde-Meiwes, Heide
Dynamic Charge Acceptance of Lead-Acid Batteries for Micro-Hybrid Automotive Applications
1. Aufl. 2016, 157 S.
ISBN 978-3-8440-4733-2

ABISEA Band 85
Engel, Stefan P.
Thyristor-Based High-Power On-Load Tap Changers Control under Harsh Load Conditions
1. Aufl. 2016, 156 S.
ISBN 978-3-8440-4986-2

ABISEA Band 86
Van Hoek, Hauke
Design and Operation Considerations of Three-Phase Dual Active Bridge Converters for Low-Power Applications with Wide Voltage Ranges
1. Aufl. 2017, 231 S.
ISBN 978-3-8440-5011-0

ABISEA Band 87
Diekhans, Tobias
Wireless Charging of Electric Vehicles - a Pareto-Based Comparison of Power Electronic Topologies
1. Aufl. 2017, 151 S.
ISBN 978-3-8440-5048-6

ABISEA Band 88
Lehner, Susanne
Reliability Assessment of Lithium-Ion Battery Systems with Special Emphasis on Cell Performance Distribution
1. Aufl. 2017, 184 S.
ISBN 978-3-8440-5090-5

ABISEA Band 89
Käbitz, Stefan
Untersuchung der Alterung von Lithium-Ionen-Batterien mittels Elektroanalytik und elektrochemischer Impedanzspektroskopie
1. Aufl. 2016, 258 S.
DOI: 10.18154/RWTH-2016-12094

ABISEA Band 90
Witzenhausen, Heiko
Elektrische Batteriespeichermodelle: Modellbildung, Parameteridentifikation und Modellreduktion
1. Aufl. 2017, 266 S.
DOI: 10.18154/RWTH-2017-03437

ABISEA Band 91
Münnix, Jens
Einfluss von Stromstärke und Zyklentiefe auf graphitische Anoden
1. Aufl. 2017, 171 S.
DOI: 10.18154/RWTH-2017-01915

ABISEA Band 92
Pilatowicz, Grzegorz
Failure Detection and Battery Management Systems of Lead-Acid Batteries for Micro-Hybrid Vehicles
1. Aufl. 2017, 212 S.
DOI: 10.18154/RWTH-2017-09156

ABISEA Band 93
Drillkens, Julia
Aging in Electrochemical Double Layer Capacitors: An Experimental and Modeling Approach
1. Aufl. 2017, 179 S.
DOI: 10.18154/RWTH-2018-223434

ABISEA Band 94
Magnor, Dirk
Globale Optimierung netzgekoppelter PV-Batteriesysteme unter besonderer Berücksichtigung der Batteriealterung
1. Aufl. 2017, 210 S.
DOI: 10.18154/RWTH-2017-06592

ABISEA Band 95
Iliksu, Merve
Elucidation and Comparison of the Effects of Lithium Salts on Discharge Chemistry of Nonaqueous Li-O_2 Batteries
1. Aufl. 2018, 160 S.
DOI: 10.18154/RWTH-2018-223782

ABISEA Band 96
Schmalstieg, Johannes
Physikalisch-elektrochemische Simulation von Lithium-Ionen-Batterien: Implementierung, Parametrierung und Anwendung
1. Aufl. 2017, 168 S.
DOI: 10.18154/RWTH-2017-04693

ABISEA Band 97
Soltau, Nils
High-Power Medium-Voltage DC-DC Converters: Design, Control and Demonstration
1. Aufl. 2017, 176 S.
DOI: 10.18154/RWTH-2017-04084

ABISEA Band 98
Stieneker, Marco
Analysis of Medium-Voltage Direct-Current Collector Grids in Offshore Wind Parks
1. Aufl. 2017, 144 S.
DOI: 10.18154/RWTH-2017-04667

ABISEA Band 99
Masomtob, Manop
A New Conceptual Design of Battery Cell with an Internal Cooling Channel
1. Aufl. 2017, 167 S.
DOI: 10.18154/RWTH-2018-223281

ABISEA Band 100
Marongiu, Andrea
Performance and Aging Diagnostic on Lithium Iron Phosphate Batteries for Electric Vehicles and Vehicle-to-Grid Strategies
1. Aufl. 2017, 222 S.
DOI: 10.18154/RWTH-2017-09944

ABISEA Band 101
Gitis, Alexander
Flaw detection in the coating process of lithium-ion battery electrodes with acoustic guided waves
1. Aufl. 2017, 109 S.
DOI: 10.18154/RWTH-2017-099519

ABISEA Band 102
Neeb, Christoph
Packaging Technologies for Power Electronics in Automotive Applications
1. Aufl. 2017, 132 S.
DOI: 10.18154/RWTH-2018-224569

ABISEA Band 103
Adler, Felix
A Digital Hardware Platform for Distributed Real-Time Simulation of Power Electronic Systems
1. Aufl. 2017, 156 S.
DOI: 10.18154/RWTH-2017-10761

ABISEA Band 104
Becker, Jan
Flexible Dimensionierung und Optimierung hybrider Lithium-Ionenbatterie-speichersysteme mit verschiedenen Auslegungs-zielen
1. Aufl., 2017, 157 S.
DOI: 10.18154/RWTH-2017-09278

ABISEA Band 105
Warnecke, Alexander J.
Degradation Mechanisms in NMC Based Lithium-Ion Batteries
1. Aufl. 2017, 158 S.
DOI: 10.18154/RWTH-2017-09646

ABISEA Band 106
Taraborrelli, Silvano
Bidirectional Dual Active Bridge Converter using a Tap Changer for Extended Voltage Ranges
1. Aufl. 2017, 94 S.
DOI: 10.18154/RWTH-2018-228242

ABISEA Band 107
Sarriegi, Garikoitz
SiC and GaN Semiconductors: The Future Enablers of Compact and Efficient Converters for Electromobility
1. Aufl. 2017, 106 S.
DOI: 10.18154/RWTH-2018-227548

ABISEA Band 108
Senol, Murat
Drivetrain Integrated Dc-Dc Converters utilizing Zero Sequence Currents
1. Aufl. 2017, 134 S.
DOI: 10.18154/RWTH-2018-226170

ABISEA Band 109
Kojima, Tetsuya
Efficiency Optimized Control of Switched Reluctance Machines
1. Aufl. 2017, 142 S.
DOI: 10.18154/RWTH-2018-226697

ABISEA Band 110
Lewerenz, Meinert
Dissection and Quantitative Description of Aging of Lithium-Ion Batteries Using Non-Destructive Methods Validated by Post-Mortem-Analyses
1. Aufl. 2018, 139 S.
DOI: 10.18154/RWTH-2018-228663

ABISEA Band 111
Büngeler, Johannes
Optimierung der Verfügbarkeit und der Lebensdauer von Traktionsbatterien für den Einsatz in Flurförderfahrzeugen
1. Aufl. 2018, 171 S.
DOI: 10.18154/RWTH-2018-226569

ABISEA Band 112
Wegmann, Raphael
Betriebsstrategien und Potentialbewertung hybrider Batteriespeichersysteme in Elektrofahrzeugen
1. Auflage 2018, 184 S.
DOI: 10.18154/RWTH-2018-228833

ABISEA Band 113
Nordmann, Hannes
Batteriemanagementsysteme unter besonderer Berücksichtigung von Fehlererkennung und Peripherieanalyse
1. Aufl. 2018, 222 S.
DOI: 10.18154/RWTH-2018-228763

ABISEA Band 114
Engelmann, Georges
Reducing Device Stress and Switching Losses Using Active Gate Drivers and Improved Switching Cell Design
1. Aufl. 2018, 195 S.
DOI: 10.18154/RWTH-2018-228973

ABISEA Band 115
Klein-Heßling, Annegret
Active DC-Power Filters for Switched Reluctance Drives during Single-Pulse Operation
1. Aufl. 2018, 166 S.
DOI: 10.18154/RWTH-2018-231030

ABISEA Band 116
Burkhart, Bernhard
Switched Reluctance Generator for Range Extender Applications - Design, Control and Evaluation
1. Aufl. 2018, 194 S.
DOI: 10.18154/RWTH-2019-00025

ABISEA Band 117
Biskoping, Matthias
Discrete Modeling and Control of a versatile Power Electronic Test Bench with Special Focus on Central Photovoltaic Inverter Testing
1. Aufl. 2018, 236 S.
DOI: 10.18154/RWTH-2019-03346

ABISEA Band 118
Schubert, Michael
High-Precision Torque Control of Inverter-Fed Induction Machines with Instantaneous Phase Voltage Sensing
1. Aufl. 2019, 221 S.
DOI: 10.18154/RWTH-2018-231364

ABISEA Band 119
Van der Broeck, Christoph
Methodology for Thermal Modeling, Monitoring and Control of Power Electronic Modules
1. Aufl. 2019, 290 S.
DOI: 10.18154/RWTH-2019-01370

ABISEA Band 120
Hust, Friedrich Emanuel
Physico-chemically motivated parameterization and modelling of real-time capable lithium-ion battery models – a case study on the Tesla Model S battery
1. Aufl. 2019, 203 S.
DOI: 10.18154/RWTH-2019-00249

ABISEA Band 121
Ralev, Iliya
Accurate Torque Control of Position Sensorless Switched Reluctance Drives
1. Aufl. 2019, 154 S.
DOI: 10.18154/RWTH-2019-03071

ABISEA Band 122
Ayeng'o, Sarah Paul
Optimization of number of PV cells connected in series for a direct-coupled PV system with lead-acid and lithium-ion batteries
1. Aufl. 2019, 114 S.
DOI: 10.18154/RWTH-2019-01843

ABISEA Band 123
Koschik, Stefan Andreas
Permanenterregte Synchronmaschinen mit verteilter Einzelzahnsteuerung - Regelkonzepte und Betriebsstrategien für hochintegrierte Antriebssysteme
1. Aufl. 2019, 158 S.
DOI: 10.18154/RWTH-2019-03446

ABISEA Band 124
Farmann, Alexander
A comparative study of reduced-order equivalent circuit models for state-of-available-power prediction of lithium-ion batteries in electric vehicles
1. Aufl. 2019, 214 S.
DOI: 10.18154/RWTH-2019-04700

ABISEA Band 125
Mareev, Ivan
Analyse und Bewertung von batteriegetriebenen, oberleitungsversorgten und brennstoffzellengetriebenen Lastkraftwagen für den Einsatz im Güterfernverkehr in Deutschland
1. Aufl. 2019, 158 S.
DOI: 10.18154/RWTH-2019-04698

ABISEA Band 126
Qi, Fang
Online Model-predictive Thermal Management of Inverter-fed Electrical Machines
1. Aufl. 2019, 154 S.
DOI: 10.18154/RWTH-2019-08304

ABISEA Band 127
Kairies, Kai-Philipp
Auswirkungen dezentraler Solarstromspeicher auf Netzbetreiber und Energieversorger
1. Aufl. 2019, 140 S.
DOI: 10.18154/RWTH-2019-06706

ABISEA Band 128
Fleischer, Michael
Traction control for Railway Vehicles
1. Aufl. 2019, 162 S.
DOI: 10.18154/RWTH-2019-10570

ABISEA Band 129
Teuber, Moritz
Lifetime Assessment and Degradation Mechanisms in Electric Double-Layer Capacitors
1. Aufl. 2019, 150 S.
DOI: 10.18154/RWTH-2019-10071

ABISEA Band 130
Bußar, Christian
Investigation of Optimal Transformation Pathways towards 2050 for the Successful Implementation of a Sustainable Reduction of Carbon Emissions from Power Generation
1. Aufl. 2019, 204 S.
DOI: 10.18154/RWTH-2019-09975

ABISEA Band 131
Wienhausen, Arne Hendrik
High Integration of Power Electronic Converters enabled by 3D Printing
1. Aufl. 2019, 146 S.
DOI: 10.18154/RWTH-2019-08746

ABISEA Band 132
Kwiecien, Monika
Electrochemical Impedance Spectroscopy on Lead-Acid Cells during Aging
1. Aufl. 2019, 138 S.
DOI: 10.18154/RWTH-2019-09480

ABISEA Band 133
Titiz, Furkan Kaan
A Three-phase Low-voltage Grid-connected Current Source Inverter
1. Aufl. 2019, 128 S.
DOI: 10.18154/RWTH-2020-00458

ABISEA Band 134
Wünsch, Martin
Separation der Kathoden-alterung in Lithium-Ionen-Batteriezellen mittels elektrochemischer Impedanzspektroskopie
1. Aufl. 2019, 177 S.
DOI: 10.18154/RWTH-2019-11017

ABISEA Band 135
Badeda, Julia
Modeling and Steering of Multi-Use Operation with Uninterruptible Power Supply Systems - utilizing the example of lead-acid batteries
1. Aufl. 2020, 282 S.
DOI: 10.18154/RWTH-2020-05456

ABISEA Band 136
Kleinsteinberg, Björn
Energy Efficiency Increase of a Vanadium Redox Flow Battery with a Power-Based Model
1. Aufl. 2020, 163 S.
DOI: 10.18154/RWTH-2020-06092

ABISEA Band 137
Cai, Zhuang
Optimization of dimension and operation strategy for a wind-battery energy system in German electricity market under consideration of battery ageing process
1. Aufl. 2020, 144 S.
DOI: 10.18154/RWTH-2020-06525

ABISEA Band 138
Sabet, Pouyan Shafiei
Analysis of Predominant Processes in Electrochemical Impedance Spectra and Investigation of Aging Processes of Lithium-Ion Batteries with Layered Oxide Cathodes and Graphitic Anodes
1. Aufl. 2020, 136 S.
DOI: 10.18154/RWTH-2020-07683

ABISEA Band 139
Angenendt, Georg
Operation, Optimization and Additional Market Participation of Households with PV Battery Storage System and Power-to-Heat Application
1. Aufl. 2020, 221 S.
DOI: 10.18154/RWTH-2020-05200

ABISEA Band 140
Oberdieck, Karl Friedrich
Measurement and Mitigation of Electromagnetic Emissions of Propulsion Inverters for Electric Vehicles
1. Aufl. 2020, 181 S.
DOI: 10.18154/RWTH-2020-09215

ABISEA Band 141
Bubert, Andreas Martin
Optimierung des elektrischen Antriebsstrangs von Elektrofahrzeugen mit Betrachtung parasitärer Ströme innerhalb der elektrischen Maschine
1. Aufl. 2020, 215 S.
DOI: 10.18154/RWTH-2020-09556

ABISEA Band 142
Fleischer, Christian Georg
Model-Driven Software Development and Verification Solutions for Safety Critical Battery Management Systems
1. Aufl. 2021, 356 S.
DOI: 10.18154/RWTH-2021-00436

ABISEA Band 143
Arzberger, Arno
Thermografische Methoden zur zerstörungsfreien Messung der anisotropen Wärmeleitfähigkeit von Lithium-Ionen Zellen
1. Aufl. 2020, 131 S.
DOI: 10.18154/RWTH-2021-00479

ABISEA Band 144
Lange, Tobias
Oberwellenbasierte Modellierung, Regelung und Auslegung von Permanentmagnet- und Reluktanz-Synchronmaschinen
1. Aufl. 2020, S.
DOI: 10.18154/RWTH-2021-02537

ABISEA Band 145
Weiss, Claude
Fault Tolerant Switched Reluctance Machines with Distributed Inverters – Modeling and Control
1. Aufl. 2020, S.
DOI: 10.18154/RWTH-2021-02327

ABISEA Band 146
Huck, Moritz
Modelling the Transient Behaviour of Lead-Acid Batteries: Electrochemical Impedance of Adsorbed Species
1. Aufl. 2020, 151 S.
DOI: 10.18154/RWTH-2020-08362

ABISEA Band 147
Willenberg, Lisa
Volumenausdehnung und ihre Auswirkungen auf die Alterung einer zylindrischen Lithium-Ionen-Batterie
1. Aufl. 2020, S.
DOI: 10.18154/RWTH-2021-01906

ABISEA Band 148
Rogge, Matthias
Electrification of Public Transport Bus Fleets with Battery Electric Busses
1. Aufl. 2020, 161 S.
DOI: 10.18154/RWTH-2021-02146

ABISEA Band 149
Münderlein, Jeanette
Numerische Methodik zur Auslegung eines Hybriden Speichersystems mit Multinutzen“
1. Aufl. 2020, 221 S.
DOI: 10.18154/RWTH-2021-00867

ABISEA Band 150
Merten, Michael
Participation of Battery Storage Systems in the Secondary Control Reserve Market
1. Aufl. 2020, 187 S.
DOI: 10.18154/RWTH-2021-01029

ABISEA Band 151
Ge, Lefei
Performance Enhancement of Switched Reluctance Machines for High-speed Back-up Generators
1. Aufl. 2020, 152 S.
DOI: 10.18154/RWTH-2020-11546

ABISEA Band 152
Neubert, Markus
Modeling, Synthesis and Operation of Multiport-Active Bridge Converters
1. Aufl. 2020, 227 S.
DOI: 10.18154/RWTH-2020-10814

ABISEA Band 153
Schülting, Philipp
Optimierte Auslegung von hochintegrierten und bidirektionalen Onboard GaN-Ladegeräten
1. Aufl. 2020, 158 S.
DOI: 10.18154/RWTH-2020-09771

ABISEA Band 154
Sewergin, Alexander
Design Challenges and Solutions for the Practical Application of SiC Power Moduls – Exemplified by an Automotive DC-DC Converter. 1. Aufl. 2021, 154 S.
DOI: 10.18154/RWTH-2021-04498

ABISEA Band 155
Stippich, Alexander
Exploiting the Full Potential of Silicon Carbide Devices via Optimized Highly Integrated Power Modules
1. Aufl. 2021, 188 S.
DOI: 10.18154/RWTH-2021-08122

ABISEA Band 156
Gottschlich, Jan
Hilfsspannungsversorgungskonzepte für Mittelspannungs-DC/DC-Wandler
1. Aufl. 2021, S.
DOI: 10.18154/RWTH-2021-

ABISEA Band 157
Hollstegge, Philipp
Injektion raumzeigerzerlegter Stromharmonischer zur Minderung tonaler Geräuschanteile in asymmetrisch sechsphasigen Permanentmagnetsynchronmaschinen
1. Aufl. 2021, S.
DOI: 10.18154/RWTH-2021-11040

ABISEA Band 158
Grau, Vivien
Development of a Test Bench to Investigate the Impact of Steep Voltage Slopes on the Lifetime of Insulation Systems for Coil Windings
1. Aufl. 2021, S.
DOI: 10.18154/RWTH-2021-09577

ABISEA Band 159
Ringbeck, Florian
Optimized Charging of Lithium-Ion Batteries with Physico-Chemical Models
1. Aufl. 2021, S.
DOI: 10.18154/RWTH-2021-

ABISEA Band 160
Bank, Thomas
Performance and Aging Analysis of High-Power Lithium Titanate Oxide Cells for Low-Voltage Vehicle Applications
1. Aufl. 2021, S.
DOI: 10.18154/RWTH-2021-10369

ABISEA Band 161
Aupperle, Felix
Realizing High-Performance Silicon-Based Lithium-Ion Batteries
1. Aufl. 2022, S.
DOI: 10.18154/RWTH-2021-

ABISEA Band 162
Schröer, Philipp A.
Entwicklung einer adaptiven Leistungsprognosefunktion für Starterbatterien mit Lithium-Titanat-Oxid-Anode als Grundlage zur sicheren Energieversorgung im Fahrzeug
1. Aufl. 2021, S.
DOI: 10.18154/RWTH-2021-

One of the essential components of an electric vehicle is its energy storage system. Unfortunately, it has also proven to be the most expensive component, limiting the vehicle‘s performance, for example, range or power, for a given cost target. If higher spreads and more inferior cell quality can be coped within the system, costs can be lowered by decreasing the number of cells rejected in production. In addition, it is essential, in particular for large storage systems such as automotive or stationary storage applications, to ensure the extended usability of the systems. Especially in stationary applications, design lifetimes have to be in the range of 10 to 15 years. Therefore, the manufacturers need to ensure long-lasting battery modules as the smallest exchangeable units. Previous analysis on the impact of variations in commercial lithium-ion battery systems on ageing showed the vital role of spreads in cell parameters of the batteries.

The research aims to optimise system topologies for individual applications to find suitable cells, avoid oversizing battery systems and give forecasts of a lifetime and quantifiably failure rates for battery packs while decreasing cost. A simulation toolchain was developed to incorporate variability and ageing rate spreads in the system design process. In the scope of the simulation tool, battery topologies can be simulated with varying usage profiles, cell parameter spreads and varying ageing rates.

ISSN 1437-675X